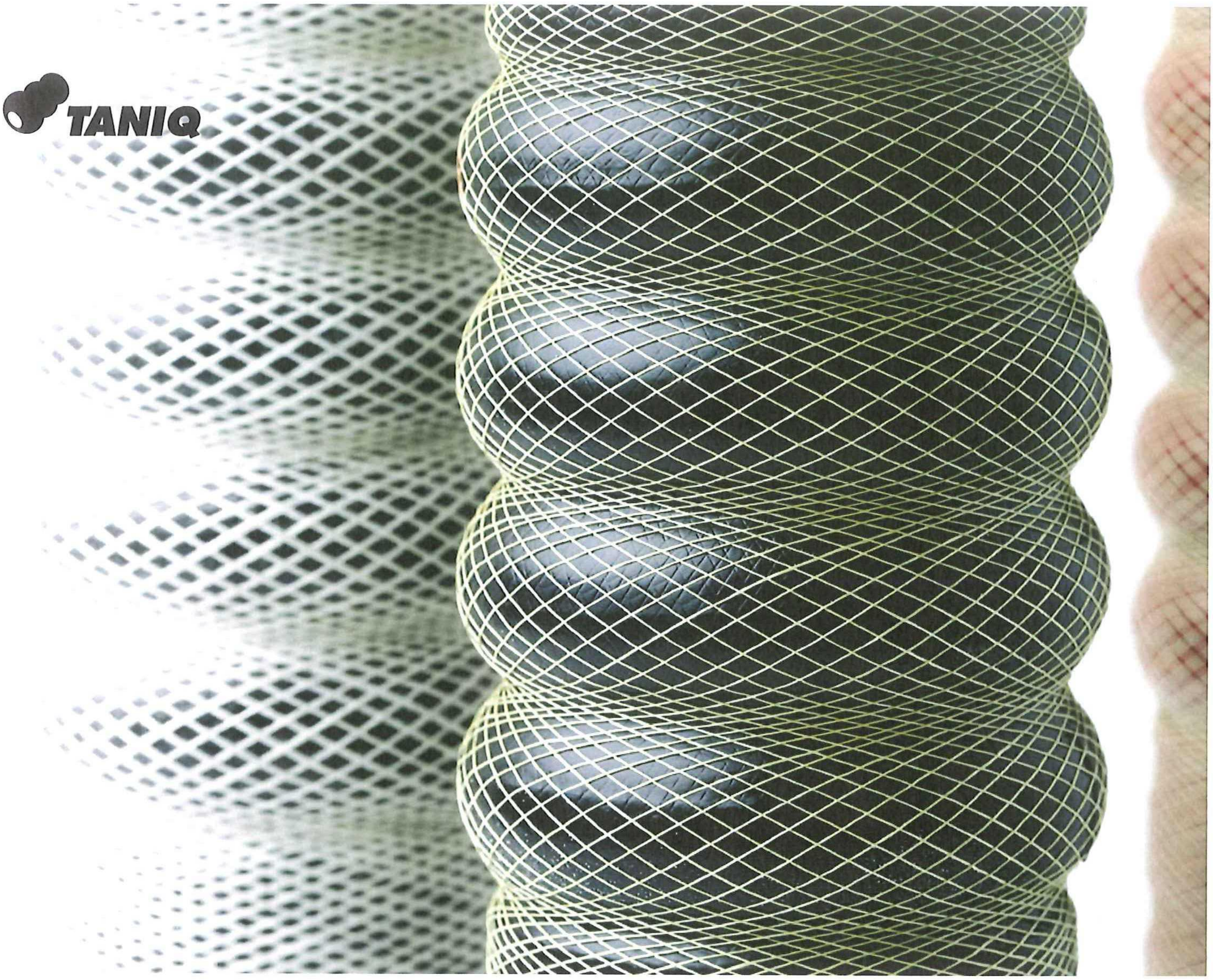

Structural Analysis of Multi-Layered Filament Wound Cord-Reinforced Rubber Products

With an application to Expansion Joints

Bram Davids
1515438

2/7/2014

Delft University of Technology
Challenge the future

Structural Analysis of Multi-Layered Filament Wound Cord-Reinforced Rubber Products

With an application to Expansion Joints

MSc. Thesis

B. Davids

July 2014

Structural Integrity and Composites
Faculty of Aerospace Engineering

Delft University of Technology

Graduation Committee:

Prof. dr. ir. R. Marissen
Dr. ir. S. Koussios
Dr. Ir. M. Ruess
Ir. R. Barendse

ABSTRACT

Taniq develops technology for manufacturers of cord-reinforced rubber products to improve their product performance and production process through product redesign and supply of software and production equipment. Taniq's technology is used for products ranging from straight large-bore hoses (Ø600 [mm]) to small bellowed expansion joints (Ø < 100 [mm]).

The current structural analysis used at Taniq is only able to predict fibre stresses of single-layered products in basic load cases. As many products require local reinforcements and/or multiple fibre layers this basic structural analysis is not proficient. Therefore these products are currently designed by trial-and-error.

It is of importance to gain insights in the complete stress state throughout the product in any load case to facilitate a more efficient design process. This stress state can be used for static and dynamic strength predictions, and for the development of design guidelines for future products. Therefore the research objective is:

To develop and validate a model for advanced structural analysis of multi-layered filament wound cord-reinforced rubber products.

For the structural analysis of the unique combination of multi-layered filament wound cord-reinforced rubber, numerical Finite Element Analysis methods have to be used. The finite deformation of the flexible products requires aligned fibre meshes to prevent intra-ply shear locking. This limits the available mesh constructions to aligned triangle or truss elements for the fibres and aligned tetrahedral or unaligned hexahedral elements for the rubber.

Various combinations of elements for the fibres and rubber have been evaluated and compared. Satisfactory agreement with test results of a pneumatic muscle, single-layered and multi-layered expansion joints has been shown. The models are not accurate enough to give an exact prediction of the strength of the product, but can be used for a comparison between different designs. It is decided to use a robust model with linear triangle elements embedded in unaligned linear hexahedral elements for further simulations. This model showed convergence for both the fibre forces, reaction forces and rubber strains.

A comparison of various calibrated rubber material models has shown that the basic material properties given by the rubber supplier are not able to accurately model the response of the rubber in biaxial and planar shear deformation modes. However, the basic material properties provide a slightly conservative approximation when modelling a complete expansion joint. It can therefore be argued whether the improvements achieved by using a fully calibrated model are worth the additional testing efforts.

The four characteristic failure modes of expansion joints are rubber cracking, fibre failure, fibre compression and fibre fretting. The most important dynamic failure mode of Aramid expansion joints is caused by fibre compression during lateral deformation. Nylon expansion joints are less sensitive to this failure mechanism.

Design of experiments has been used for a parametric study to investigate the influence of all design parameters on the performance of the product. The effect of the local reinforcement length on the performance of the product has been investigated separately. The results have been used to determine an optimal expansion joint design that satisfies all manufacturing constraints. Prototypes of this optimal expansion joint have been built to validate the optimization. During lateral dynamic testing the optimized design showed a major improvement. This proves that the numerical structural analysis method can be a valuable tool during the development of cord-reinforced rubber products.

Some design guidelines for expansion joints have been determined based on the results of the parametric study and the tests. These are listed below;

- Use Nylon Fibres
- Use a Corpo bellow
- Use the bridging procedure
- Apply local reinforcements

The optimal length of the reinforcement layer is the length where the angle of the angle-ply local reinforcement matches the fibre angle of the main fibre layer. This restricts the stiffness discontinuity that causes stress concentrations.

Recommended improvements of the numerical model are listed below;

- Implement the non-linear Riks solution method to resolve structural instabilities.
- Aligned truss elements can be used to increase the computational efficiency.
- Viscoelastic effects can be incorporated to increase the solution accuracy.
- Local-global models can be used to investigate stress concentrations and delamination of local reinforcements.

Next to the numerical improvements, it is recommended to investigate the effect of advanced calibrated material models on the simulation of multi-layered expansion joints. Furthermore the design of experiments can be improved by eliminating the reinforcement length design parameters as these are not able to describe the rubber cracking failure mode. This can be accounted for by writing an algorithm that determines the optimal reinforcement length for a given set of design parameters based on minimizing the stiffness discontinuity.

PREFACE

This report is written as part of my graduation to obtain a Master of Science degree in Aerospace Engineering at the Structural Integrity and Composites (SI&C) chair of the Delft University of Technology. The thesis has been performed in collaboration with Taniq, a company developing technology for manufacturers of cord-reinforced rubber products.

The idea of this thesis came to mind during an internship at Taniq. While being highly experienced in the design and manufacturing of cord-reinforced rubber products, their experience with the structural analysis of the products that they develop was limited. This gave the opportunity to contribute to the development of Taniq while further developing my skills in (numerical) structural analysis. Taniq has been very helpful as their hands-on mentality enabled an extensive experimental testing program which has been used for the verification and validation of the structural analysis models.

I would especially like to thank my company supervisor Rob Barendse for his advice, support and insightful comments during the research. His MSc thesis has been the foundation for the development of the numerical structural analysis method. I would also like to thank Soren Blomaard and Coen ten Herkel, the founders of Taniq. Without their early commitment to this project it would not have come into being.

Furthermore, I would like to thank my supervisor from Delft University of Technology, Sotiris Koussios, for his counsel. He has been the founder of the technology on which Taniq's products are based. I would also like to thank Martin Ruess for his support and counsel during the development of the numerical analysis models. Furthermore I would like to thank Roel Marissen for being in my graduation committee. His lectures and enthusiasm have been an inspiration during my master study.

I would also like to thank René ten Thije and his team at AniForm for their quick support during the use of their software. Next, I would like to thank Philippe Willems for the collaboration, support and fun times during our master studies.

At last I would like to thank my parents. They have provided me with a carefree environment during my studies, allowing me to perform without any concerns. Without their support my studies would have been a lot harder.

Bram Davids,
Delft, July 2014

TABLE OF CONTENTS

LIST OF TABLES

LIST OF FIGURES

NOMENCLATURE

ABBREVIATIONS

AB	Arruda-Boyce material model
ASTM	American Society for Testing and Materials
CR	Chloroprene Rubber
DOE	Design of Experiments
FEA	Finite Element Analysis
M	Marlow material model
MR	Mooney-Rivlin material model
NHg	Neo-Hookean material model, given parameters
NHc	Neo-Hookean material model, calibrated parameters
NR	Natural Rubber
Oa	Ogden material model, approximated parameters
Ot	Ogden material model, calibrated parameters
Ref	Reinforcement
SBR	Styrene-Butadiene Rubber
vdW	van der Waals material model
Y	Yeoh material model

SYMBOLS

$\emptyset$	Diameter

GREEK SCALARS

α	Fibre angle	9, 71, 97
	Hyperelastic material constant	38, 86
β	Invariant mixture parameter	
θ	Independent winding variable	
λ	Stretch	
μ	Initial shear modulus	
ν	Poisson's ratio	
ρ	Corpo load factor	
σ	Stress	9
	Standard deviation	20

LATIN SCALARS

A	Axial load	8
	Area	81
a	Global interaction parameter	
C	Hyperelastic material constant	
E	Young's modulus	
$\boldsymbol{F}$	Deformation gradient	

FF	Fibre force	
I	Strain invariant	
k	Dimensionless load	
l	Length	
n	Number	
P	Internal pressure	
p	Hydrostatic pressure	
q	Corpo Shape Factor	
r	Radial Coordinate	
R	Radius of curvature	9
	Coefficient of determination	52
s	Path coordinate	10
	Spacing	84
t	Thickness	
T	Nominal stress	
U	Work	36
	Strain energy potential	85
Y	Dimensionless radial coordinate	
z	Axial coordinate	
Z	Dimensionless axial coordinate	

INDICES

0	Related to theoretical minimum	
1	Related to the 1st principal direction	
2	Related to the 2nd principal direction	
3	Related to the 3th principal direction	
θ	Related to the circumferential direction	
φ	Related to the longitudinal direction	
a	Related to axial load	
B	Related to Biaxial deformation	
dev	Related to the deviatoric behaviour	
eq	Related to the equator	
$fibre$	Related to the fibre	
m	Related to the meridional direction	9
	Related to polymer network locking	85
min	Related to the actual minimum	
n	Related to the surface normal	
p	Related to the polar direction	
S	Related to planar shear deformation	
U	Related to uniaxial deformation	

LIST OF APPENDIX TABLES

LIST OF APPENDIX FIGURES

1 INTRODUCTION

Taniq develops technology for manufacturers of cord-reinforced rubber products to improve their product performance and production process through product redesign and supply of software and production equipment. Taniq's technology is used for products ranging from straight large-bore hoses (Ø600 [mm]) to small bellowed expansion joints (Ø < 100 [mm]).

The current structural analysis used at Taniq is based on monotropic stress analysis and is only able to predict fibre stresses of single-layered products in basic load cases. As many products require local reinforcements and/or multiple fibre layers, this basic structural analysis is not proficient. Therefore these products are currently designed by trial-and-error.

To facilitate a more efficient design process it is of importance to gain insights in the complete stress state throughout the product in any load case. This stress state can be used for static and dynamic strength predictions, and for the development of design guidelines for future products. Therefore the research objective is:

To develop and validate a model for advanced structural analysis of multi-layered filament wound cord-reinforced rubber products

To develop these models a literature study has been performed to investigate the products' characteristic behaviour and the available analytical and/or numerical methods to model this behaviour. This literature study has shown that the unique combination of materials, production method and geometry limits the applicability of a general analytical model. Therefore a link between Taniq's design software and various numerical analysis tools will be made.

The developed numerical structural analysis models will be evaluated and compared by applying them to expansion joints. Design of Experiments will be used to investigate the main and interaction effects of the design parameters of an expansion joint. These effects are used to determine an optimal design, which will be validated by static and dynamic testing.

A brief overview of the state of the art structural analysis methods and characteristic behaviour of cord-reinforced rubbers is given in Chapter 2. To improve the understanding of expansion joints, Chapter 3 provides some technical background. Various numerical Finite Element Analysis (FEA) methods will be evaluated and compared in Chapter 4. The simulations are dependent on the quality of their input. Therefore the effect of the accuracy of the hyperelastic rubber material models on the numerical analysis is investigated in Chapter 5. To translate the results predicted by the analysis to actual product performance, the failure modes of expansion joints are studied in Chapter 6. These failure modes enable a parametric study and optimization of an expansion joint. These are performed in Chapter 7 to validate the applicability of the developed analysis model. At last, Chapter 8 gives the conclusion and some recommendations for future research.

2 STATE OF THE ART

The optimal fibre geometry of filament wound structures generally does not require local reinforcement. However, the majority of cord-reinforced rubber products need local reinforcements as their flanges cannot be wound in an optimal way. This results in the unique combination of tapered filament wound cord-reinforced rubber products. Although numerous analytical and numerical methods have been developed for each of these separate topics, a combination of these topics is uncommon in literature. Therefore, in this Chapter an overview is given of the current state of the art on structural analysis of filament wound structures as well as important characteristic effects of cord-reinforced rubbers.

The structural analysis of filament wound structures will be discussed in Section 2.1. Next, the characteristic effects that have to be accounted for during structural analysis of cord-reinforced rubbers are presented in Section 2.2.

2.1 FILAMENT WINDING

Structural analysis of filament wound structures is often based on fundamental elasticity or shell theories. Shell theories are a good approximation for shells up to a moderate thickness. The more complex elasticity theories on the other hand offer a more accurate prediction of stresses in all three dimensions and can thus be applied to structures with any thickness. [1]

Analytical structural analysis methods of filament wound structures can be divided into monotropic, orthotropic and thick-walled analysis. The monotropic method neglects the matrix properties and is limited to the analysis of fibre stresses. The orthotropic analysis does take the matrix into account but is limited to thin-walled structures. The most advanced analytical analysis methods are thick-walled theories based on elasticity theories and fully describe the through-thickness normal stress distribution. [2-4] These through-thickness stresses have a significant effect on the stress-distribution in cord-reinforced rubber products. Current analytical thick-walled analysis is limited to cylindrical shells with a constant winding angle in each ply. Furthermore it is generally only applicable to axisymmetric load cases, making them unsuitable for the structural analysis of most cord-reinforced rubber products.

Numerical FEA is applicable to any load case and or geometry and is frequently applied for the structural analysis of complex filament wound structures. FEA has shown significant effects of winding patterns and through-thickness fibre angle distributions. [5, 6] Preceding research has shown promising results for the applicability of FEA to single-layered filament wound cord-reinforced rubber products. [7, 8] Furthermore, three dimensional FEA models are able to accurately predict the stress distribution around local-reinforcements (tapered laminates). [9]

2.2 CORD-REINFORCED RUBBERS

Cord-reinforced rubbers have been investigated since the early 60s. They are a special subset of composites that combine the flexibility of the rubber matrix with the strength of the cords to create strong flexible structures. Their most common application is in tires that are reinforced by uni-directional steel cords. Therefore most of the research devoted to this topic is performed in the tire industry.

Due to the material characteristics of the rubber matrix material, rubber composites behave different than typical polymer composites. When analysing cord-reinforced rubber, some important effects have to be taken into account. These are non-linear incompressible hyperelastic stress-strain behaviour, fibre shearing and interlaminar normal stresses.

Rubber is a hyperelastic incompressible material. The stress-strain behaviour is non-linear and cannot be described by traditional linear-elastic analysis. Rubber is therefore modelled by non-linear hyperelastic continuum mechanics material models.

An important effect of cord-reinforced rubbers is the effect of fibre shearing. This effect is caused by the difference of matrix and fibre stiffness. In regular polymer composites this ratio ranges from 50 to 200, whereas cord-reinforced rubbers have a ratio between 500-5000. Cord-reinforced rubber has a higher level of anisotropy that causes its strain dependent properties. When a load is applied, the stiff fibres tend to align with the direction of maximum stress as illustrated in Figure 2.1. To account for the shifting of the fibres, the stiffness properties of the deformed configuration have to be used instead of the properties of the undeformed configuration. This is also known as finite deformation analysis.

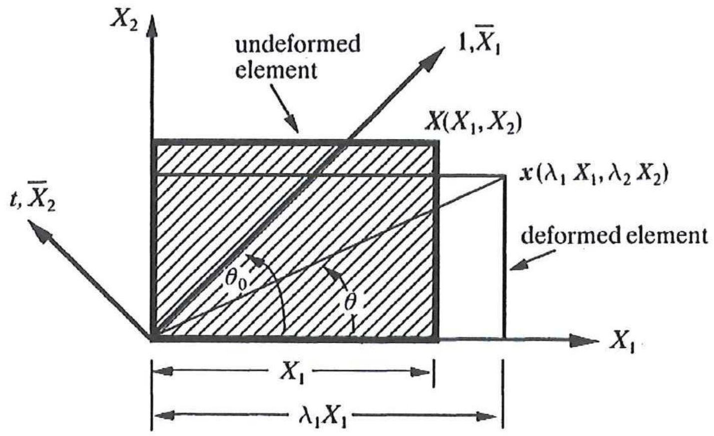

FIGURE 2.1: HOMOGENEOUS ANISOTROPIC DEFORMATION [10]

A major challenge in multi-layered cord-reinforced rubber hoses is the load transfer between different layers. Due to the hyperelasticity of the interply rubber matrix, the inner fibres are able to stretch significantly before the outer fibres experience any loading. This causes an inhomogeneous load distribution through the thickness. It has been shown that in the case of a two ±54°-layered high pressure hose with 20 [mm] diameter, the stress in the inner layer is 24% higher than the outer layer. [11] This indicates that interlaminar normal stresses have to be accounted for when modelling multi-layered cord-reinforced rubbers.

3 TECHNICAL BACKGROUND

In this work an attempt is made to develop a structural analysis method for filament wound cord-reinforced rubber products in general. To validate this structural analysis method, it is compared with test data of expansion joints. In the field of composites, the interaction between material, manufacturing and design has to be kept in mind at all times. To understand the design drivers and the limitations in the expansion joint design space, it is important to have some background information on both the product and manufacturing methods.

In this Chapter the function of an expansion joint and different types of expansion joints are discussed in Section 3.1. Next, Section 3.2 describes the unique manufacturing process developed by Taniq. At last, the fundamental theory of the design of optimized bellows is presented in Section 3.3.

3.1 EXPANSION JOINTS

Currently Taniq's main focus is the expansion joint market. There are multiple expansion joint development projects in progress for a variety of manufacturers. A typical expansion joint is shown in Figure 3.1. They are widely applied in fluid or gas piping systems to absorb axial, lateral, angular or twisting movement between different pipes within the system. Their geometry varies from an inner diameter of 100 [mm] up to 4000 [mm]. However, the production process of Taniq is currently limited to a maximum diameter of 1200 [mm].

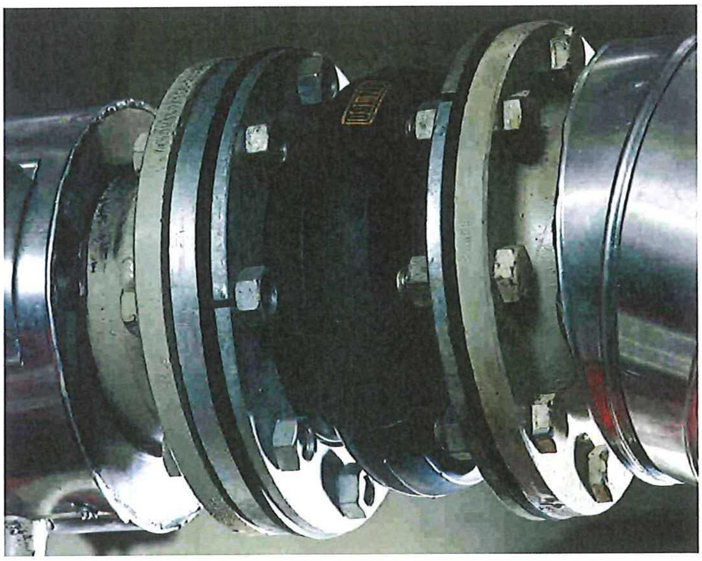

FIGURE 3.1: EXPANSION JOINT [12]

The length and shape of the bellow(s) varies between manufacturers. Taniq determines an optimal bellow by using the Corpo technology, as will be discussed in Section 3.3. The three major types of expansion joint designs for Taniq are standard, high-flow or multiple bellow designs as shown in Figure 3.2.

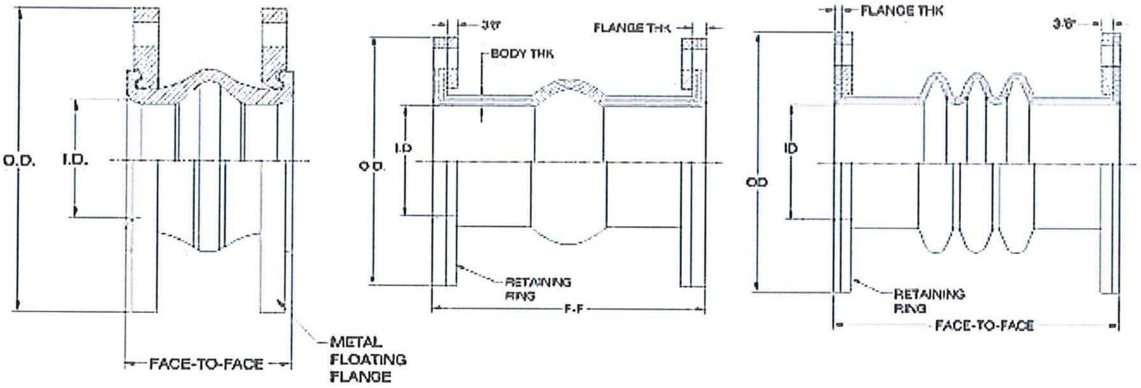

FIGURE 3.2: EXPANSION JOINT BELLOW TYPES
LEFT: STANDARD, MIDDLE: HIGH FLOW, RIGHT: MULTIPLE BELLOW

Next to the bellow shape an important design feature is the flange type. The flange geometry is dictated by standards. However there are three different types of flange configurations, being the full rubber flange, the standard floating flange or the bead ring floating flange. These are illustrated in Figure 3.3. In the full rubber flange the bolt holes are cut directly through the rubber whereas in the other flange types a metal flange compresses the expansion joint to create a seal.

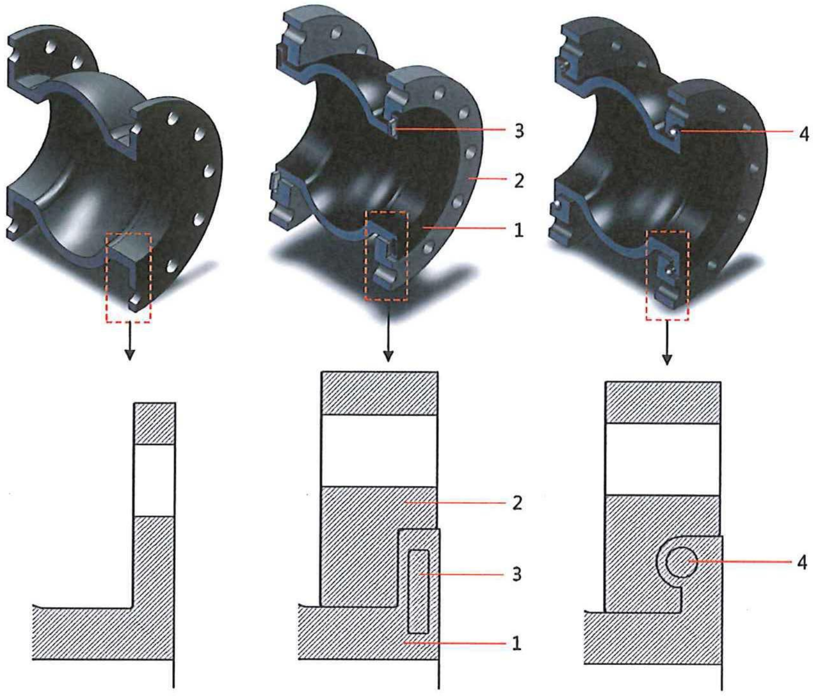

FIGURE 3.3: FLANGE TYPES [13]
LEFT: FULL RUBBER FLANGE, MIDDLE: STANDARD FLOATING FLANGE, RIGHT: BEAD RING FLOATING FLANGE

The internal structure of the expansion joints typically exist of an inner rubber liner for chemical protection and load distribution over the fibres and one or multiple filament wound fibre layer(s) to carry the pressure loads. The outer rubber layer protects the expansion joint against environmental influences. Furthermore there can be local axial, circumferential and/or cross-ply fibre reinforcement layers. By varying these parameters, a wide variety of expansion joint designs is possible to tailor their performance for specific requirements.

3.2 MANUFACTURING

One of the unique technologies that Taniq offers is their automated production process. They have developed robot tools that are able to place fibres by filament winding, wind rubber and apply wrapping tape. These three production steps are illustrated in Figure 3.4.

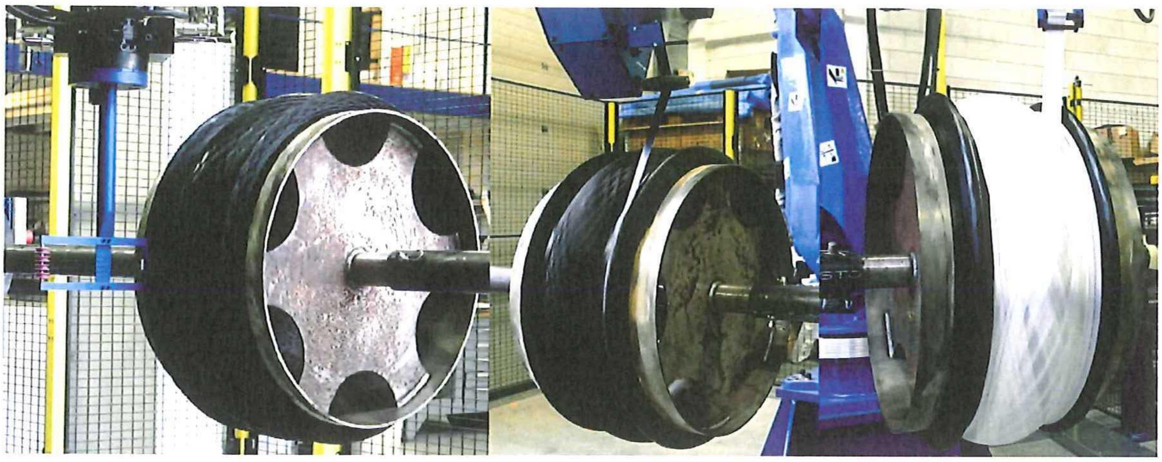

FIGURE 3.4: EXPANSION JOINT PRODUCTION STEPS
LEFT: FIBRE WINDING, MIDDLE: RUBBER WINDING, RIGHT: TAPE WRAPPING

This production process has a number of benefits. First of all it is much quicker than the manual production that is currently applied in the expansion joint industry. Another major benefit is the high reproducibility of products and the accurate fibre placement. The design software is able to create output of the precise geometry and fibre angles throughout the product. This data is essential for an accurate structural analysis.

A recent development in the production of expansion joints at Taniq is the so called "bridging" method. During traditional filament winding, the winding angle near the flanges approaches 90° to prevent bridging of the fibres. Such high fibre angles are not able to provide sufficient axial stiffness in this region to prevent rubber tearing. To increase axial stiffness in this region a lower fibre angle is required. This can be achieved by the bridging procedure. In a bridging prototype the wound flange region is elongated and fibre bridging is allowed. During the moulding, this region is compressed towards its intended length causing the bridged fibres to neatly fold into the flange edges. The winding and moulding profiles and fibre paths of a bridging prototype are illustrated in Figure 3.5.

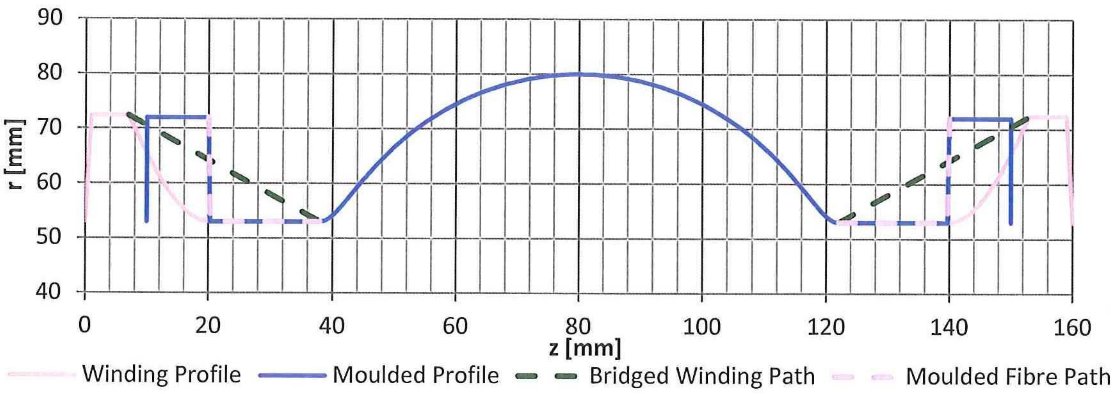

FIGURE 3.5: WINDING AND MOULDED PROFILES AND WINDING PATHS

3.3 CORPO TECHNOLOGY

The Corpo technology is a geometric description of halve a bellow with two vertical ends. Due to the vertical ends it is possible to combine multiple bellows to create multi-bellowed hoses. An example of a Corpo profile, described by axial (z) and radial (r) coordinates is shown in Figure 3.6. [2]

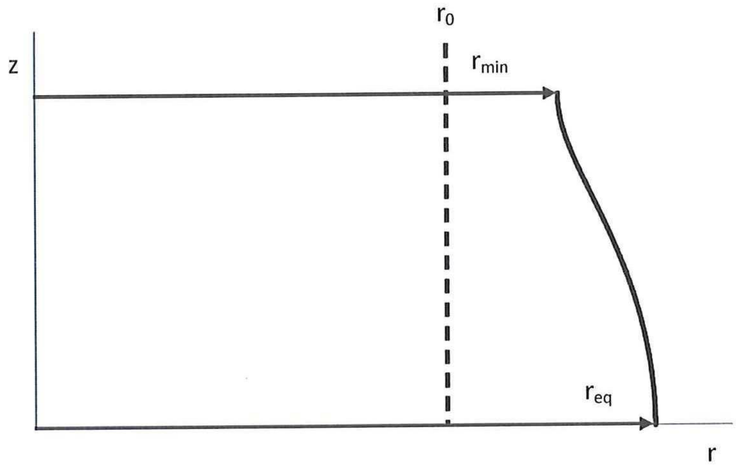

FIGURE 3.6: CORPO PROFILE [14]

A Corpo contour can be described by the dimensionless coordinates Y and Z given in Equation 3.1.

$$Y = \frac{r}{r_0}$$
$$Z = \frac{z}{r_0} \qquad 3.1$$

A Corpo profile is typically loaded by an internal pressure (P) and an axial load (A). The axial load can be made dimensionless using Equation 3.2.

$$k_a = \frac{A}{\pi P {r_0}^2} \qquad 3.2$$

Combining these dimensionless parameters a Corpo profile can be fully described by just three parameters (q, ρ and r_0). The shape factor q relates the dimensionless radius of the equator (Y_{eq}) and the poles (Y_{min}). The ρ factor is determined by the dimensionless axial force. Both are shown in Equation 3.3.

$$q = \left(\frac{Y_{eq}}{Y_{min}}\right)^2$$
$$\rho = \frac{k_a}{{Y_{eq}}^2} \qquad 3.3$$

When the fibre orientation on a Corpo profile is precisely controlled by filament winding, it can lead to optimally reinforced bellowed hoses. This is achieved by isotensoid and geodesic winding paths.

3.3.1 ISOTENSOID

Isotensoid loading is a constant load throughout the length of a fibre. This is an optimal loading condition as it allows the full strength of the fibre to be utilized. Isotensoid loading is achieved by matching the fibre angle with the direction of maximum load, as given by Equation 3.4. [2]

$$\frac{\sigma_\varphi}{\sigma_\theta} = \tan^2 \alpha \tag{3.4}$$

Here α is the fibre angle with respect to the longitudinal direction of the product, σ_φ is the stress component in the longitudinal direction and σ_θ the stress component in the circumferential direction.

3.3.2 GEODESIC

To obtain an optimally loaded structure, the fibre path has to fulfil the isotensoid condition. However, the filament winding process limits the feasible winding paths. To control the fibre placement, filament winding requires some tension in the fibre. When a fibre under tension is placed on a frictionless surface it will naturally follow the shortest path between two points, also known as a geodesic path. By limiting the fibre placement to these inherently stable paths, the feasibility of production is guaranteed. On a rotational symmetric shape, geodesic fibre paths are given by the Clairaut relation shown in Equation 3.5. [2]

$$r \sin \alpha = constant \tag{3.5}$$

When the winding angle at a single position is chosen, the constant on the right hand side is set. The entire geodesic fibre path is thus determined by the winding angle at a single position. In the case of a Corpo profile a winding angle of 90° is specified at the theoretical smallest radius of the product r_0. This allows the Clairaut relation to be rewritten to Equation 3.6.

$$\alpha = arcsin\frac{1}{Y} = arcsin\frac{r_0}{r} \tag{3.6}$$

3.3.3 OPTIMAL WINDING

Now that the criteria for guaranteed windability (geodesic) and optimal loading (isotensoid) are known, they can be combined to create optimal windable structures. Combining Equation 3.4 and 3.6, gives the condition described by Equation 3.7.

$$\frac{\sigma_\varphi}{\sigma_\theta} = \tan^2\left(arcsin\frac{1}{Y}\right) = \frac{1}{Y^2 - 1} \tag{3.7}$$

The shell stresses in a double curved surface under pressure are related by their radii of curvature in the meridional and polar direction, as shown in Equation 3.8. [15]

$$\frac{\sigma_\theta}{R_m} + \frac{\sigma_\varphi}{R_p} = \frac{P}{t} \tag{3.8}$$

Matching these stresses with the force equilibrium in axial direction as given by Equation 3.9, determines the complete stress state of a body of revolution.

$$A + P\pi r^2 = \sigma_\theta 2\pi r t \frac{dz}{ds} \qquad 3.9$$

Combining Equation 3.1 to 3.9 yields a description of the dimensionless profile. The dimensionless coordinates Y and Z are described by the Corpo parameters q, ρ and an independent integration variable θ ($0 \leq \theta \leq \frac{\pi}{2}$). These dimensionless coordinates are given in Equation 3.10. [2]

$$Y = \sqrt{{Y_{eq}}^2 \cos^2\theta + {Y_{min}}^2 \sin^2\theta}$$

$$Z = \frac{Y_{min}}{\sqrt{1+2q(1+\rho)}} \left((1+2q(1+\rho)) ellE\left(\theta, \frac{q-1}{1+2q(1+\rho)}\right) - (1+q+q\rho) ellF\left(\theta, \frac{q-1}{1+2q(1+\rho)}\right) \right) \qquad 3.10$$

In this Equation $ellE$ and $ellF$ denote incomplete elliptic integrals of the first and second kind.[2] Any profile described by this Equation fulfils the conditions for both isotensoid and geodesic winding paths. In the software of Taniq, bellow profiles are constructed according to these Equations, ensuring optimal windable bellows.

4 FINITE ELEMENT ANALYSIS

The objective of this thesis is to develop tools for the analysis of a wide variety of cord-reinforced rubber products. As there are no analytical models that are applicable to all relevant load cases and products, the decision has been made to develop and evaluate more generally applicable numerical approaches. These models will be tested and verified with an application to expansion joints, as extensive experimental testing and development programs of these products are being performed by Taniq.

Only a few numerical methods are able to accurately model intra-ply shear as indicated in Section 2.2. One way is by modelling each fibre separately using truss elements. Another way is to use membrane/shell elements in combination with material models that capture the material reorientation. In both cases a proper coupling between the fibre and rubber elements has to be ensured.

A single-layered numerical shell model has shown promising results for the analysis of a filament wound turbo-hose. [7] In this Chapter this model is extended to incorporate through-thickness effects of the rubber and evaluate locally reinforced multi-layered products.

Both the specialized software package AniForm and the widely applied Abaqus software are evaluated. AniForm is specialized in the analysis of forming processes of composite materials and utilizes an updated Lagrangian solution method that is able to analyse fibre structures undergoing large deformations. This updated Lagrangian solution method utilizes a continuously non-linear finite strain definition whereas the conventional solution method discretizes the non-linear strain path by a number of linear strain paths. [16] Abaqus on the other hand is widely applied in the rubber industry and has one of the largest element and material model libraries. To investigate the difference between the conventional (Abaqus) and the updated Lagrangian (AniForm) solution methods a comparison is made between the different software packages.

In this Chapter the importance of mesh alignment to prevent intra-ply shear locking is investigated in Section 4.1. Section 4.2 discusses the mesh requirements and meshing approaches that satisfy these requirements. In Section 4.3 the analyses of a pneumatic muscle using different mesh approaches are compared. Some of these approaches are validated using experimental results of a single layered expansion joint in Section 4.4. A convergence study for the different mesh approaches is performed in Section 4.5. Section 4.6 explains a method for automated mesh generation of aligned fibre meshes in multi-layered products. This multi-layered model is validated using experimental data of an actual expansion joint design in Section 4.7. The causes of the convergence issues encountered are discussed in Section 4.8 and recommendations are made to improve the robustness of the analysis. At last, a trade-off is made between the different software packages and mesh types in Section 4.9.

4.1 MESH-FIBRE ALLIGNMENT

Intra-ply shear locking is a numerical phenomenon that overestimates intra-ply shear stiffness in membrane elements. This obstructs realistic fibre reorientation in highly-anisotropic materials and results in inaccurate structural analysis results. [17]

The extent of intra-ply shear locking depends on the level of anisotropy, being the ratio between the stiffness of the fibre and the matrix material. In regular matrix composites, with a degree of anisotropy ranging from 50-200, the effect is insignificant. On the other hand it has a major influence on thermoplastic composite forming simulations with degrees of anisotropy ranging up to a million. The degree of anisotropy of cord-reinforced rubber is somewhere in between 500-5000. Therefore it has to be investigated whether intra-ply shear locking is present in the simulation of these materials.

Research has shown that one way to eliminate intra-ply shear locking is by aligning linear triangle elements with the fibre direction. [17] To investigate the effects of intra-ply shear locking, aligned and unaligned meshes of a pneumatic muscle are compared. This pneumatic muscle is a cord-reinforced rubber that experiences large fibre reorientations. It has been used to validate both analytical and numerical models in previous research. [7, 18, 19] In the simulation the pneumatic muscle is pressurized to 5 [bar] causing axial contraction. Next, an axial load is applied at one end, extending the muscle again. These load cases for a model with aligned rebar triangle elements and a model with aligned truss elements are shown in Figure 4.1.

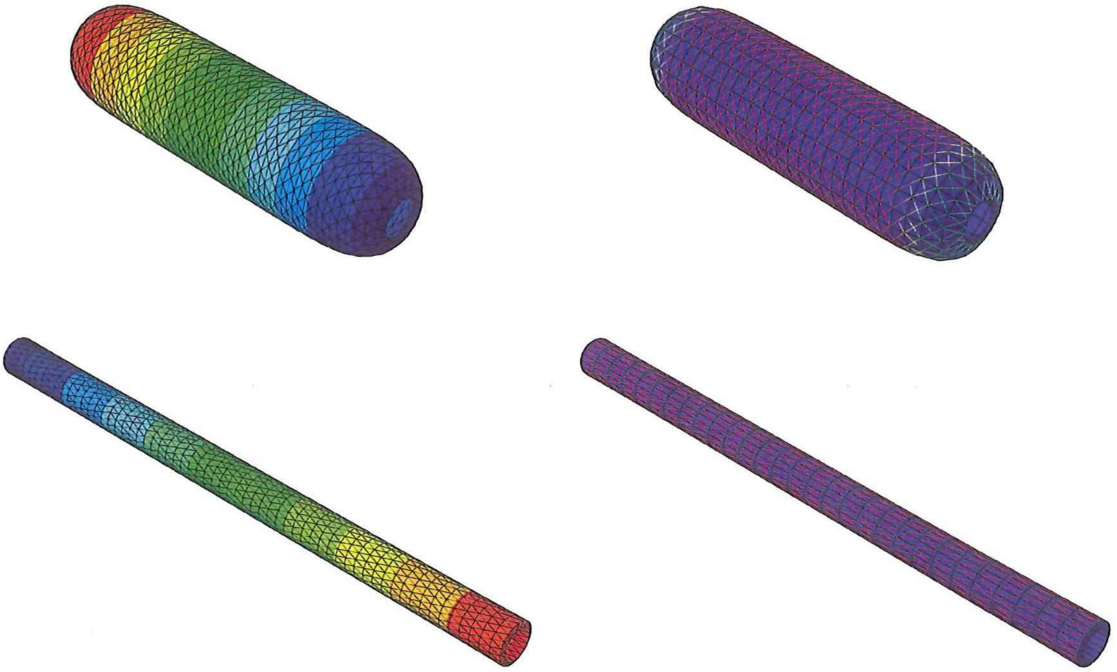

FIGURE 4.1: DEFORMATION MODES
LEFT: ALIGNED TRIANGLE ELEMENTS, RIGHT: ALIGNED TRUSS ELEMENTS
TOP: PRESSURIZED, BOTTOM: PRESSURIZED AND STRETCHED

The undeformed fibre angle with respect to the axis of revolution is 17,68°. The applied axial load of this muscle with respect to the axial stretch at a pressure of 5 [bar] is calculated. The indicated angle describes the angle of the edges of the triangle elements with respect to the axis of revolution. In Figure 4.2 the results for the aligned and various unaligned meshes calculated using Abaqus are shown. Figure 4.3, shows the results calculated by AniForm, using the exact same mesh geometry. The internal geometry, fibre angles and material properties of the pneumatic muscle are shown in Appendix A.1.

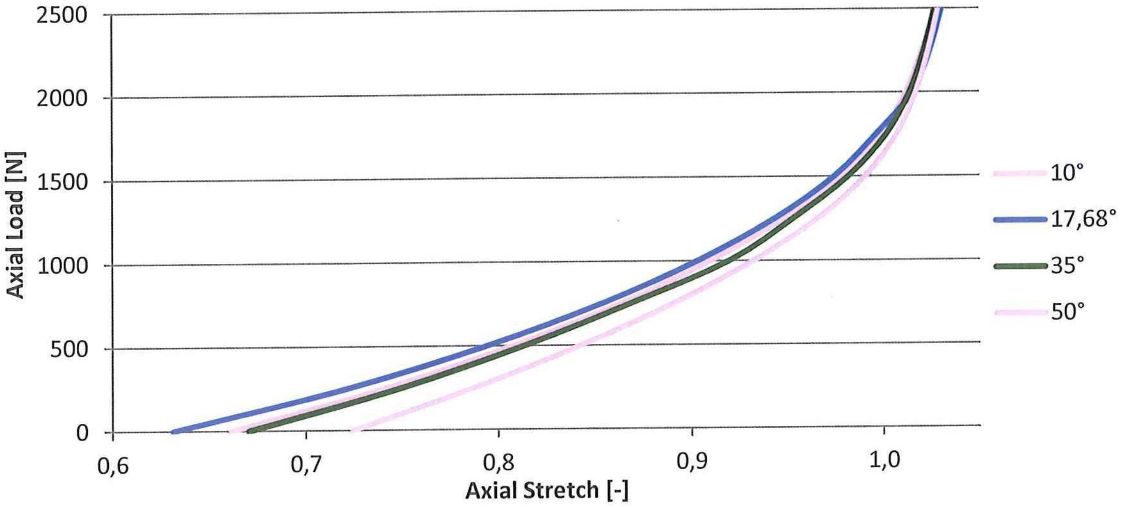

FIGURE 4.2: ABAQUS UNALIGNED MESH RESPONSE

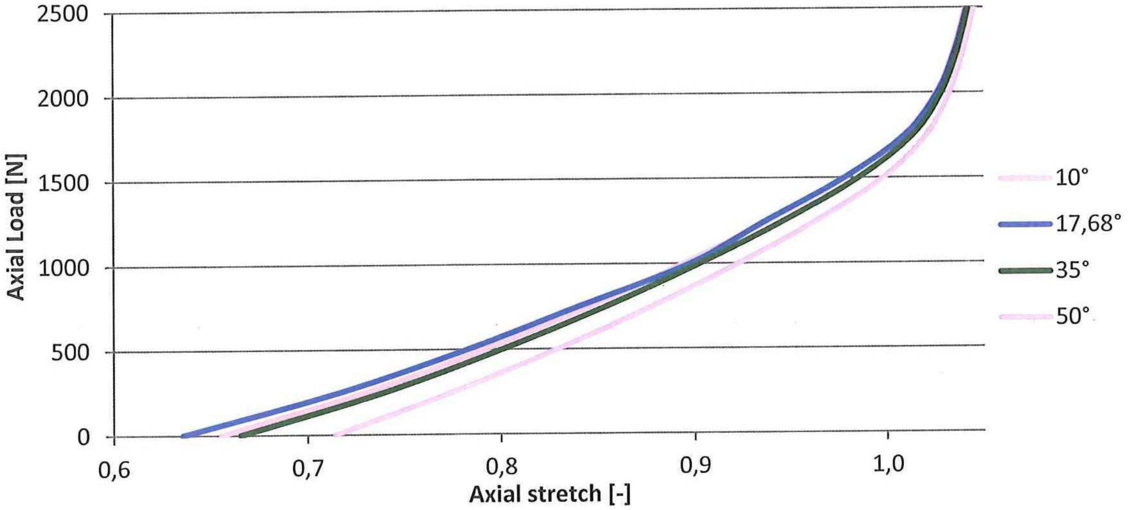

FIGURE 4.3: ANIFORM UNALIGNED MESH RESPONSE

As can be seen the effect of intra-ply shear locking is present. As the degree of misalignment increases, the pneumatic muscle tends to become stiffer. Although the effect is less pronounced in Aniform, it is still clearly visible. The use of an updated Lagrangian material model thus shows little improvement with respect to a finite deformation approach on element level as used in Abaqus. The effect of intra-ply shear locking is relatively small up to a misalignment of 20°. However, cord-reinforced rubber products can have a winding angle range of 5° to 90°. Therefore it is best to use aligned fibre meshes that ensure the best simulation accuracy for a wide range of products.

4.2 MESH

An important part of FEA is the way the product is discretized, better known as the mesh. Depending on the element types and material models available there are different approaches to discretize a product and its behaviour. Subsequently the approach determines the results that can be generated by the model and the computational efficiency at which the results are generated. In this Section the mesh requirements will be discussed as well as multiple approaches that satisfy these requirements.

4.2.1 REQUIREMENTS

Cord-reinforced rubbers show characteristics that have to be accounted for when modelling them using FEA. The most important is fibre shearing due to finite deformations. To account for this effect it is important that such fibre shearing is incorporated in the element/material behaviour. Another important effect is the hyperelastic material behaviour that has to be incorporated in the applied material models.

Section 4.1 has shown that the fibre mesh has to be aligned with the fibre direction. As each fibre layer needs to be aligned with its own fibre direction, it is not possible to combine multiple layers into a single element layer. Each fibre layer has to be modelled by a separate layer of elements. The connection of unaligned layers can only be achieved by modelling a 3-dimensional rubber layer.

4.2.2 APPROACHES

An overview of the available mesh approaches for cord-reinforced rubber expansion joints is shown in Figure 4.4. One approach is to separate the fibre and rubber elements. As the fibres only possess significant in-plane stiffness, their out-of-plane behaviour can be neglected. Therefore they can be modelled using membrane, shell or truss elements.

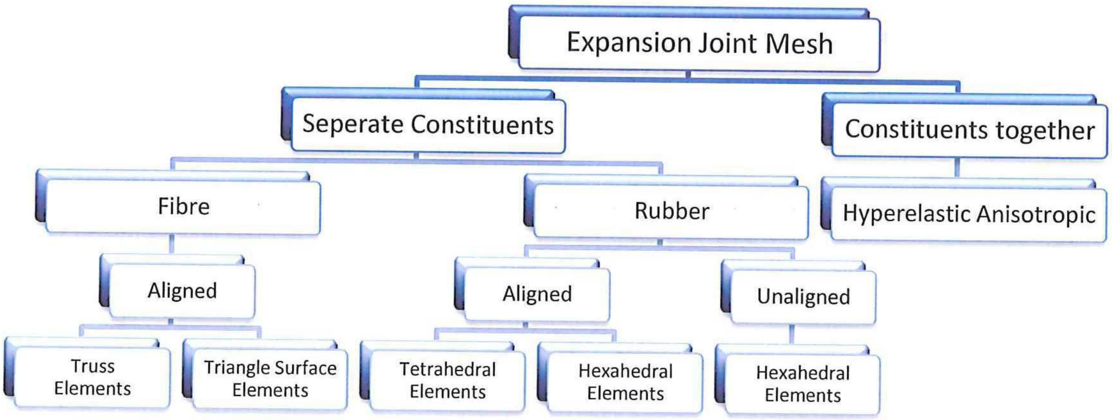

FIGURE 4.4: EXPANSION JOINT MESH APPROACHES

In Aniform the fibre layer can only be modelled using linear triangular membrane or shell elements. To prevent intra-ply shear locking these elements have to be aligned with the fibre directions. The fibre shearing effect is incorporated in an updated Lagrangian material model. The only 3D solid elements available in Aniform are linear or quadratic tetrahedral elements.

In Abaqus a similar approach can be applied. A major difference is the method of accounting for fibre shearing. Whereas Aniform accounts for this behaviour within the material model, Abaqus uses so called "rebar" elements. The rebar element description only attributes one-dimensional material properties to the element in a given direction and rotates this principal material direction to account for the fibre shearing. Abaqus thus handles fibre-shearing on element level, whereas Aniform handles this effect on a material level.

Another approach that is available in Abaqus is to model the fibres or groups of fibres separately as truss elements aligned with the actual fibre directions. One important advantage is that truss elements do not encounter intra-ply shear locking.

The last approach is to model the fibres and rubbers together using an anisotropic hyperelastic material model. These describe the interaction between the rubber and fibres within a single material definition. A downside of such material models is that they require various combined material properties as input. As these material properties are difficult to determine without experimental testing, the application of these material models becomes unpractical.

4.3 FINITE ELEMENT ANALYSIS COMPARISON

Now the different meshing approaches have been determined, a comparison between these methods has to be made. For this comparison the same product (pneumatic muscle) and load cases are used as in Section 4.1. First of all there is the comparison between the different software packages. Furthermore the fibre and rubber element types are varied. The different meshing approaches that are evaluated are listed in Table 4.1.

TABLE 4.1: ANALYSIS CONFIGURATION

Approach	Software	Fibre Elements	Rubber Elements
1	Abaqus	Linear Triangles	Linear Tetrahedrals
2	Abaqus	Linear Triangles	Quadratic Tetrahedrals
3	Abaqus	Quadratic Triangles	Quadratic Tetrahedrals
4	Aniform	Linear Triangles	Linear Tetrahedrals
5	Aniform	Linear Triangles	Quadratic Tetrahedrals
6	Abaqus	Linear Truss	Linear Hexahedrals
7	Abaqus	Quadratic Truss	Quadratic Hexahedrals
8	Abaqus	Linear Triangles	Linear Hexahedrals (Unaligned)

The first five mesh approaches are made using aligned triangle elements for the fibres and tetrahedral elements aligned with these triangle elements, as depicted on the left side of Figure 4.1. To investigate the influence of the order of the element both linear and quadratic elements and combinations of these are tested. The 1st order linear elements are limited to a constant stress throughout each element, where the stress in a quadratic element can vary linearly. Quadratic elements are thus better able to model regions with large stress gradients. However, quadratic elements require more nodes and thus more degrees of freedom, increasing the computational cost of these elements. By comparing different order elements it can be investigated whether the additional computational cost of higher order elements improves the solution accuracy and/or convergence.

Next to the mesh approaches with aligned triangle elements, some models are made using truss elements to model the fibres. In these approaches, each fibre is modelled separately, eliminating the risk of intra-ply shear locking. The first two models use aligned hexahedral meshes for the rubber of which the nodes coincide with the fibre nodes, as depicted on the right side of Figure 4.1. The last model uses unaligned hexahedral elements which are bound to the fibres using a so called "embedded" constraint in which the nodal surface of the fibre elements is fixed within the hexahedral elements. [20] This method is most suitable for automated mesh generation as the fibre geometry does not have to be accounted for when discretizing the rubber.

To investigate the behaviour of all the different mesh approaches, three important parameters are compared throughout the whole deformation spectrum of the product. These three parameters are the axial reaction force (Figure 4.5), the maximum fibre stress (Figure 4.6) and the maximum rubber strain (Figure 4.7), all with respect to the axial stretch of the pressurized pneumatic muscle. The deformed geometries of the pneumatic muscle are illustrated in Figure 4.1.

As can be seen in Figure 4.5, there is little variation between the different meshing approaches with respect to the axial reaction force. The variation in element types for the rubber has little effect in this case as the behaviour of the total product is mainly determined by the stiff fibres and not by the flexible rubber of the pneumatic muscle. When compared to the measured results, the stretch levels differ. This is due to fibre plasticity. [18]

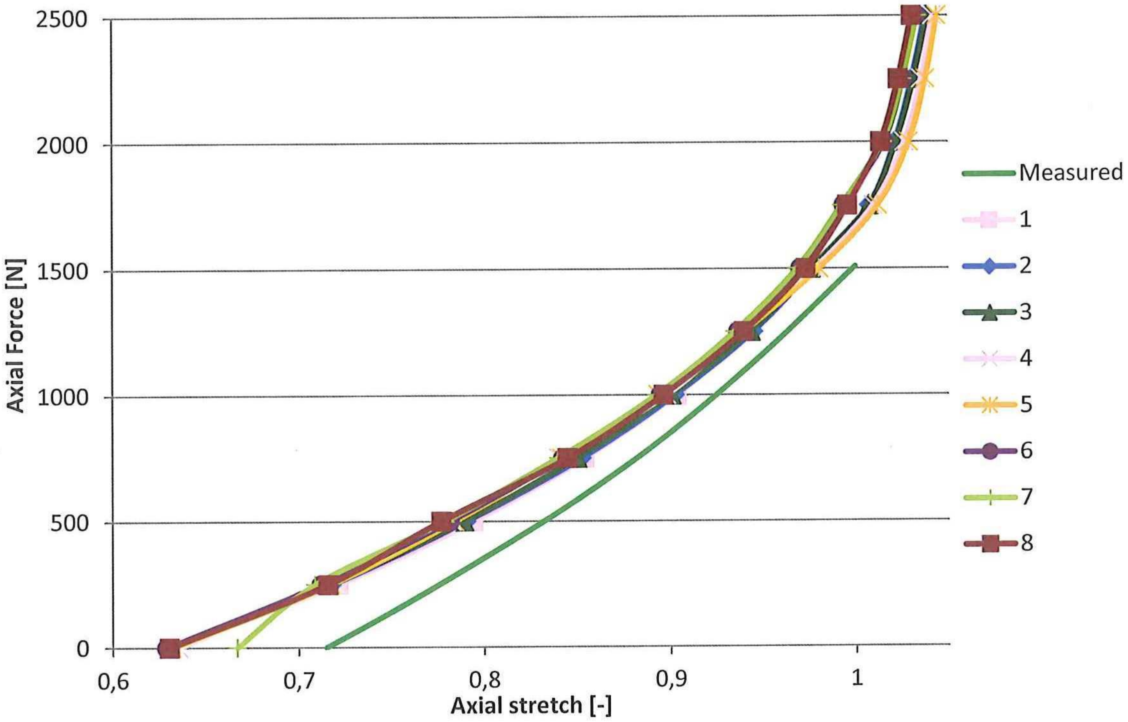

FIGURE 4.5: AXIAL STRETCH VS. AXIAL FORCE

Figure 4.6 shows the maximum fibre stress with respect to the axial stretch. In comparison with the axial reaction force there is more variation between the different meshing approaches. As can be seen there is one divergent approach, this is the only model that uses quadratic triangle elements for the fibres. The cause of this deviation is that in this model the highest fibre stresses are given at the edges whereas in the other models the highest fibre stresses are given in the middle. However, the stresses in the middle of this quadratic triangle model match with the other models.

It is known that boundary conditions can result in overestimated stresses. These overestimated stresses only show in the quadratic elements as these elements are the only elements that allow for large stress gradients, allowing this asymptotic behaviour at the boundaries. Apart from these overestimated stresses at the boundaries, all other fibre stresses throughout this model match with the values of the other models.

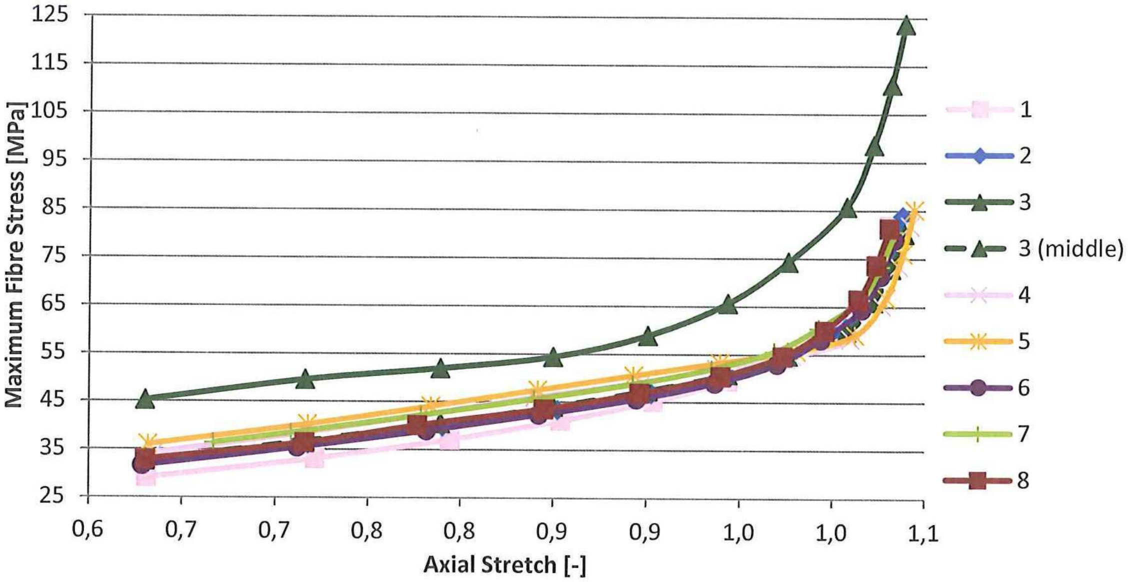

FIGURE 4.6: AXIAL STRETCH VS. MAXIMUM FIBRE STRESS

Figure 4.7 shows the maximum principal rubber strain in the model with respect to the axial stretch. From all the parameters this graph shows the biggest variation between the different models. It should be noted that the Aniform results are not included as this software is unable to provide strains that are comparable with the Abaqus strain definition.

The fully linear models (1, 6 and 8) match quite well up to a stretch of approximately 1. Above this stretch the unaligned hexahedral model (8) starts to deviate. This is likely caused by the fact that this model has multiple elements through the thickness of the rubber and is thus able to predict a strain gradient throughout the thickness, whereas the other linear models give a constant strain throughout the thickness.

When the higher order element approaches are compared with the linear elements they give significantly higher rubber strains. Again this effect is likely to be caused by the strain gradient through the thickness of the rubber. Furthermore the quadratic triangle models (2 and 3) show some unexpected perturbations at high stretch levels. These perturbations can be attributed to a shifting location of highest rubber strain from the middle of the product to the edges. Where this is a smooth transition in the linear models, this location jumps back and forth in the quadratic triangle models.

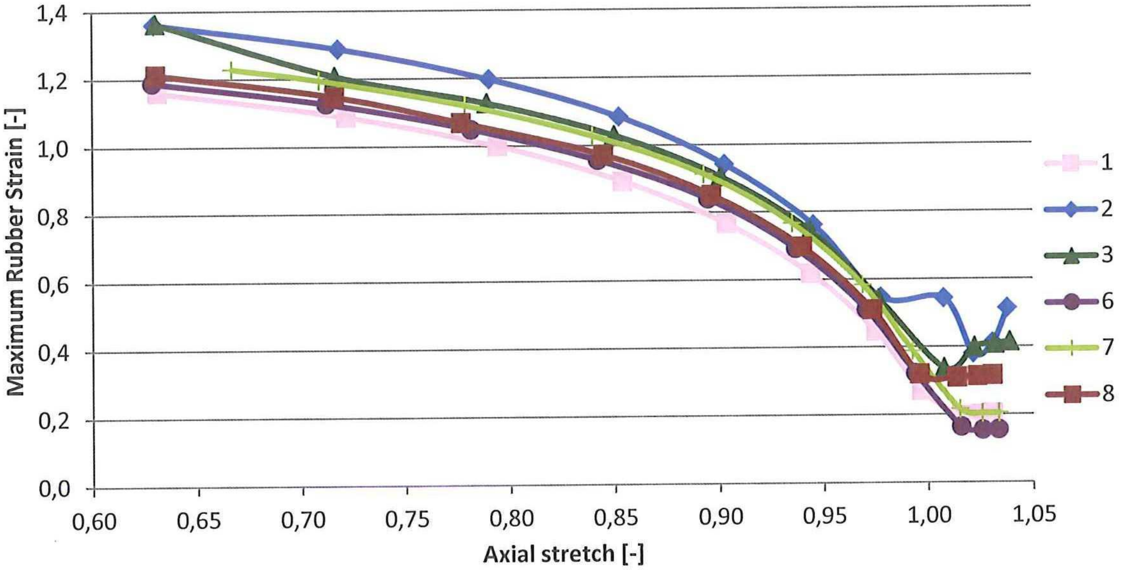

FIGURE 4.7: AXIAL STRETCH VS. MAXIMUM RUBBER STRAIN

4.4 EXPANSION JOINT COMPARISON

Section 4.3 compared the different meshing approaches for a standardized pneumatic muscle. In this Section a comparison is made with actual test results of a single layered expansion joint. The internal geometry, fibre angles and material properties of the single layered expansion joint are shown in Appendix A.2.

In the previous Section models have been made with hexahedral elements aligned with truss elements for the fibres. These mesh approaches have not shown any significant improvement with respect to the unaligned hexahedral with embedded triangle element approach. Furthermore these meshes are difficult to construct for expansion joints with varying fibre angles and radii. Therefore these two methods are omitted from the comparison. Table 4.2 shows the remaining mesh approaches that are evaluated in this Section.

TABLE 4.2: EXPANSION JOINT ANALYSIS CONFIGURATIONS

Approach	Software	Fibre Elements	Rubber Elements
1	Abaqus	Linear Triangles	Linear Tetrahedrals
2	Abaqus	Linear Triangles	Quadratic Tetrahedrals
3	Abaqus	Quadratic Triangles	Quadratic Tetrahedrals
4	Aniform	Linear Triangles	Linear Tetrahedrals
5	Aniform	Linear Triangles	Quadratic Tetrahedrals
8	Abaqus	Linear Triangles	Linear Hexahedrals (Unaligned)

Figure 4.8 shows the measured and simulated elongation of a single layered expansion joint during unrestricted pressurization. In this case high elongations result from the closed end conditions of the pipe causing high axial tensile forces. When comparing the different meshing approaches among each other they all match quite well.

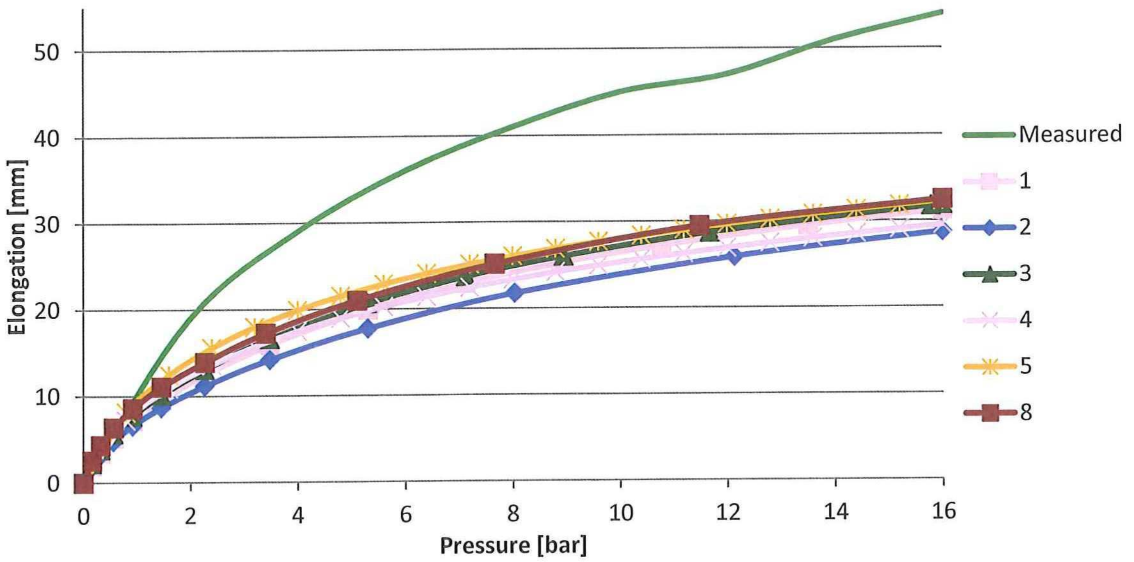

FIGURE 4.8: UNRESTRICTED ELONGATION VS. PRESSURE

The Abaqus models with linear tetrahedral elements (1 and 2) behave slightly stiffer than the rest. This is due to the fact that the hybrid tetrahedral element formulation in Abaqus is overconstrained causing a small degree of volumetric locking. [21] However, for the modelling of the nearly incompressible rubber the hybrid element formulation is required to achieve convergence of the non-linear analysis.

Although the different meshing approaches match quite well, the stifness of the actual expansion joint is much lower. There are two causes for this discrepancy. First of all the top layer of the rubber at the flange ends was not well vulcanized, causing it to rupture at the flange ends at a rather small elongation as can be seen in Figure 4.9. This event exposed the fibre layer and showed poor fibre-rubber bonding at the cylindrical parts of the expansion joints which was likely to be caused by the poor vulcanization as well.

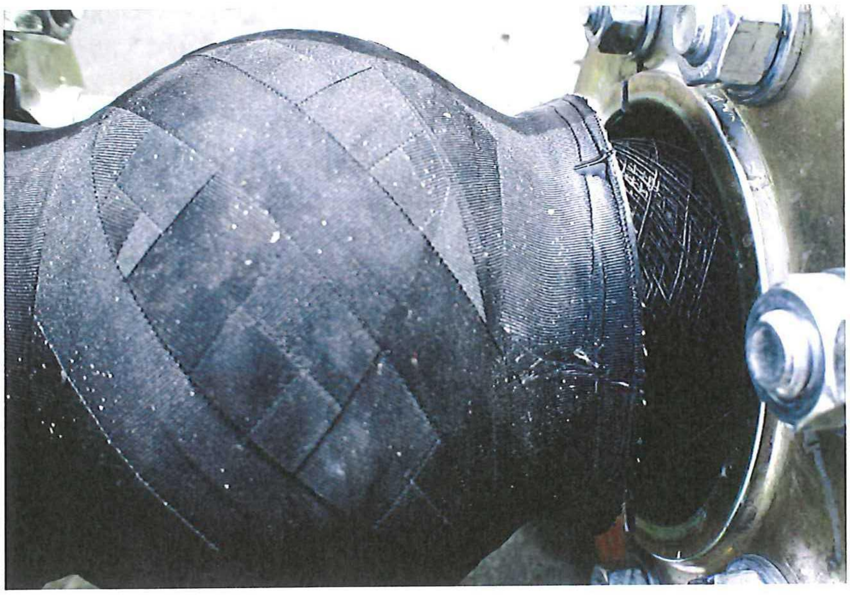

FIGURE 4.9: RUPTURED OUTER RUBBER IN SINGLE-LAYERED PROTOTYPE

As the winding angle at the cylindrical regions is far from geodesic, the fibres tend to shear towards the direction of maximum stress, causing significant axial elongation. During the measurements it was clearly visible that the majority of the elongation was achieved in the cylindrical region as the bellow was able to retain it's shape. In typical expansion joints additional axial reinforcement layers are placed at these locations to limit the elongation of the cylindrical region. Therefore the ruptured prototype is not representative for actual expansion joints. A comparison with realistic expansion will be made in Section 4.7.

Next to the unrestricted pressurization load case, the different meshing approaches are compared among each other in different realistic load cases. These load cases are illustrated in Figure 4.10 and represent the most extreme deformations throughout the testing program for high-performance expansion joints. Both the reaction forces and the maximum fibre forces are compared for each of the load cases. The results of the different simulations are listed in Table 4.3 together with the standard deviation as a percentage of the average result.

TABLE 4.3: REACTION FORCES AND FIBRE FORCES DURING DIFFERENT LOAD CASES
* = NO RESULT DUE TO NON-CONVERGENCE

Load Case	Parameter	Mesh Approaches						σ [%]
		1	2	3	4	5	8	
Restricted Pressurized	Axial Reaction Force [N]	4090	3715	3693	4453	3951	4221	6,7
	Maximum Fibre Force [N]	144,9	141,3	139,9	141,6	142,1	144,7	1,3
Axial Elongation	Axial Reaction Force [N]	14629	13636	13397	14424	13419	15088	4,6
	Maximum Fibre Force [N]	165,0	160,5	161,4	162,6	165,9	164,6	1,2
Axial Compression	Axial Reaction Force [N]	-5258	-4216	-4205	-2235	-1756	-4945	34,9
	Maximum Fibre Force [N]	127,8	126,8	123,1	133,0	126,7	128,1	2,3
Lateral Deformation	Axial Reaction Force [N]	3864	*	4622	6023	6019	4241	18,2
	Lateral Reaction Force [N]	7576	*	5081	5357	4000	7874	25,1
	Maximum Fibre Force [N]	315,7	*	265,3	369,6	349,5	280,4	12,5

As can be seen the relative variation in the maximum fibre forces is very low in the axisymmetric load cases. Furthermore the variation in reaction forces in the restricted and elongated cases is satisfactory as well. In the compressive case there is however a large variation between the results of Aniform (4 and 5) and Abaqus (1, 2, 3 and 8). In the compressive simulation of Aniform kinking occurs at the end of the bellow where this does not occurs in the simulation of Abaqus. This kinking is responsible for the difference in compressive stiffness between the two software packages.

The non-axisymmetric lateral load case shows a large variation in both the reaction forces and the maximum fibre force. During the lateral analysis it is much more difficult for the models to converge than in the axisymmetric cases. This indicates a higher level of non-linearity in this problem. Furthermore the stress and strain gradients during this load case are much higher than in any of the other cases. Therefore the use of linear elements is less suitable to achieve an accurate result.

In general the quadratic models behave less stiff than the linear models as these experience less volumetric locking than the linear hybrid tetrahedral elements. However, as the linear models slightly overestimate the fibre forces in every case, these computationally efficient models are a suitable conservative choice for the analysis of expansion joints.

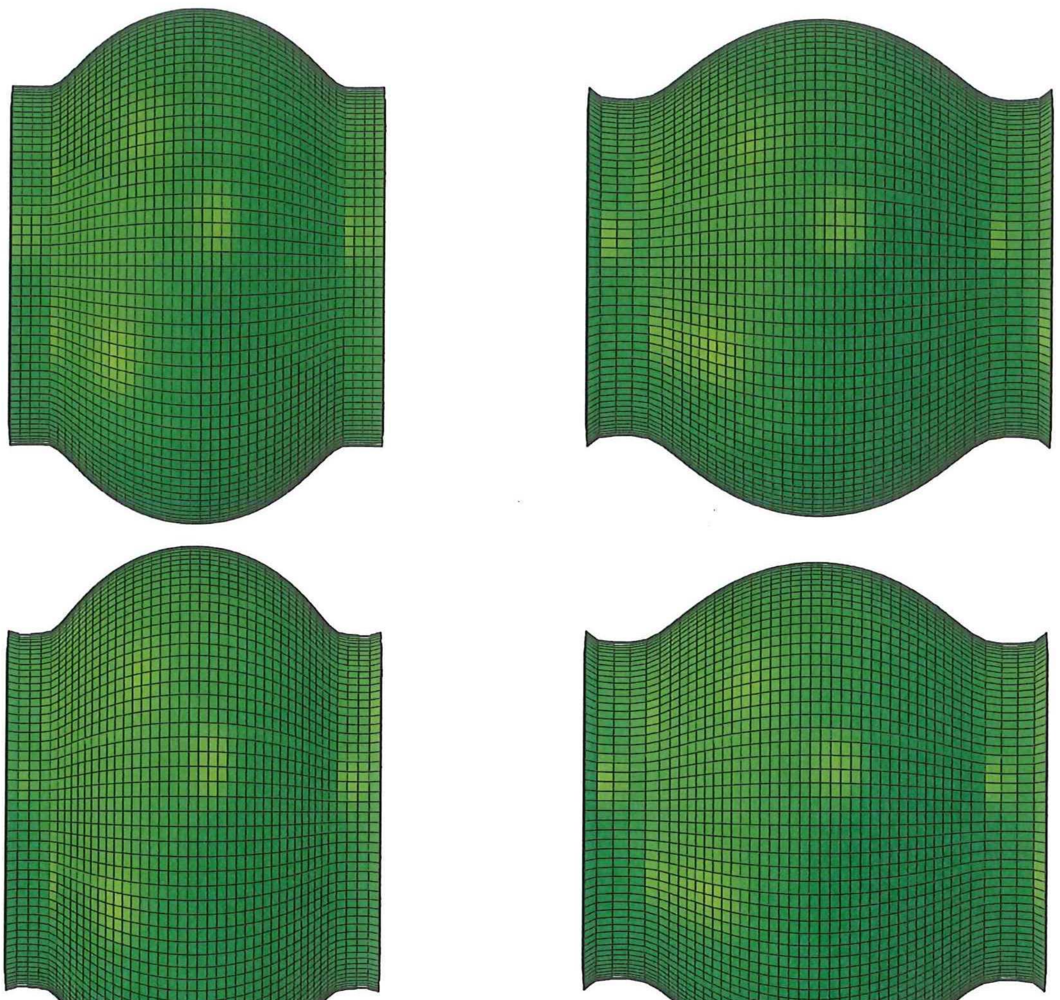

FIGURE 4.10: EXPANSION JOINT LOAD CASE DEFORMATION
TOP-LEFT: UNDEFORMED, TOP-RIGHT: UNRESTRICTED PRESSURIZED
MIDDLE-LEFT: RESTRICTED PRESSURIZED, MIDDLE-RIGHT: 30 [MM] ELONGATION
BOTTOM-LEFT: 30 [MM] COMPRESSION, BOTTOM-RIGHT: 30 [MM] LATERAL DEFLECTION

4.5 CONVERGENCE STUDY

In this Section a convergence study is performed to determine which mesh densities are sufficient to give a converged solution. The convergence of the total reaction force, the maximum fibre force and the maximum rubber strain are investigated. This is done for the restricted pressurized load case illustrated in Figure 4.10.

As there is a minimum number of elements required to describe the expansion joint geometry this determines the coarsest mesh. On the other hand the finest mesh is constrained by the memory size of the computer as the analysis storage has to fit within the memory. As the final model should be able to run on a regular workstation, this limits the maximum number of elements.

For the convergence study the relative error is determined with respect to the finest mesh that was able to run. Figure 4.11 shows the convergence of the axial reaction force as a function of the degrees of freedom. As can be seen every model shows some level of convergence, however the error of the quadratic models (2, 3 and 5) remains too high. The linear models (1, 4 and 8) on the other hand show satisfactory convergence (< 5%), even with relatively coarse meshes.

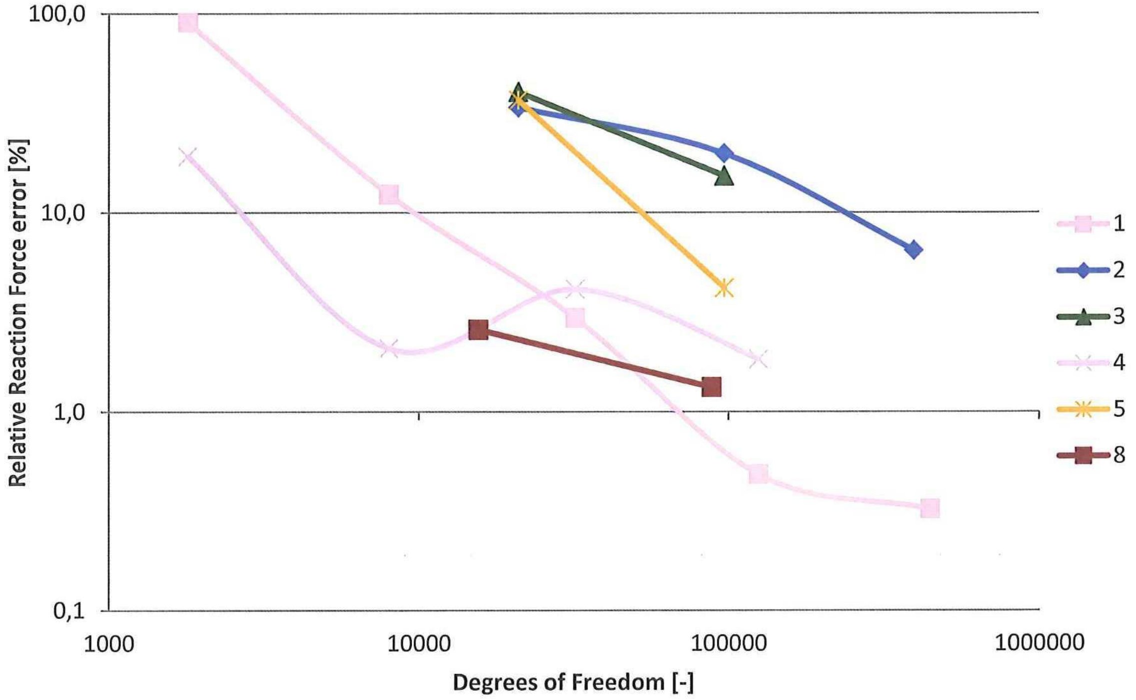

FIGURE 4.11: RESTRICTED REACTION FORCE CONVERGENCE

Figure 4.12 shows the convergence of the maximum fibre force in the model. Just as with the axial reaction force, all the models show some level of convergence and the linear models converge better than the quadratic models. It should be noted that here the benefits of the updated Lagrangian material model of Aniform show as even the coarsest Aniform model shows satisfactory convergence.

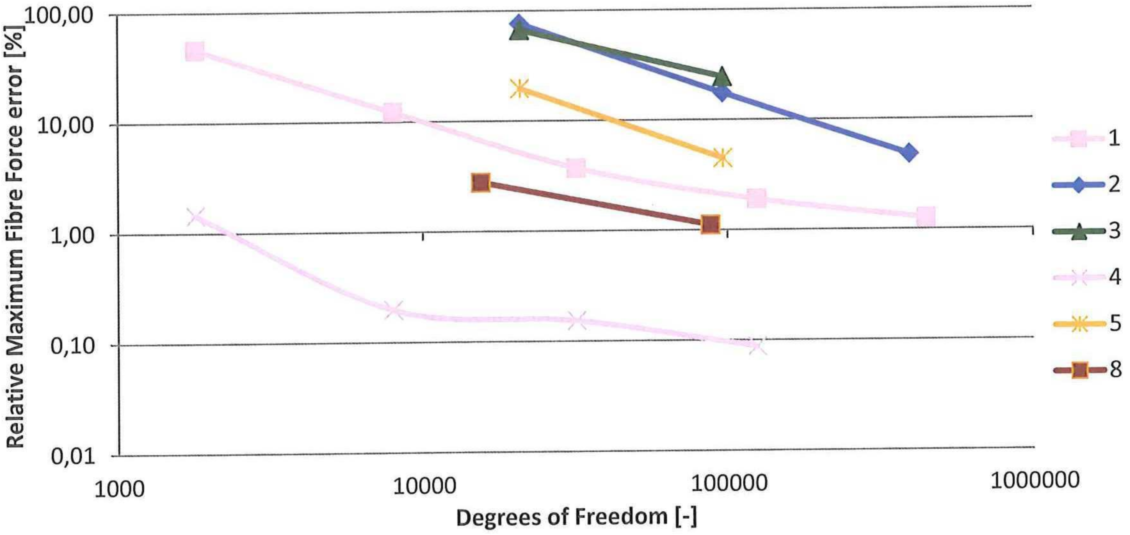

FIGURE 4.12: RESTRICTED MAXIMUM FIBRE FORCE CONVERGENCE

The maximum principal rubber strain convergence is shown in Figure 4.13. Just as in Figure 4.6 the Aniform results are not included as the software is unable to provide strains that are comparable with Abaqus its strain definition. Where the axial reaction force and maximum fibre force showed convergence in all the mesh approaches, this is not the case for the maximum principal rubber strain. All the models using tetrahedral elements do not show satisfactory convergence or even any form of converging rubber strains at all. The only approach that shows sufficient convergence is the unaligned hexahedral model (8). These linear hexahedral elements do not show the inherent volumetric locking of the linear tetrahedral elements. The hexahedral elements are not over constrained by the hybrid element definition used for the modelling of incompressible materials. [22] Furthermore it is possible to have multiple elements through the thickness while maintaining limited degrees of freedom. Therefore this is the only approach suitable to simulate meaningful rubber strains. On the other hand the linear tetrahedral models (1 and 4) do show sufficient convergence for the simulation of fibre stresses and reaction forces.

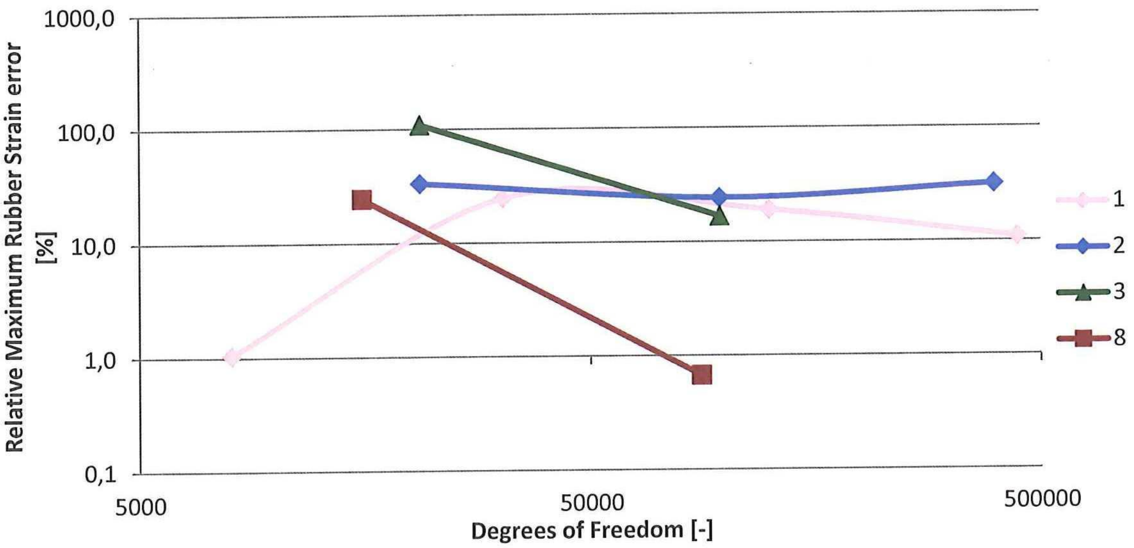

FIGURE 4.13: RESTRICTED MAXIMUM RUBBER STRAIN CONVERGENCE

4.6 MULTI-LAYERED ALLIGNMENT

In the previous Sections two products have been modelled that both contain a single fibre layer. To be able to model all the different types of cord-reinforced rubbers, multi-layered products have to be modelled as well. As the fibre layers have to be modelled using aligned meshes as shown in Section 4.1, each fibre mesh layer has to be aligned with its own fibre orientation. These different fibre layers have to be connected to each other using 3-dimensional rubber elements as indicated in Section 4.2. One method to connect these aligned fibre meshes, is by aligning the rubber element nodes with the fibre nodes. This automated mesh generation method will be discussed in this Section.

Figure 4.14 shows aligned triangle meshes of a single layered and multi layered expansion joint. Each fibre mesh can be seen as a collection of rings aligned with that fibre section. The rings of different fibre layers can be connected by discretizing the solid in between into circumferential cones as illustrated in Figure 4.15 for a multi-layered expansion joint.

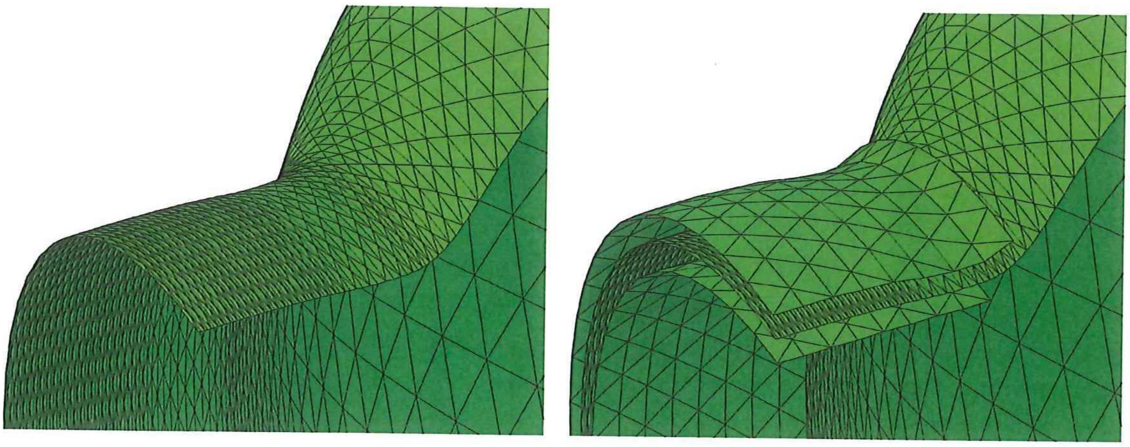

FIGURE 4.14: ALIGNED TRIANGLE MESHES
LEFT: SINGLE LAYERD, RIGHT: MULTI-LAYERED

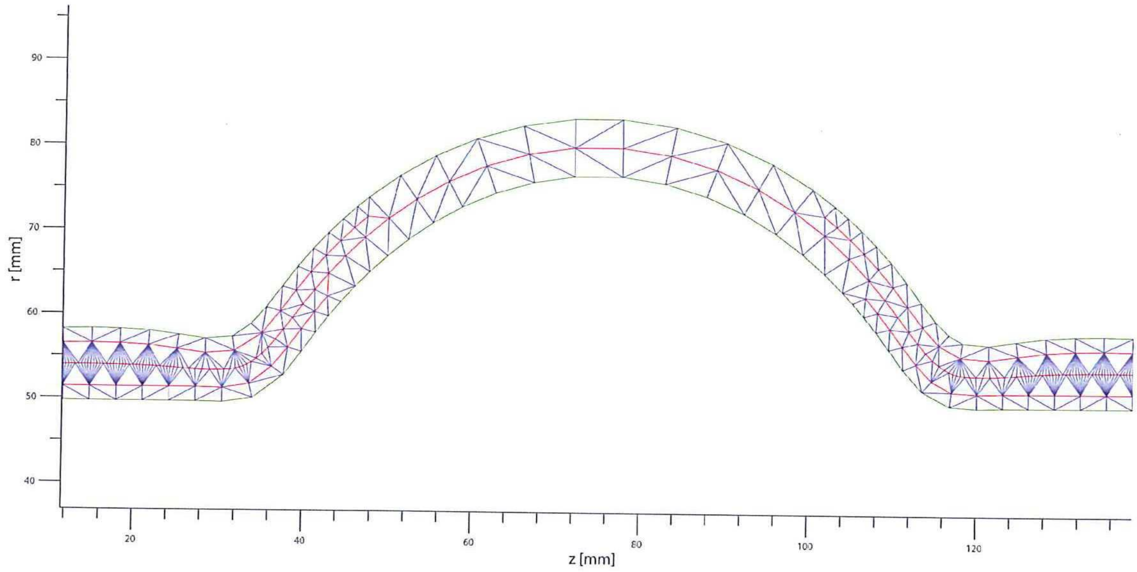

FIGURE 4.15: CONE DISCRETIZATION IN Z-R PLANE

After this step a large number of circumferential rings are left for the modelling of the rubber. The next step is to discretize this ring into single wedge sections. A single circumferential cone and wedge section are illustrated in Figure 4.16. This single wedge section can now easily be discretized into three tetrahedral elements.

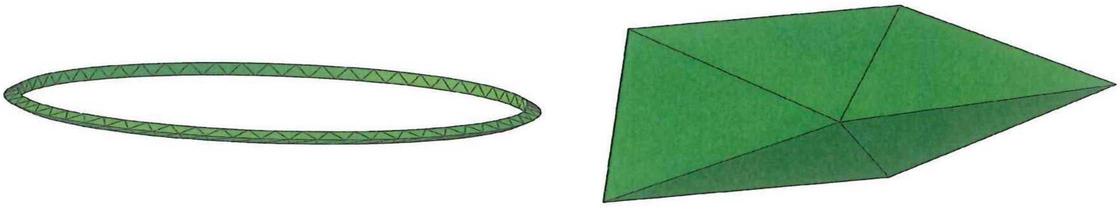

FIGURE 4.16: DISCRETIZED CONE AND WEDGE SECTION
LEFT: SINGLE CIRCUMFERENTIAL CONE SECTION, RIGHT: SINGLE CONE WEDGE SECTION

By automating these discretization steps, multi-layered aligned tetrahedral elements can be generated efficiently. Figure 4.17 shows cross section cuts of an aligned tetrahedral mesh for the connection layer between the fibre layers and for a whole expansion joint.

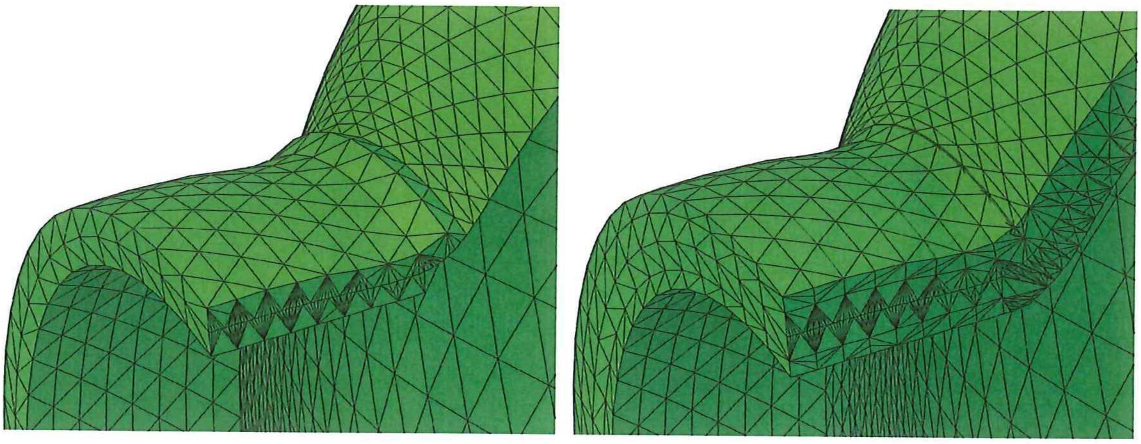

FIGURE 4.17: CONNECTED ALIGNED FIBRE MESHES
LEFT: INTER-PLY RUBBER, RIGHT: COMPLETE EXPANSION JOINT

4.7 MULTI-LAYERED EXPANSION JOINT

Where the previous mesh comparisons were made for single-layered products, this Section investigates the behaviour of the different models in a multi-layered expansion joint. This multi-layered expansion joint design is part of a development project for one of the leading European expansion joint manufacturers. The internal geometry and fibre angles of the reinforced expansion joint are shown in Appendix A.4.

An extensive testing sequence has been performed on this expansion joint design. This test data will be used to validate the numerical models. For the validation a comparison is made for both axial and lateral deformations, unpressurized and at working pressure. Furthermore the measured and predicted burst pressures are compared. For this comparison the same models are used as indicated in Table 4.2. However, as not all models were able to converge in the compressive and/or lateral load cases, not all models are included in each comparison. The difficulties with convergence will be discussed in Section 4.8.

Figure 4.18 shows the axial load-displacement graph of an unpressurized expansion joint. As can be seen the Abaqus tetrahedral models (1, 2 and 3) overestimate the tensile stiffness of the expansion joint significantly. Both Aniform models (4 and 5) perform slightly better, but the most accurate simulation is done by the unaligned hexahedral model (8). It should be noted that the loop visible in the measured response is due to elastic hysteresis of the rubber which is not accounted for in the simulations.

Where most of the models overestimated the tensile stiffness, they underestimate the compressive stiffness. In this case the most accurate model is the Abaqus linear tetrahedral model (1) whereas all other models show approximately the same response. Furthermore there is a significant difference between the linear and quadratic elements, indicating that there are large strain gradients in the rubber. It is interesting to see that the large variation in the compressive response between Aniform and Abaqus as noted in Section 4.4 has disappeared as both models do not kink at the end of the bellow.

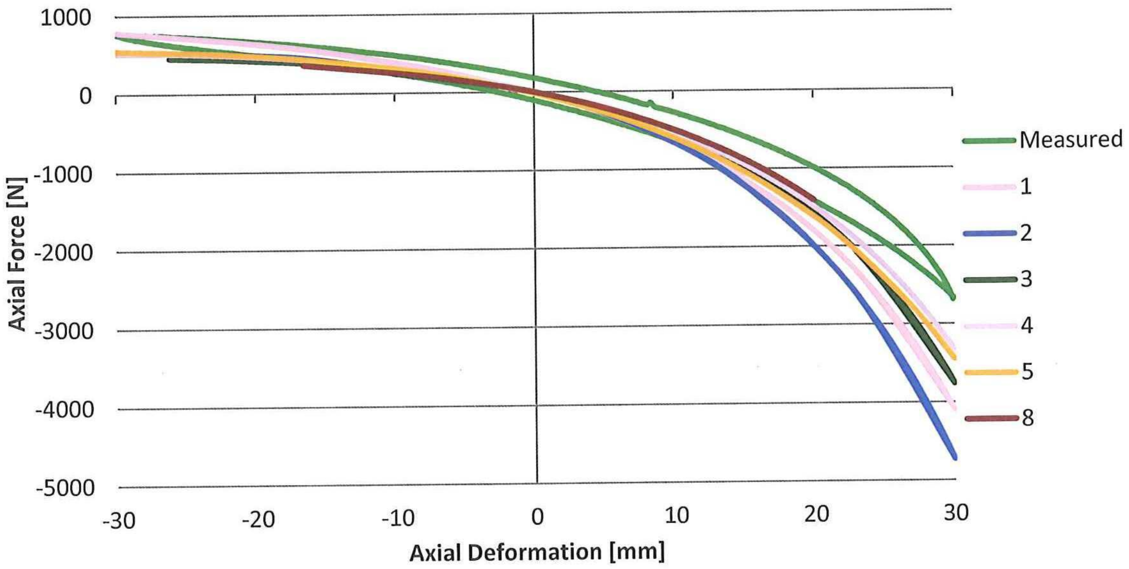

FIGURE 4.18: AXIAL DEFORMATION VS. AXIAL REACTION FORCE

The lateral load displacement graph of the unpressurized expansion joint is shown in Figure 4.19. Only the linear tetrahedral models (1 and 4) were able to give a converged solution over the whole deformation range. The models that were unable to converge all predicted some form of buckling, either locally in the cylindrical region or globally throughout the bellow.

In this graph there is a more pronounced difference between the different models. The Abaqus linear tetrahedral model (1) behaves overly stiff. This is caused by the inherent volumetric locking of this type of element. The use of higher-order rubber elements (2 and 3) shows a more realistic response. The variation between the linear and quadratic fibre element models indicates that there are large stress gradients in the fibres in this load case.

An interesting note is the large variation between the linear models of Abaqus and Aniform. This is partly caused by the fact that the linear tetrahedral elements in Aniform do not experience the inherent volumetric locking as the hybrid elements in Abaqus do. Furthermore the updated Lagrangian strain definition is more accurate in the modelling of the finite deformations.

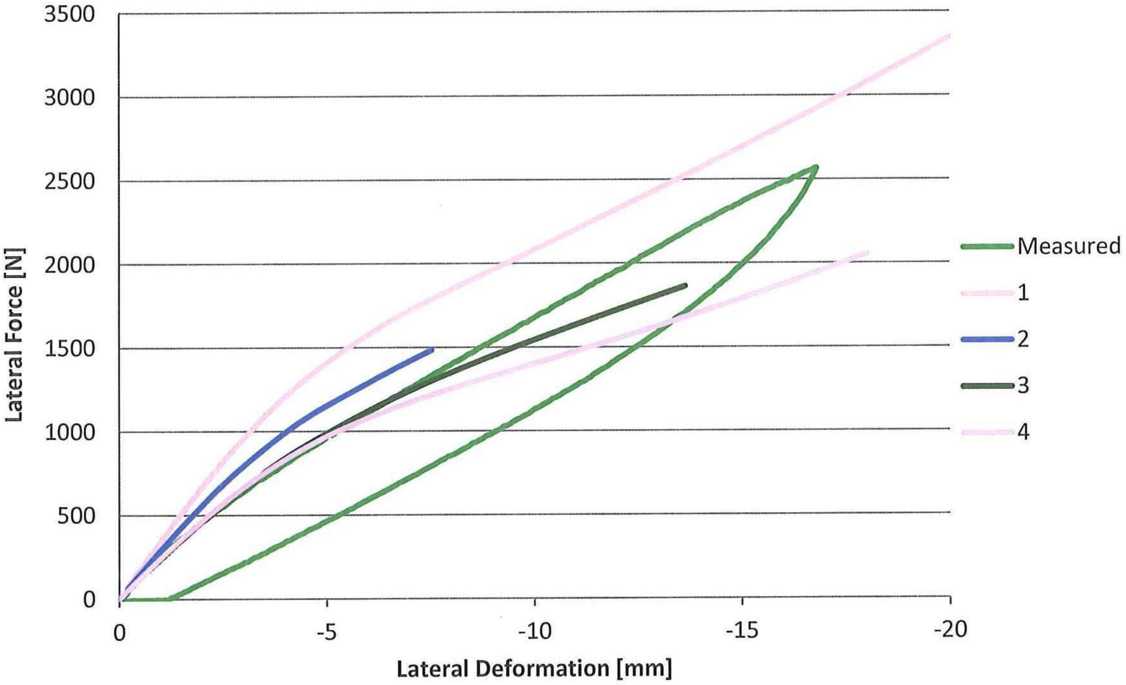

FIGURE 4.19: LATERAL DEFORMATION VS. LATERAL REACTION FORCE

The actual product specifications of the expansion joints tested in these cases restrict their use to maximum axial and lateral deformations of ±11 [mm]. The simulated axial response of the expansion joint in this deformation range is sufficiently accurate. Furthermore, the fully quadratic Abaqus and linear Aniform models show fair agreement with the lateral test results throughout this deformation range as well.

Next to the unpressurized stiffness response, the stiffness response at working pressure (16 [bar]) is simulated as well. Figure 4.20 shows the axial response of the pressurized expansion joint. Only the linear models were able to give a converged solution of a restricted expansion joint at working pressure. As this is the starting point for the stiffness responses, only the simulation of these linear models could be determined.

As can be seen, the unaligned hexahedral (8) and linear tetrahedral (1) models show little variation. This indicates that the through-thickness strain distribution, which is better predicted by the hexahedral model, does not have a significant effect on the pressurized axial stiffness. Furthermore both Abaqus models overestimate the axial stiffness. The Aniform model (4) shows a more flexible response, which can again be attributed to the updated Lagrangian method and its ability to better predict the finite deformations. However, all of the models overestimate the stiffness significantly. This could be due to inaccurate rubber material parameters or due to poor rubber-fibre bonding in the cylindrical section as mentioned in Section 4.4. The effect of more advanced rubber material models on the results will be investigated in Chapter 5.

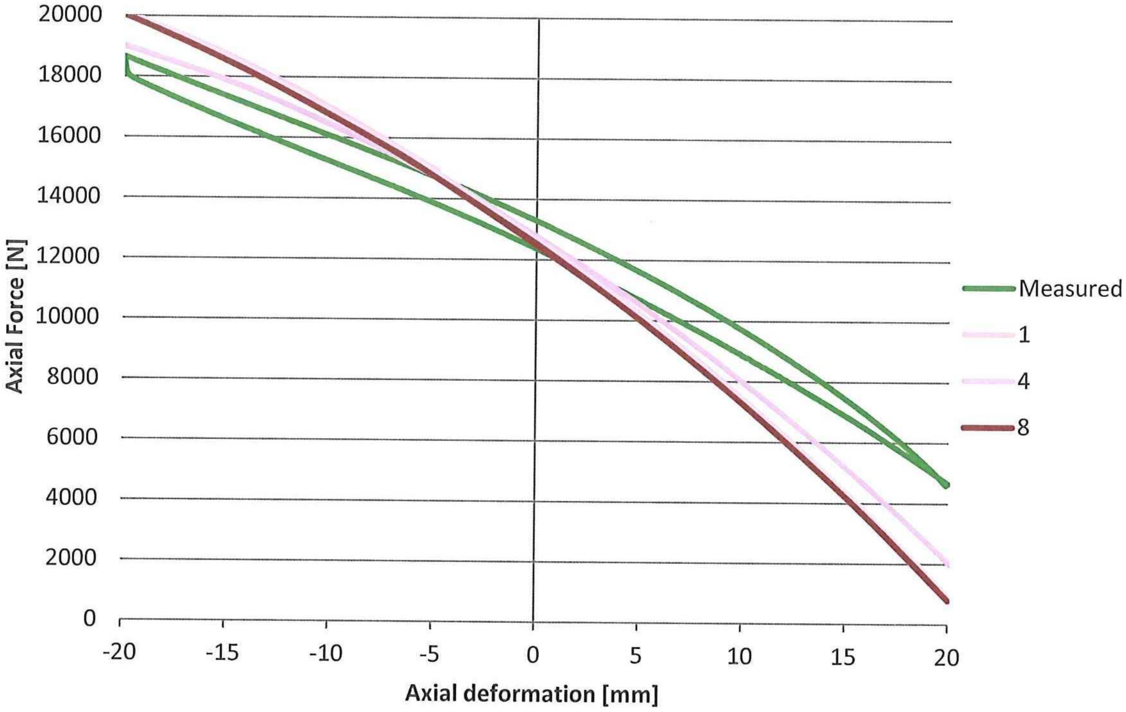

FIGURE 4.20: PRESSURIZED AXIAL DEFORMATION VS. AXIAL REACTION FORCE

The lateral pressurized load displacement graph is shown in Figure 4.21. In contrast with the axial deformation there is a slight difference between both Abaqus models. This indicates that the through-thickness strain distribution does have an effect on the pressurized lateral stiffness. Furthermore the Aniform model shows a more flexible lateral response. However, in this case the stiffer Abaqus response matches better with the test results.

In general it can be concluded that the linear tetrahedral gives the most stiff response, due to volumetric locking. The influence of the volumetric locking has a less pronounced effect in pressurized simulation as in this case volumetric locking is likely to occur in the other models as well. The AniForm models are less prone to volumetric locking as the updated Lagrangian solution method is better able to cope with finite deformations. Therefore AniForm gives the most flexible responses. Furthermore it can be concluded that through-thickness strain gradients do have an effect in most load cases. Therefore it is recommended to use elements that capture these strain gradients, either with higher-order tetrahedral, or multiple hexahedral elements through the thickness.

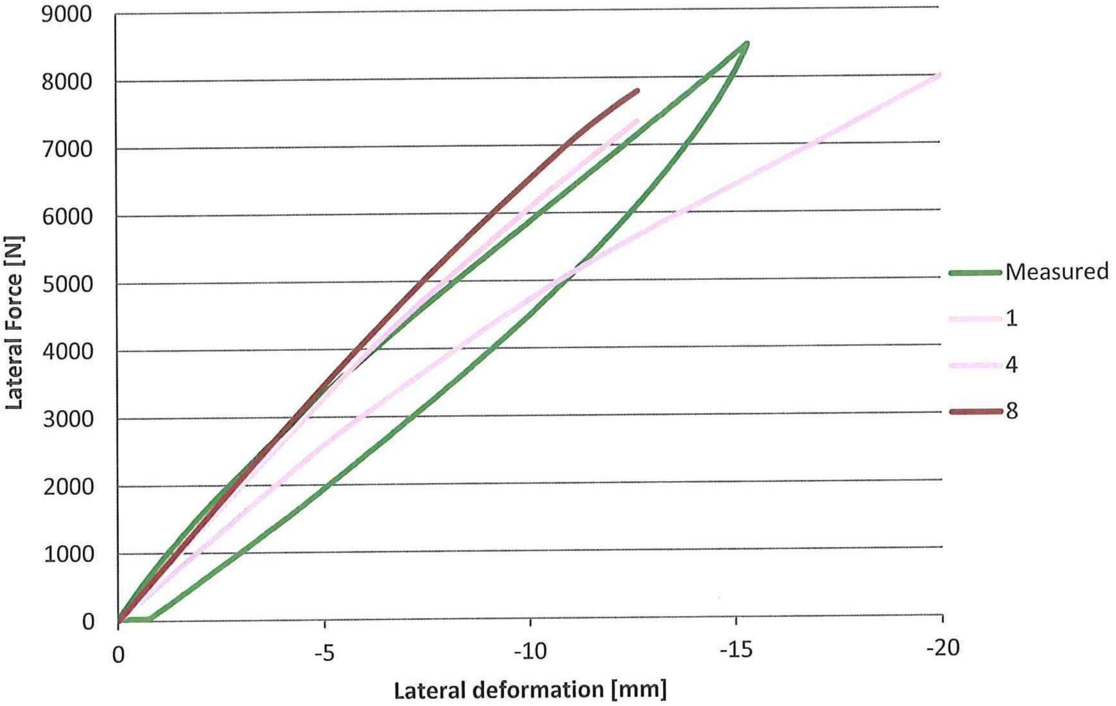

FIGURE 4.21: PRESSURIZED LATERAL DEFORMATION VS. LATERAL REACTION FORCE

Although it is interesting to be able to predict the stiffness responses of expansion joints, it is not an important design driver for expansion joint manufacturers. Therefore an accuracy of 30% over the specified deformation range is sufficient. The most important design drivers are the burst pressure and durability of expansion joints. Therefore, Table 4.4 shows a comparison between the measured and predicted restricted burst pressures. As the linear tetrahedral models were the only models able to give a converged solution at high pressures, only their results can be compared.

TABLE 4.4: STATIC BURST PRESSURES

Burst pressure [bar]	
Design	48
Measured	47
Abaqus	58,7
Aniform	57,2

As can be seen both simulations overestimate the burst pressure by approximately 20%. This discrepancy is caused by viscoelastic behaviour of both the rubber and fibres which is not accounted for in the simulation. Tests at Taniq at extreme load rates have shown burst pressures of over 70 [bar], whereas slowly loaded prototypes with exactly the same design showed burst pressures near the design burst pressure of 48 [bar]. By changing the load rate the burst pressure can thus be increased by 40%. Without the material efficiency factor of 0,8 the numerical models have an accuracy of lower than 5% with respect to the burst pressure at extreme load rates. This indicates that for an accurate burst pressure prediction, viscoelastic material behaviour and realistic load rates have to be included in the simulations.

4.8 CONVERGENCE PROBLEMS

As mentioned in Section 4.7 some of the models were not able to give a converged solution. The non-linear solution method requires the loads or deformations to be applied in multiple increments. In each increment iterations have to be made to achieve nodal equilibrium throughout the whole model, including the effects of the deformed geometry and non-linear material behaviour. However, if the iterative process does not give a converged solution the simulation becomes unstable. In that case the increment size will be decreased to find a stable solution but this is not able to surpass inherent numerical, structural or material instabilities.

The hyperelastic and incompressible behaviour of rubber is prone to such numerical and material instabilities, causing difficulties with convergence. In this Section causes for numerical and structural instabilities are discussed, whereas material instabilities will be discussed in Section 5.3.

The main numerical instability of incompressible rubber is volumetric locking. As the material is incompressible, the hydrostatic pressure becomes extremely sensitive to deformations if the rubber material is highly constrained. E.g., as the constrained rubber is limited in its movement and it is unable to compress, a small change in deformation can lead to a very large change in forces. Therefore unrestricted rubber models, such as balloons, are easy to analyse whereas highly constrained rubber structures, such as cord-reinforced rubbers, are not.

To prevent or limit numerical instabilities Abaqus gives recommendations for the types of elements to be used. Quadratic elements are recommended if strain gradients and element distortions remain small. For large deformations linear elements are recommended as they remain stable under large element distortions. Furthermore the use of hexahedral elements is recommended as they do not have the inherent volumetric locking that linear tetrahedral elements possess. [21]

Next to the numerical instabilities, structural instabilities can occur. Important structural instabilities are buckling or collapse. Due to the flexible nature of the cord-reinforced rubber, buckling can occur at low compressive load levels. In the case of buckling a negative stiffness occurs requiring the structure to release strain energy to maintain equilibrium.

One approach to model such behaviour is by using dynamic solution methods that do not require static equilibrium in each increment. However, these solution methods increase the computational cost significantly in comparison with a standard non-linear static analysis. Another approach is to absorb small amounts of strain energy caused by local buckling using viscous damping throughout the model to stabilize the analysis. An intermediate approach is to perform a quasi-static analysis in which the inertia effects of the material absorb the strain energy released in local buckling modes.

An interesting alternative for these methods is the use of the so called "modified Riks method". Whereas a normal (Newton-Raphson) non-linear static analysis applies a given load and determines the displacement for that specific load, the Riks method treats the load magnitude as an unknown variable as well. The quantity used to measure the progress of the analysis is the arc length along the static equilibrium path. For a given arc-length along this path, both the load and displacement are determined. This method is able to provide solutions, regardless of whether the structural response is stable or unstable. [23]

The difference between the Newton-Raphson and Riks non-linear solution methods is illustrated in Figure 4.22.

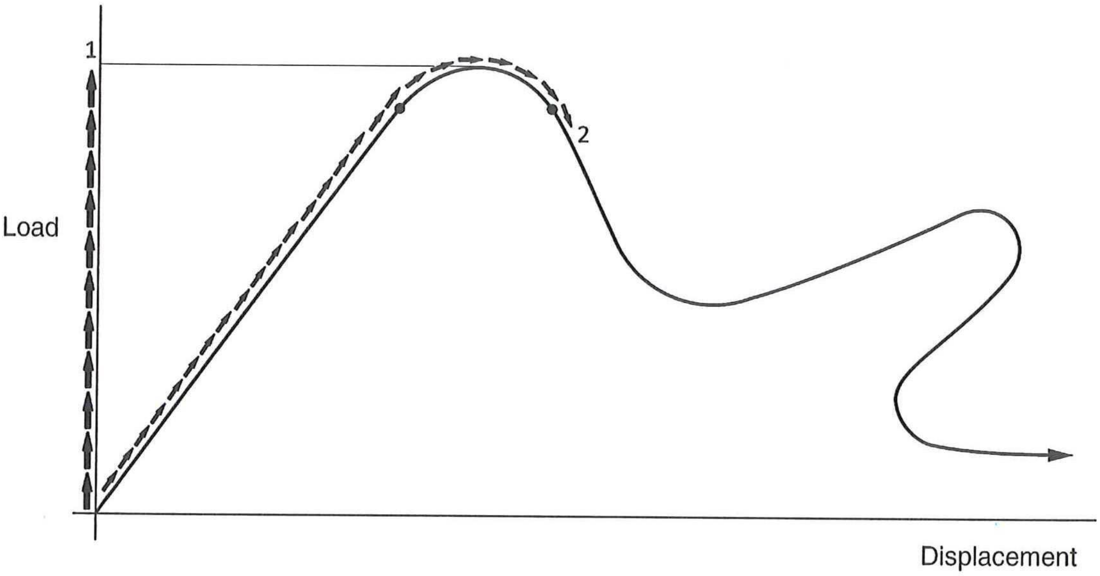

FIGURE 4.22: NON-LINEAR ANALYSIS METHODS
1 = NEWTON-RAPHSON, 2 = RIKS METHOD

4.9 MESH TRADE-OFF

In the previous Sections the importance of mesh alignment to prevent intra-ply shear locking has been demonstrated. This limits the fibre elements to aligned triangle surface or truss elements. The rubber can be modelled as tetrahedral elements aligned with the fibre triangle elements, or as unaligned hexahedral elements that are connected to the fibre layers using embedded constraints.

The most important requirements for the meshes are their convergence and robustness. The convergence of higher-order elements did not show any improvement with respect to first-order elements. The updated-Lagrangian solution method used in AniForm, did show improved convergence in comparison to similar Abaqus models. However, the unaligned hexahedral element shows similar convergence and is less prone to volumetric locking. Therefore this mesh type is chosen for future simulation as it is the most robust model and shows satisfactory convergence.

It should be noted that this mesh approach has proven to be sensitive to local buckling during lateral deformations. Therefore a linear tetrahedral model could be used for fibre force simulations of lateral load cases, as this mesh approach is less sensitive to local buckling and shows satisfactory convergence of the fibre forces.

5 RUBBER MODELLING

Expansion joints consist of two constituent materials, being the fibres and the rubber matrix. The fibres are easily modelled using linear elasticity. The rubber on the other hand has hyperelastic and incompressible behaviour. Therefore the modelling of rubber is typically done using continuum mechanics based material models.

Abaqus offers a wide variety of hyperelastic material models for the rubber ranging from the basic single-parameter Neo-Hookean model to advanced high-order Ogden models. Rubber suppliers typically provide only a single Neo-Hookean material parameter. This most basic model is not capable to describe the behaviour of rubber at high strain levels (>100%) and complex strain states. Therefore this Chapter makes a comparison between the use of different rubber material models during the modelling of expansion joints. By fitting different material models to material test data, the advantages of using calibrated material properties and complex material models will be investigated.

To be able to determine the parameters required for the different material models, the types of tests and their results will be discussed in Section 5.1. Next, Section 5.2 discusses the different material models and the method of fitting their parameters to the test data. As some hyperelastic material models can become unstable above certain strain levels, this will be investigated in Section 5.3. The effect of these calibrated material models on the results of the expansion joint simulations is investigated in Section 5.4. At last, Section 5.5 concludes whether the use of calibrated complex material models is worthwhile.

5.1 RUBBER TESTING

As this work has an application to high-performance expansion joints, the same rubber compounds are tested as used in these expansion joints. These are Chloroprene Rubber (CR) and Styrene-Butadiene Rubber (SBR). Next to these two types of rubber, the most common type of rubber, Natural Rubber (NR), is tested as well to see whether this material behaves differently.

The most commonly performed experiments to characterize the tensile hyperelastic material behaviour are uniaxial tension, equibiaxial tension and planar tension. Uniaxial tension describes a stretch in just a single direction, equibiaxial tension a constant stretch in a plane and planar tension a stretch in a single direction where the contraction in the width direction is restricted. These deformation modes are shown in Figure 5.1.

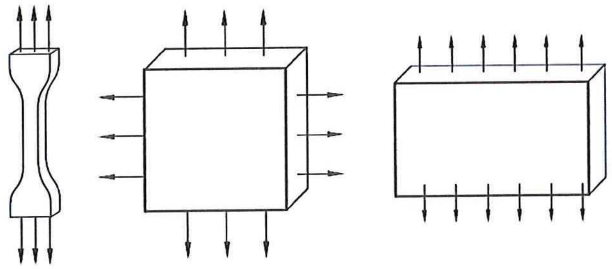

FIGURE 5.1: TENSILE DEFORMATION MODES[24]
LEFT: UNIAXIAL TENSION, MIDDLE: EQUIBIAXIAL TENSION, RIGHT: PLANAR TENSION

For an incompressible material model, the nominal stress-strain response is developed using derivatives of the strain energy function with respect to the strain invariants. The deformation gradient in terms of principal stretch directions is given by Equation 5.1 where the principal stretches λ_i are the ratios of current length with respect to the original length in the principal directions.

$$\boldsymbol{F} = \begin{vmatrix} \lambda_1 & 0 & 0 \\ 0 & \lambda_2 & 0 \\ 0 & 0 & \lambda_3 \end{vmatrix} \tag{5.1}$$

Assuming incompressibility requires the volume to stay constant and thus imposes the relation between the principal stretches shown in Equation 5.2.

$$\lambda_1 \lambda_2 \lambda_3 = 1 \tag{5.2}$$

This incompressibility results in the stretch states for the different types of tests listed in Table 5.1.

TABLE 5.1: STRETCH STATE AT DIFFERENT TENSILE DEFORMATION MODES [24]

Deformation Mode	**Stretch state**		
Uniaxial	$\lambda_1 = \lambda_U$	$\lambda_2 = \lambda_3 = \lambda_U{}^{-0,5}$	
Equibiaxial	$\lambda_1 = \lambda_2 = \lambda_B$		$\lambda_3 = \lambda_B{}^{-2}$
Planar	$\lambda_1 = \lambda_S$	$\lambda_2 = 1$	$\lambda_3 = \lambda_S{}^{-1}$

To fully describe the behaviour of a rubber material it is desirable to perform all three of these tests. The equibiaxial and planar tension experiments require specialized equipment that is not available. However, due to the incompressibility of the rubber, each tensile test has an equivalent compressive test that results in the same deformation mode. The equivalent to equibiaxial tension is uniaxial compression, which can be performed with standard equipment.

The same deformation mode between these experiments is achieved by a superposition of a tensile hydrostatic stress. For fully incompressible materials this superposition results in different stresses but does not change the deformation, as illustrated in Figure 5.2.

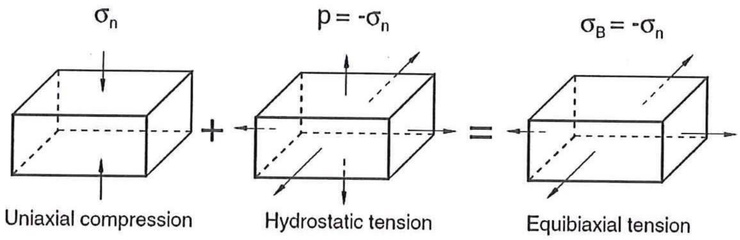

FIGURE 5.2: EQUIVALENT DEFORMATION MODE THROUGH SUPERPOSITION OF HYDROSTATIC STRESS [24]

The experiments that have been performed to determine the behaviour of the three types of rubber are thus a uniaxial tension experiment and a uniaxial compressive experiment. The tensile experiments have been performed according to the ASTM D412a standard and the compressive experiments according to the ASTM D575 standard. For both experiments ten specimens for each type of rubber have been moulded by an external rubber supplier.

The averaged uniaxial stress-strain responses for the three types of rubber are shown in Figure 5.3. This Figure confirms that the SBR and CR compounds have a similar uniaxial tensile response as indicated by the Neo-Hookean material parameters given by the supplier. The tested NR compound behaves a little more flexible. It should however be noted that the stiffness of a rubber can be altered significantly by adjusting the mixture and that NR is not by definition less stiff than SBR or CR.

FIGURE 5.3: UNIAXIAL TEST RESULTS

To ensure a deformation mode similar to biaxial tension during the compressive experiment, one adjustment has been made from the ASTM D575 standard. The ASTM standard prescribes the use of sandpaper to prevent slipping of the specimen. As this sandpaper would restrict the lateral expansion of the specimens, it would prevent an equibiaxial deformation mode. Therefore this sandpaper has been replaced by lubricant to minimize friction and maximize the equibiaxially deformed region within the specimen. Figure 5.4 shows the undeformed and deformed state of the specimens during compression. The nearly vertical sides of the specimen in the deformed state indicate that there is a nearly homogeneous equibiaxial deformation mode.

FIGURE 5.4: BIAXIAL TENSILE STRAIN STATE DURING UNIAXIAL COMPRESSION

Figure 5.5 shows the averaged equivalent biaxial stress-strain response of the types of rubber. It is interesting to note that in this deformation mode the SBR acts much stiffer than the CR. This indicates that a similar response for one deformation mode does not imply a similar behaviour for another deformation mode.

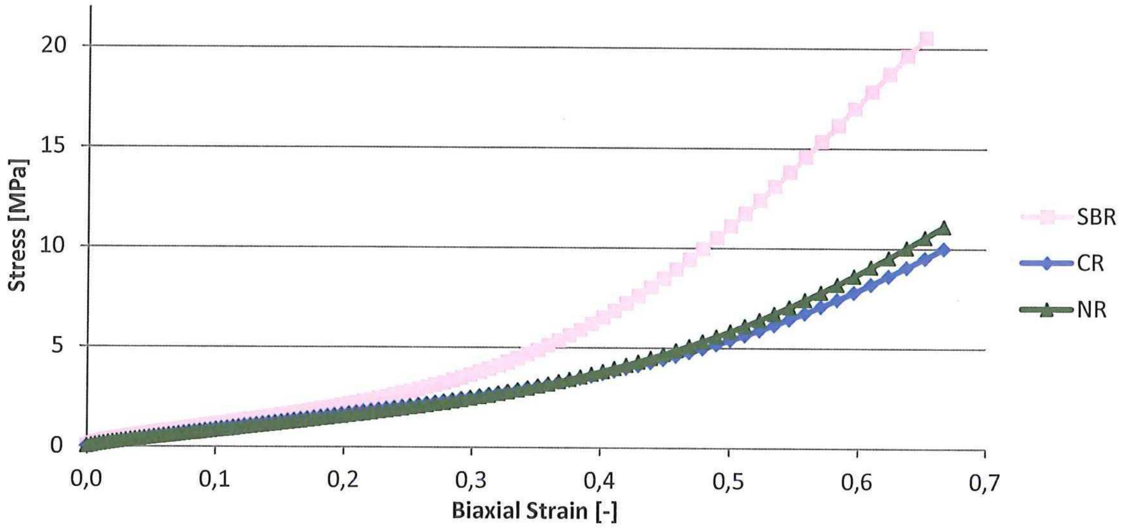

FIGURE 5.5: BIAXIAL TEST RESULTS

It should be noted that all rubbers behave fully elastic throughout the strain ranges shown in Figure 5.3 and Figure 5.5 and that this strain range is representative for the strains experienced in expansion joints.

5.2 MODEL FITTING

Hyperelastic material models are described by strain energy potentials. Therefore a relation between the nominal stress and strain according to the strain energy potential is required before material model parameters can be determined. The strain energy potentials describe the strain energy by means of deviatoric strain invariants. In the case of an incompressible material there are two strain invariants that are described by their principal stretches. These are shown in Equation 5.3. [25]

$$\begin{aligned} \bar{I_1} &= {\lambda_1}^2 + {\lambda_2}^2 + {\lambda_3}^2 \\ \bar{I_2} &= {\lambda_1}^{-2} + {\lambda_2}^{-2} + {\lambda_3}^{-2} \end{aligned} \tag{5.3}$$

The relation between the strain energy potential and nominal stresses and strains are determined using the principal of virtual work. The virtual work for uniaxial and equibiaxial deformation modes are given in Equation 5.4, where δU is the virtual work and T is the nominal stress.

$$\begin{aligned} \delta U &= T_U \delta \lambda_U \\ \delta U &= 2 T_B \delta \lambda_B \end{aligned} \tag{5.4}$$

Rewriting this equation to separate the nominal stresses gives Equation 5.5.

$$\begin{aligned} T_U &= \frac{\delta U}{\delta \lambda_U} = \frac{\delta U}{\delta \bar{I_1}} \frac{\delta \bar{I_1}}{\delta \lambda_U} + \frac{\delta U}{\delta \bar{I_2}} \frac{\delta \bar{I_2}}{\delta \lambda_U} \\ T_B &= \frac{\delta U}{\delta \lambda_B} = \frac{\delta U}{\delta \bar{I_1}} \frac{\delta \bar{I_1}}{\delta \lambda_B} + \frac{\delta U}{\delta \bar{I_2}} \frac{\delta \bar{I_2}}{\delta \lambda_B} \end{aligned} \tag{5.5}$$

Combining Equation 5.1 with Equation 5.5 and inserting the stretches of the uniaxial and equibiaxial deformation modes given in Table 5.1 results in the nominal stress formulation as given in Equation 5.6.

$$T_U = 2\left(1 - {\lambda_U}^{-3}\right)\left(\lambda_U \frac{\delta U}{\delta \bar{I}_1} + \frac{\delta U}{\delta \bar{I}_2}\right)$$
$$T_B = 2\left(\lambda_B - {\lambda_B}^{-5}\right)\left(\frac{\delta U}{\delta \bar{I}_1} + {\lambda_B}^2 \frac{\delta U}{\delta \bar{I}_2}\right) \qquad 5.6$$

Now the nominal stress-strain relationship for both experiments is known with respect to the strain energy potential. Material models can be curve fitted to the test data. This is done with Abaqus which uses a least square method to determine the material model parameters.

A wide variety of material models will be curve fitted to investigate their abilities to accurately describe the rubber behaviour. Each material model is best fitted to a certain type of test. The simple models are only able to describe uniaxial deformation accurately and are therefore best curve fitted to uniaxial tension data only. If these models would be fitted towards equibiaxial data too, they would show an overly stiff result. [21] The characteristics and strain energy potentials of the different material models can be found in Appendix B.1.

If detailed uniaxial tensile data is available, the Marlow material is a good choice as it exactly describes the uniaxial data and shows a reasonable accurate response in equibiaxial and planar tension.

A 3th-order Ogden model is recommended if detailed test data is available from multiple deformation modes. If a product is modelled that experiences significant equibiaxial or planar shear deformation and only uniaxial tension data is available, the equibiaxial and planar tension response can be estimated as well to allow the use of a 3th-order Ogden model. For most rubber materials the planar and equibiaxial stresses are respectively 20 and 40% higher than the uniaxial stresses at the same strain levels in a strain range up to 100%. [21]

In Table 5.2 an overview of the material models investigated are given, together with the data towards which they are fitted.

TABLE 5.2: EVALUATED MATERIAL MODELS AND FITTING DATA

Material Model	Abbreviation	Fitted to
Neo-Hookean	NHg	Parameters given by manufacturer
Neo-Hookean	NHt	Coarse uniaxial test data
Arruda-Boyce	AB	
Mooney-Rivlin	MR	
van der Waals	vdW	
Yeoh	Y	
Marlow	M	Detailed uniaxial test data
3th order Ogden	Oa	Detailed uniaxial test data and approximated biaxial and planar shear results
3th order Ogden	Ot	Detailed uniaxial and biaxial test data

The curve fitted parameters for all material models for SBR are shown in Table 5.3. The C and μ material properties are bulk moduli in [Pa], λ_m is the polymer locking stretch [-] and α is either the van der Waals polymer chain interaction factor [-] (van der Waals model) or the power of the principal stretches [-] (Ogden model). It is interesting to note that the Neo-Hookean parameter as given by the supplier is only 3% off with respect to a curve-fitted Neo-Hookean model. The material model parameters for CR and NR can be found in Appendix B.2.

TABLE 5.3: MATERIAL MODEL PARAMETERS FOR SBR

Material Model	Parameters					
Neo-Hookean Given	$C_{10} = 6{,}10\ 10^5$					
Neo-Hookean Measured	$C_{10} = 5{,}91\ 10^5$					
Arruda-Boyce	$\mu = 1{,}16\ 10^6$		$\mu_0 = 1{,}18\ 10^6$		$\lambda_m = 6{,}32$	
Mooney-Rivlin	$C_{10} = 6{,}66\ 10^5$			$C_{01} = -1{,}31\ 10^5$		
van der Waals	$\mu = 1{,}12\ 10^6$		$\lambda_m = 5{,}34$		$\alpha = 3{,}60$	
Yeoh	$C_{10} = 6{,}41\ 10^5$		$C_{20} = -5{,}87\ 10^4$		$C_{30} = 1{,}02\ 10^4$	
Marlow	*test data*					
Ogden, N=3 approximation	$\mu_1 = 1{,}21\ 10^6$	$\alpha_1 = 1{,}18$	$\mu_2 = 1{,}86\ 10^4$	$\alpha_2 = 6{,}91$	$\mu_3 = 6{,}15\ 10^3$	$\alpha_3 = -3{,}32$
Ogden, N=3 full tests	$\mu_1 = 1{,}84\ 10^6$	$\alpha_1 = -1{,}27$	$\mu_2 = 9{,}48\ 10^2$	$\alpha_2 = 10{,}1$	$\mu_3 = 1{,}46\ 10^5$	$\alpha_3 = -6{,}51$

Figure 5.6 shows the measured uniaxial stress-stretch response and that of the different curve fitted models for SBR. As can be seen almost all models match the actual tensile behaviour quite well. The most deviating model is the Ogden model fitted to all test data. This is due to the fact that this model is not only fitted to the uniaxial response but to the biaxial response as well. Furthermore it can be noted that the Mooney-Rivlin model is less stiff in compression. Since there is little compression of the rubber in expansion joints, it is expected that this will not influence the results of the FEA simulation.

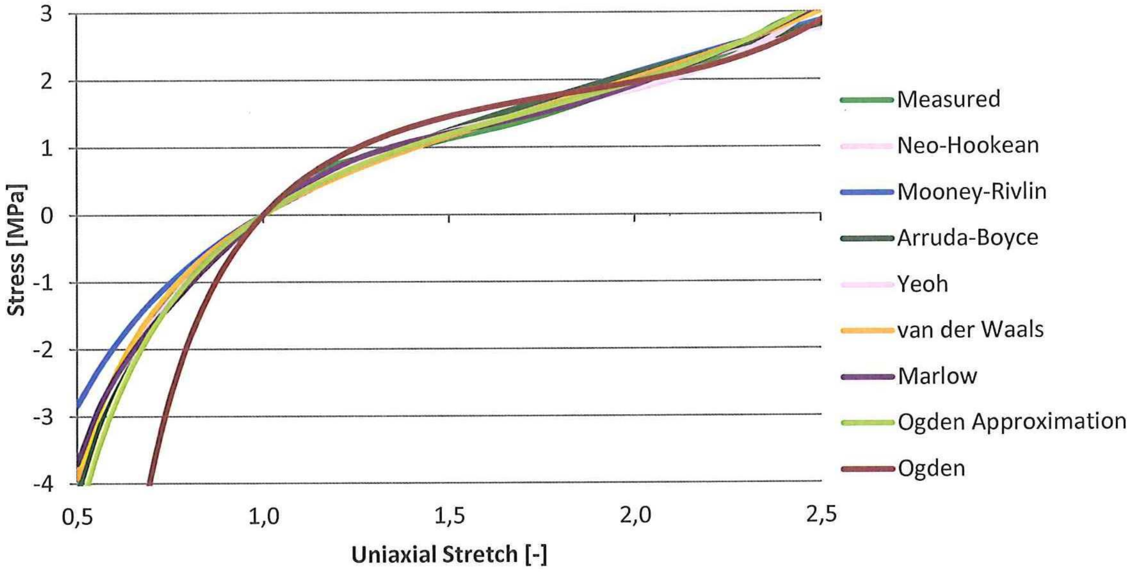

FIGURE 5.6: UNIAXIAL STRESS-STRETCH RESPONSE SBR

The equibiaxial stress-stretch responses of SBR are shown in Figure 5.7. In this deformation mode the difference between the different material models are more pronounced than in the uniaxial deformation mode. In this case only the 3th-order Ogden model is able to describe the measurements well as this is the only one fitted to this data. Furthermore this Figure shows the benefits of the Yeoh and van der Waals models, as they are able to describe the typical S-shape of the stress-stretch curve. It is interesting to note that the Ogden model based on the approximated biaxial test data is not able to show a significant improvement with respect to the models based on uniaxial data only. This indicates that the approximation is not valid in this case.

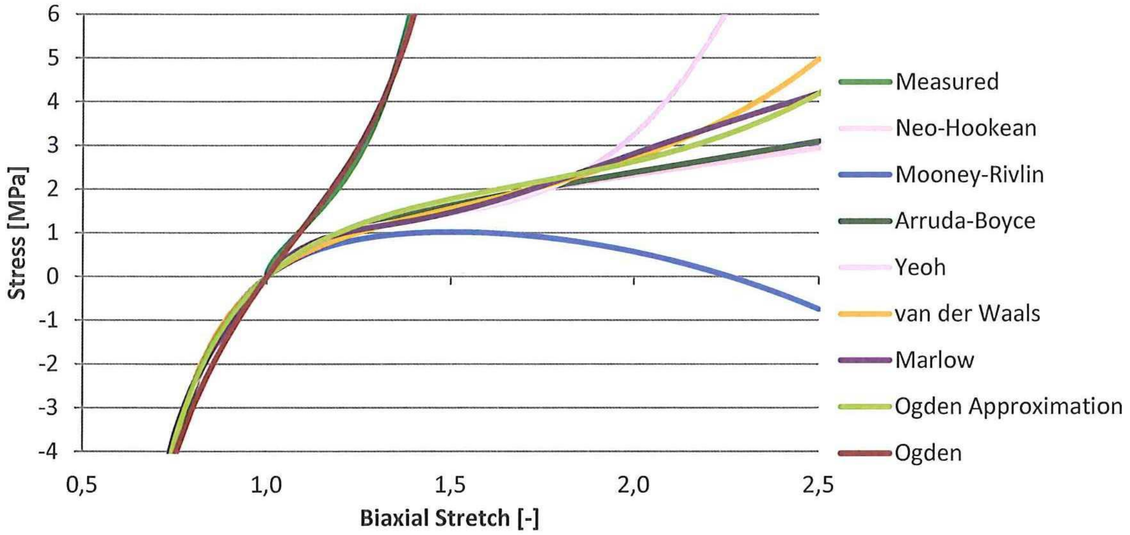

FIGURE 5.7: EQUIBIAXIAL STRESS-STRECHT RESPONSE SBR

Figure 5.8 shows the planar shear response of the different material models for SBR. As there is no test data available for this deformation mode it cannot be determined which model performs better. Typically it can be expected that the planar shear response will be somewhere in between the uniaxial and equibiaxial response. In that case the Ogden model based on all available test data would be most accurate but this cannot be verified without actual test data.

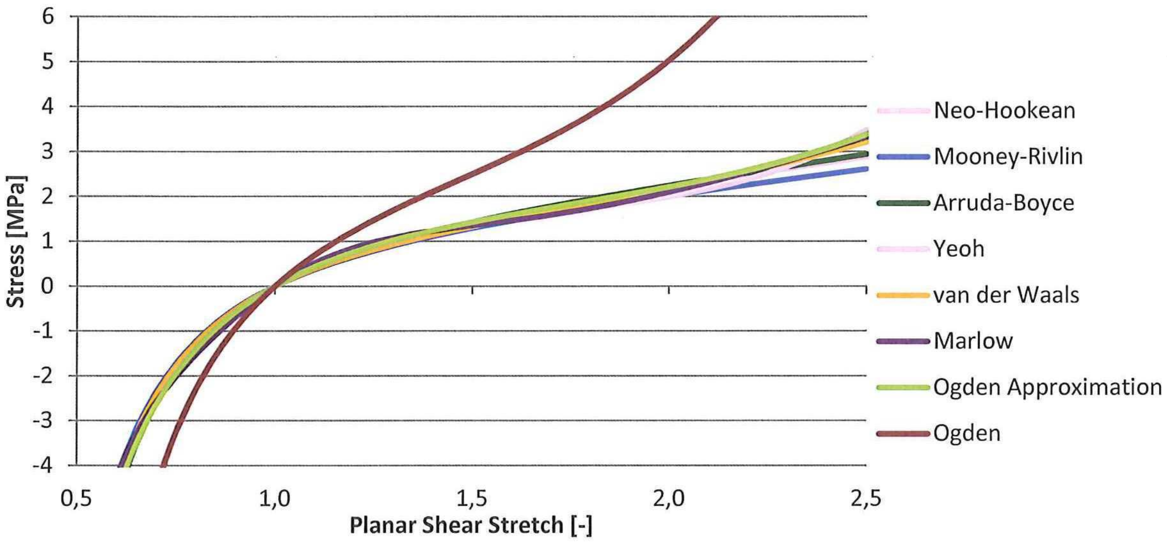

FIGURE 5.8: PLANAR STRESS-STRETCH RESPONSE SBR

In the previous Figures the results for SBR rubber has been shown. CR and NR show the same trend where all models describe uniaxial deformation well while the Ogden model fitted to all data is the only model able to accurately describe the other deformation modes. The stress-stretch responses for these materials can be found in Appendix B.3.

When the Neo-Hookean material properties as given by the supplier are compared with the actual measured data it can be concluded that this data is only sufficient to describe the uniaxial deformation mode. If a product has to be simulated that experiences equibiaxial and/or planar deformation modes this single material property will not be sufficient.

5.3 STABILITY

Next to the numerical (locking) and structural (buckling) instabilities discussed in Section 4.8, hyperelastic strain energy potentials can become unstable too. This is the case when external loading causes non-negative work within the material (e.g. a negative stress-strain gradient). As the least-square curve fitting procedure within Abaqus is not constrained to create unconditionally stable material models, their stability range has to be checked. In Abaqus the stability range for the three main deformation modes is checked by default in a stretch range from 0,1 to 10. [21]

Only two material models show instabilities, their unstable stretch ranges for the three deformation modes are shown in Table 5.4. As can be seen, the Mooney-Rivlin material shows the smallest stable stretch range. This corresponds with the equibiaxial stress-stretch response shown in Figure 5.7. It should be noted that as long as the stretch levels during the analysis are within the stable stretch range, an unstable material model will not cause issues. The maximum uniaxial stretch within an expansion joint during its most extreme deformation is typically not higher than 2,1. Therefore it is expected that none of the unstable material models will cause problems during the analysis. The unstable material models for CR and NR can be found in Appendix B.4.

TABLE 5.4: UNSTABLE SBR MATERIAL MODELS

Material Model	Stability Range Uniaxial	Stability Range Planar Shear	Stability Range Biaxial
Mooney-Rivlin	$0,36 \leq \lambda \leq 2,26$ [-]	$0,47 \leq \lambda \leq 2,15$ [-]	$0,67 \leq \lambda \leq 1,66$ [-]
van der Waals	$0,07 \leq \lambda \leq 5,31$ [-]	$0,19 \leq \lambda \leq 5,25$ [-]	$0,43 \leq \lambda \leq 3,78$ [-]

5.4 EFFECTS ON FINITE ELEMENT ANALYSIS

The previous Sections have investigated the response and stability of different materials in the case of a pure rubber. Although significant differences have been discovered in biaxial deformation modes, it is unknown whether this is a dominant deformation mode within expansion joints. Furthermore the main load carrying material in cord-reinforced rubbers is the fibre, limiting the effect of the rubber on the total product performance. This Section investigates the effect of the use of different material models on the total product performance.

As Figure 4.12 has shown that the only model showing converged rubber strains is the linear hexahedral elements in combination with embedded triangle elements, this model is used to compare the different material models. To prevent structural instabilities, a single-layered expansion joint is modelled, as this product has a converged solution throughout the full deformation range. To investigate the material model behaviour both axial (± 30 [mm]) and lateral (20 [mm]) deformations are applied at working pressure. The load cases can be seen in Figure 5.9.

It should be noted that in addition to Chapter 4, contact constraints are taken into account. These contact constraints represent the metallic closing flanges that are attached during testing. Apart from a more realistic simulation, these contact constraints eliminate local buckling in the cylindrical parts of the expansion joints in compressive load cases, resulting in a more robust analysis.

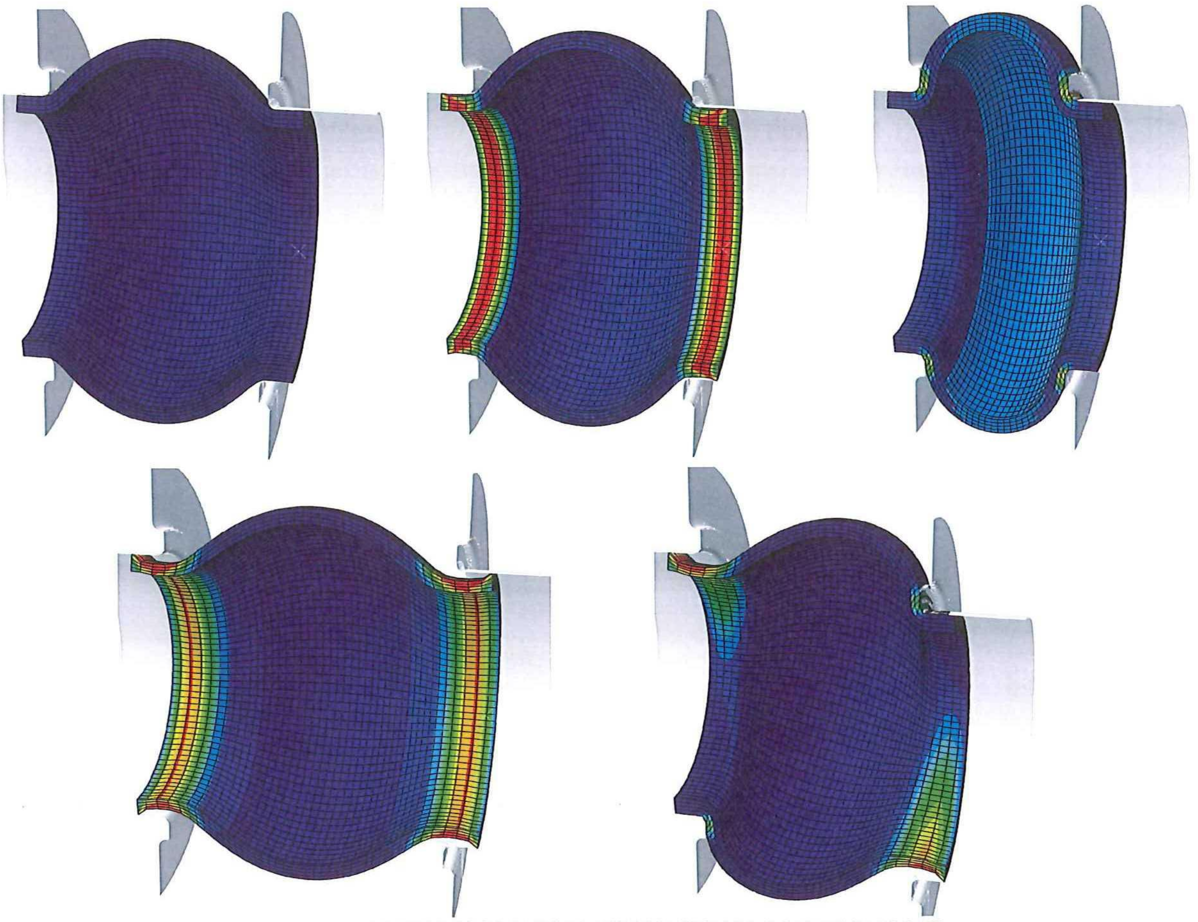

FIGURE 5.9: MAXIMUM PRINCIPAL RUBBER STRAIN CONTOUR PLOTS
TOP LEFT: UNLOADED, TOP-MIDDLE: PRESSURIZED, TOP-RIGHT: AXIAL COMPRESSION
BOTTOM LEFT: AXIAL ELONGATION, BOTTOM RIGHT: LATERAL DEFORMATION

The parameters that are compared are the axial and lateral reaction forces, the maximum fibre forces and the maximum principal rubber strain. The results for the material models calibrated using only uniaxial data are shown in Table 5.5. As can be seen the difference between the given Neo-Hookean parameter and the calibrated Neo-Hookean parameter is negligible. Furthermore the differences between all the models are rather small, except for the Arruda-Boyce model. The Arruda-Boyce model shows significant deviations from all the other results. This is unexpected as the stress-stretch response shown in Section 5.2 is similar to the other models. It is thus assumed that this is due to a numerical error within Abaqus when using the Arruda-Boyce model.

Table 5.5 also shows the standard deviation among the different material models calibrated to uniaxial tension data (except for the Arruda-Boyce model). This indicates that the differences between these models are negligible, except from the maximum principal rubber strain during axial compression. This is either due to the difference in uniaxial compressive behaviour of the Mooney-Rivlin model (Figure 5.6) and/or due to the difference in biaxial tensile behaviour of the Mooney-Rivlin, Yeoh and Marlow models (Figure 5.7). As the axial compressive load case is generally not a critical load case, and the standard deviation between the different material models is rather small, these differences will not affect the use of the numerical analysis methods.

TABLE 5.5: REACTION FORCES, FIBRE FORCES AND RUBBER STRAINS FOR UNIAXIAL CALIBRATED MATERIAL MODELS

Load Case	Parameter		Material Models								
			NHg	NH	MR	vdW	Y	M	Oa	AB	σ [%]
Restricted Pressurized	Axial Reaction Force	[N]	3632	3631	3659	3587	3718	3743	3647	3925	**1,4**
	Maximum Fibre Force	[N]	143	143,3	143,7	143	143,3	142,7	143,5	133,3	**0,2**
	Maximum Principal Rubber Strain	[-]	0,239	0,240	0,239	0,246	0,231	0,2281	0,238	0,295	**2,3**
Axial Elongation	Axial Reaction Force	[N]	12925	12923	12988	12770	12799	12753	12846	12089	**0,6**
	Maximum Fibre Force	[N]	160,6	160,3	161,3	161,1	159,9	159,6	160,5	147,4	**0,4**
	Maximum Principal Rubber Strain	[-]	0,818	0,819	0,806	0,828	0,833	0,870	0,821	0,785	**2,3**
Axial Compression	Axial Reaction Force	[N]	-8190	-8195	-8279	-8161	-8243	-7827	-8212	-5874	**1,7**
	Maximum Fibre Force	[N]	121,3	120,0	119,5	118,1	121,1	119,6	118,5	112,5	**0,9**
	Maximum Principal Rubber Strain	[-]	0,585	0,577	0,524	0,592	0,557	0,635	0,571	0,210	**5,4**
Lateral Deformation	Axial Reaction Force	[N]	1724	1722	1724	1692	1685	1683	1701	2539	**1,0**
	Lateral Reaction Force	[N]	6057	6059	6111	5973	5986	5967	6022	4606	**0,8**
	Maximum Fibre Force	[N]	243,3	243,9	244,5	242,5	242,2	241,6	243,3	215,9	**0,4**
	Maximum Principal Rubber Strain	[-]	1,076	1,076	1,059	1,082	1,090	1,115	1,075	0,916	**1,5**

The fully calibrated 3th order Ogden model is compared with the given Neo-Hookean material model in Table 5.6. Again, the maximum fibre forces only show a negligible difference. However, a clear deviation in the reaction forces can be seen. With the fully calibrated model, the expansion joint behaves up to 10% stiffer than the given material model. An even larger difference can be seen in the maximum principal rubber strains. This indicates that the biaxial and planar tension deformation modes are present in the expansion joint and have a significant influence on the reaction forces and rubber strains. It should however be noted that the given material model overestimates the maximum rubber strains in each deformation mode. Therefore, this simple model provides a conservative approximation.

TABLE 5.6: COMPARISON BETWEEN THE GIVEN AND FULLY CALIBRATED MATERIAL MODEL

Load Case	Parameter		NHg	Ot	Deviation [%]
Restricted Pressurized	Axial Reaction Force	[N]	3632	3930	8,2
	Maximum Fibre Force	[N]	143	142,2	-0,6
	Maximum Principal Rubber Strain	[-]	0,239	0,198	-17,2
Axial Elongation	Axial Reaction Force	[N]	12925	13909	7,6
	Maximum Fibre Force	[N]	160,6	162,3	1,1
	Maximum Principal Rubber Strain	[-]	0,818	0,739	-9,6
Axial Compression	Axial Reaction Force	[N]	-8190	-8530	4,2
	Maximum Fibre Force	[N]	121,3	119,1	-1,8
	Maximum Principal Rubber Strain	[-]	0,585	0,486	-16.9
Lateral Deformation	Axial Reaction Force	[N]	1724	1908	10,7
	Lateral Reaction Force	[N]	6057	6659	9,9
	Maximum Fibre Force	[N]	243,3	249,6	2,6
	Maximum Principal Rubber Strain	[-]	1,076	0,990	-8,0

The axial stiffness response of the expansion joint using different material models is shown in Figure 5.10. This Figure confirms that the difference between the uniaxial calibrated material models is insignificant and that the fully calibrated Ogden model behaves slightly stiffer than the other models. Furthermore it shows the erroneous results of the Arruda-Boyce model, as it should predict a smooth load-displacement curve throughout the entire deformation range.

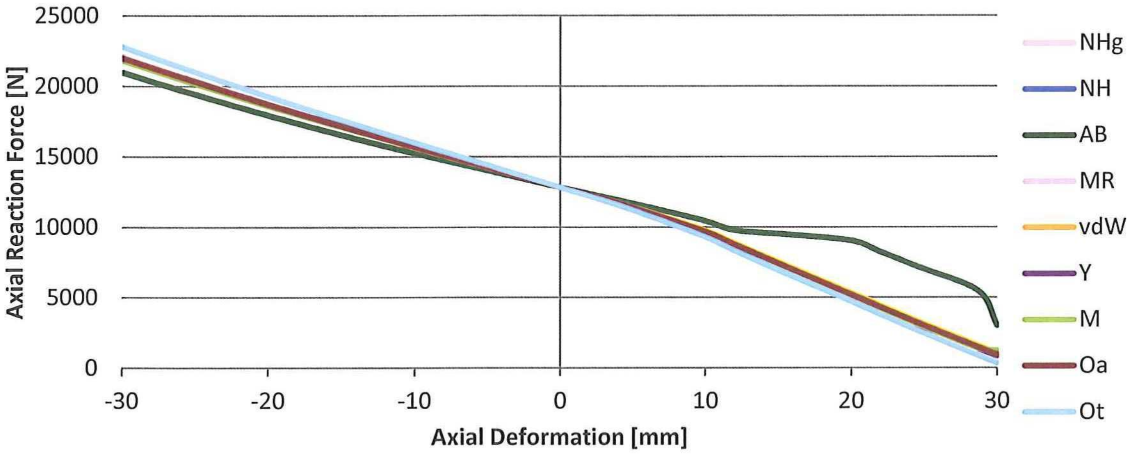

FIGURE 5.10: AXIAL LOAD DISPLACEMENT OF DIFFERENT MATERIAL MODELS

The lateral stiffness response is shown in Figure 5.11. Again the difference between the uniaxial calibrated models is insignificant. The difference between the fully calibrated Ogden model and the others is more significant during lateral deformation than during axial deformation. This indicates that during this load case, biaxial and planar tension modes are more influential than during axial load cases. The Arruda-Boyce model shows a large deviation with respect to the other models. The cause of this deviation remains unclear, as the stress-stretch response of this model is similar to that of the other models

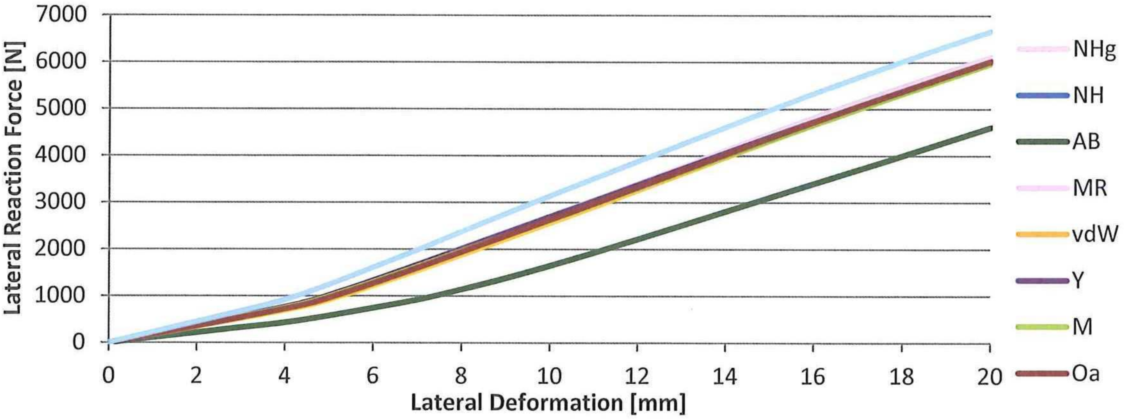

FIGURE 5.11: LATERAL LOAD DISPLACEMENT OF DIFFERENT MATERIAL MODELS

5.5 CONCLUSION

The previous Sections have shown that the material parameter given by the material supplier is not able to accurately model the rubber response in biaxial or planar tensile deformation modes. Different material models that are calibrated using only tensile data show little improvement in these deformation modes. The effect of these deformation modes on the analysis results is however limited. The maximum fibre forces are nearly independent of the material model used. Therefore the most basic material model is able to accurately predict fibre failure modes.

A larger difference is visible in the reaction forces and rubber strains. However, the stiffness response of an expansion joint is not an important design driver. Furthermore the most basic material model overestimates the rubber strains, making it a conservative approximation for expansion joints. It can thus be argued whether the improvements that can be achieved by using a fully calibrated advanced material models, are worth the additional testing efforts.

It should be noted that the influence of biaxial and planar tensile deformation modes might be more significant when modelling multi-layered expansion joints with interlaminar strains. As the fully calibrated material model parameters are known anyway, these will be used in the remainder of this research. The exact material model parameters of these models are given in Table 5.7.

TABLE 5.7: PARAMETERS OF THE 3TH ORDER OGDEN MATERIAL MODEL

Material	Parameters					
SBR	$\mu_1 = 1{,}84\ 10^6$	$\alpha_1 = -1{,}27$	$\mu_2 = 9{,}48\ 10^2$	$\alpha_2 = 10{,}1$	$\mu_3 = 1{,}46\ 10^5$	$\alpha_3 = -6{,}51$
CR	$\mu_1 = 1{,}61\ 10^6$	$\alpha_1 = -0{,}25$	$\mu_2 = 5{,}28\ 10^3$	$\alpha_2 = 8{,}16$	$\mu_3 = 9{,}32\ 10^4$	$\alpha_3 = -5{,}84$
NR	$\mu_1 = 1{,}54\ 10^6$	$\alpha_1 = -0{,}88$	$\mu_2 = 1{,}07\ 10^3$	$\alpha_2 = 9{,}98$	$\mu_3 = 5{,}35\ 10^4$	$\alpha_3 = -6{,}57$

6 FAILURE MODES

So far the numerical analysis method and the influence of the material parameters on this analysis have been investigated. To relate the results of these numerical analyses to actual product performance, the dominant failure modes of the products have to be determined. In this Chapter these failure modes are investigated and related to fracture mechanics of both the fibres and the rubber. Fracture mechanics will be used to establish the critical parameters that determine the products performance.

There are both static and dynamic failure mechanism that are dependent on the material used and the load cases. Whereas a static analysis (fibre burst) is relatively simple, an accurate quantitative dynamic analysis of cord-reinforced rubber is very complex. It would require viscoelastic effects (Mullins Effect, Elastic Hysteresis) as well as detailed load rates to be incorporated in the analysis. As these parameters are difficult to obtain without lengthy testing programs, it is chosen to relate the dynamic failure mechanisms on the basis of qualitative reasoning. By determining force and strain amplitudes of various designs, their dynamic performance can be compared without requiring an exact quantitative prediction.

In consultation with the experience available at Taniq, the performance of expansion joints and cord-reinforced rubbers in general, has been traced back to four predominant failure mechanisms. Section 6.1 discusses the failure mechanism of rubber cracking, which is the only failure mode related to rubber. The most important static and dynamic failure mode is burst failure caused by fibre breakage and will be discussed in Section 6.2. An important dynamic failure mechanism for Aramid fibres in lateral load cases is fibre compression. This failure mechanism will be investigated in Section 6.3. At last fibre abrasion due to fibre shearing within the product will be discussed in Section 6.4.

6.1 RUBBER CRACKING

Rubber cracking is the only rubber related failure mode. Rubber cracking is typically a dynamic failure mode that is highly compound specific. The critical region for rubber cracking in expansion joints is the connection of the cylindrical part with the flanges. A typical rubber crack at this location can be seen in Figure 6.1. These rubber cracks initiate at the top of the expansion joint during cyclic lateral deformation of the joint and grow along the full circumference. Although these cracks of the outer rubber are not critical for the performance of the expansion joint, they are inadmissible for the customers.

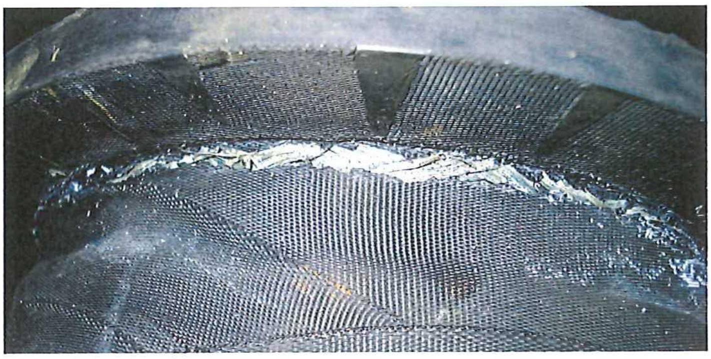

FIGURE 6.1: RUBBER TEARING FAILURE[26]

Cord-reinforced rubber failure typically initiates at the rubber-fibre interface, either perpendicular to the fibre direction or along the rubber-fibre interface. Numerical simulation of the fatigue life of cord-reinforced rubbers is based on J-Integrals determining strain-energy release rates and crack growth on a micromechanical level. [27]

Dynamic failure behaviour of cord-reinforced rubbers is dependent on a large variety of parameters, the most important are;

- Internal geometry
- Rubber Compound
- Degree of Anisotropy (Stiffness Ratio between the Fibre and Rubber)
- Rubber-Fibre Bonding
- 3D-strain states
- Load rates

The exact internal geometry of a product is required to determine the initial flaw geometry initiating the rubber crack. This initial flaw geometry is the determining factor in the nucleation of cracks in rubber. As the majority of the fatigue life of rubber consists of this crack initiation phase, knowledge about the exact internal geometry is vital for an accurate fatigue life prediction.[28] The exact geometry of the fibres within the rubber is however unknown due to fibre build-up and fibres flowing through the rubber during vulcanization. The internal geometry of an expansion joint is shown in Figure 6.2. As can be seen the exact distribution of the fibres throughout the expansion joint varies and is thus not sufficient for a detailed simulation of the fatigue life.

FIGURE 6.2: FIBRE DISTRIBUTION NEAR THE FLANGES OF AN EXPANSION JOINT

Whereas a detailed fatigue life analysis is impossible with the limited knowledge of the exact fibre geometry, the global models developed in this research are suitable for the prediction of critical regions within the expansion joints for rubber cracking. [27] Uniaxial tests of cord-reinforced rubber have shown reasonable agreement with Strain-Life curves and have shown an infinite fatigue life below a certain strain threshold. [29] Extending these uniaxial tests to complex 3D-load cases has indicated that the plane of maximum normal strain gives a good prediction of the direction of crack growth. [30] The global models developed in this research can thus be used to indicate the critical regions within the products. Furthermore the strains among different designs can be compared, as a lower peak strain will result in a better fatigue life.

6.2 FIBRE BURST FAILURE

The most important failure mode of expansion joints is fibre burst failure. During static testing this is the dominant failure mode. A single fractured fibre instigates a chain reaction of adjacent fibres breaking and the rubber tearing, causing complete failure of the expansion joint. A typical fibre burst failure is shown in Figure 6.3. It clearly shows one main crack perpendicular to one of the two fibre directions and smaller bifurcations in the other fibre direction.

FIGURE 6.3: FIBRE BURST FAILURE

Static burst pressures are typically close to their designed failure pressures, regardless of the fibre type. The fibre fracture surface is however different for each material. Tensile failure of highly oriented chain-extended polymer fibres such as Aramid is caused by axial split breaks, showing frayed fibre ends. Melt-spun synthetic fibres such as Nylon or Polyester show ductile failure and blunt fibre ends. [14] These can be seen in Figure 6.4.

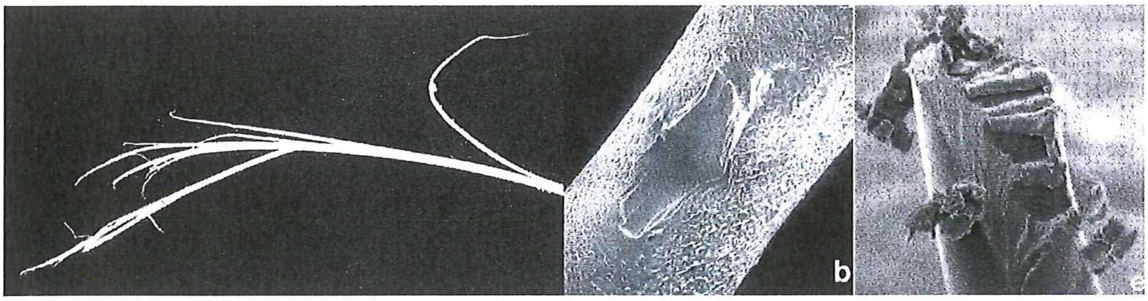

FIGURE 6.4: FIBRE FRACTURES [31]
LEFT: AXIAL SPLIT BREAKS IN ARAMID FIBRE
MIDDLE: DUCTILE CRACK PROPAGATION IN NYLON FIBRE, RIGHT: DUCTILE FRACTURE OF NYLON FIBRE

The cause for this different behaviour is due to the internal molecular structure of the different fibres. The highly-oriented aramid fibres have strong covalent bonds in their axial direction, but rely on weaker van der Waals forces and hydrogen bonds for their transverse properties. Therefore they are more prone to show cracks in the axial directions (axial split breaks). These axial split breaks propagate through the length of a fibre up to the end of the molecular chains where they are able to propagate in the transverse direction, as illustrated in Figure 6.5. If such a crack propagates through the width, the fibre fails and shows its characteristic frayed fracture surface.

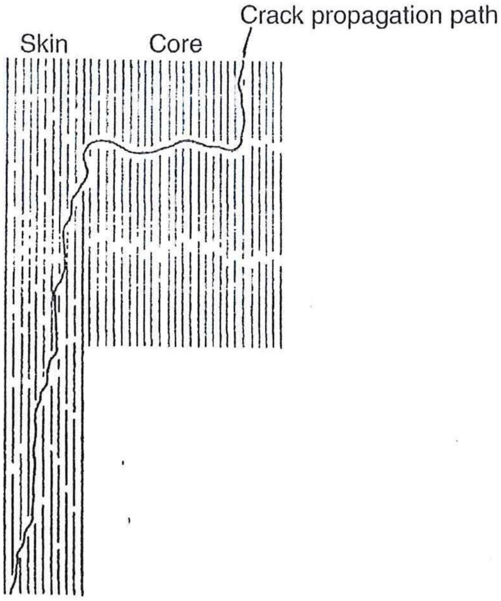

FIGURE 6.5: CRACK PROPAGATION PATH IN ARAMID FIBRES [31]

Melt-spun synthetic fibres such as Nylon are less oriented than Aramid fibres. Therefore they show less anisotropy and have better properties in their transverse direction. Due to their molecular structure these fibres allow some ductility as well, which shows in their fibre ends.

The tensile fatigue properties of Aramid fibres are excellent, as they show little degradation at load levels close to its tensile breaking strength. Nylon on the other hand experiences some weakening due to cyclic tensile loading. This is due to inherent defects that initiate crack growth in its transverse direction. The extent of fatigue degradation of Nylon fibres depends on the exact fibre type. [31]

In general the maximum fibre force during different load cases is the most important parameter for the performance of an expansion joint. The maximum fibre force determines the burst-pressure which is the most important performance measure of cord-reinforced rubber products.

6.3 FIBRE COMPRESSION

As most load cases for cord-reinforced rubbers cause pure tensile fibre loading, the previous Section was concerned with static and dynamic tension-tension failure of the fibres. Lateral loading on the other hand can cause fibre compression in the bellow of expansion joints. Depending on the fibre type, compressive fibre stresses can be detrimental to the overall product performance.

Due to the poor properties in the transverse direction of Aramid fibres, they offer little resistance to micromechanical buckling when loaded in compression. This micromechanical buckling is also known as kink band formation and is shown in Figure 6.6. These kink bands initiate axial split breaks at very low compressive strain levels. Furthermore the axial split break growth during repetitive compressive loading is much quicker than during pure tensile loading. Therefore the tension-compression fatigue performance of Aramid is poor, especially in comparison with their excellent tension-tension fatigue properties. As Nylon fibres have good properties in their transverse direction, they are less prone to kink band formation and show excellent tension-compression fatigue properties.

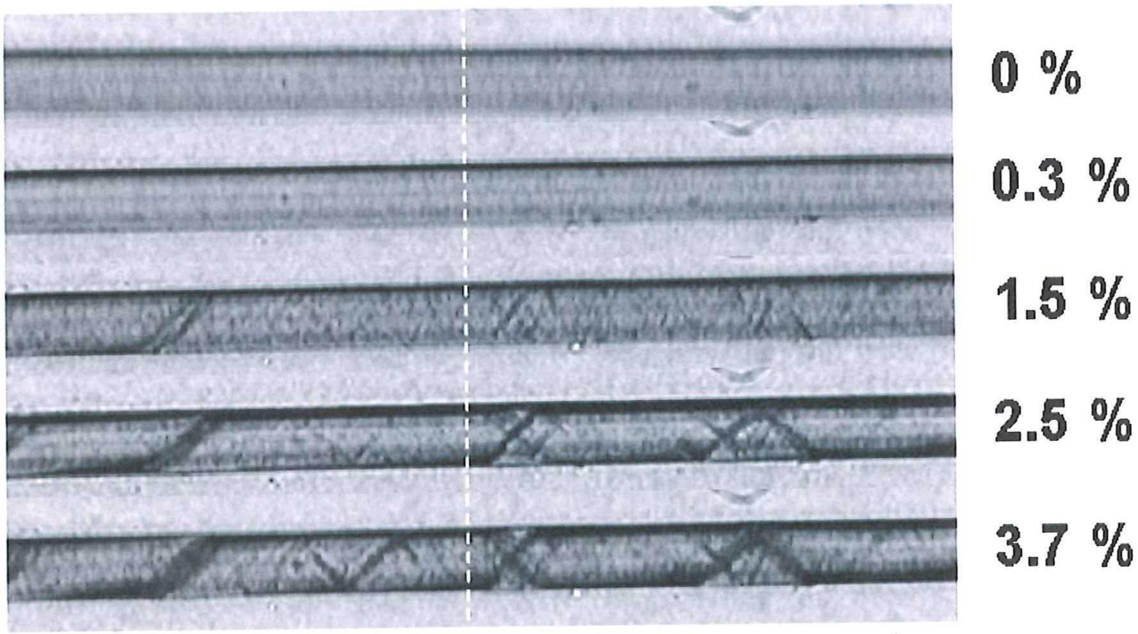

FIGURE 6.6: FORMATION OF KINK BANDS DURING PURE AXIAL COMPRESSION IN ARAMID FIBRES [32]

Cyclic lateral deformation is one of the most stringent requirements for high-performance expansion joints. Dynamic lateral testing has shown extreme degradation of the burst-pressure. The lateral deformation cycles cause large stress amplitudes that can extend into compressive fibre forces. To investigate the fibre load distribution during lateral deformation, an Aramid design without local reinforcements has been simulated at working pressure (16 [bar]), test pressure (3 [bar]) and an intermediate pressure (10 [bar]). The minimum, maximum and average forces in the fibres at the centre of the bellow as a function of the lateral deformation are shown in Figure 6.7.

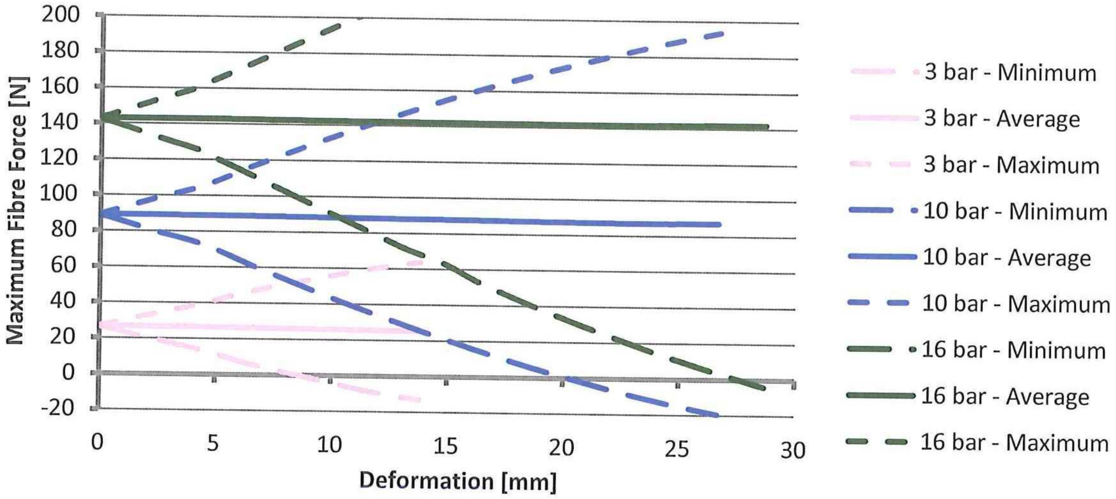

FIGURE 6.7: CENTRAL BELLOW FIBRE FORCES DURING LATERAL DEFORMATION, UNREINFORCED ARAMID

As can be seen the average fibre forces in the centre of the bellow remain approximately constant, regardless of the lateral deformation. The minimum fibre force shows a linear decrease with respect to the lateral deformation whereas the maximum fibre force shows a linear increase. This indicates that a significant part of the lateral deflection is absorbed by shear deformation of the bellow. The filament wound angle-ply fibre layers experiences compressive forces in one fibre direction and tensile forces in the other, in addition to the tensile fibres caused by the pressure.

Next to the shear deformation in the bellow, bending of the cylindrical parts of the expansion joint absorbs part of the lateral deformation as well. To investigate the effects of the bending stiffness of the cylindrical part on the bellow fibre force distribution, a design with local reinforcement on the cylindrical part is simulated. The results of this Nylon prototype are shown in Figure 6.8.

In comparison with the unreinforced prototype this design shows compressive fibre forces at lower levels of lateral deformation. The local reinforcement increases the bending stiffness of the cylindrical part. Therefore this section is less able to absorb the lateral deformation by bending, causing higher shear loads in the bellow.

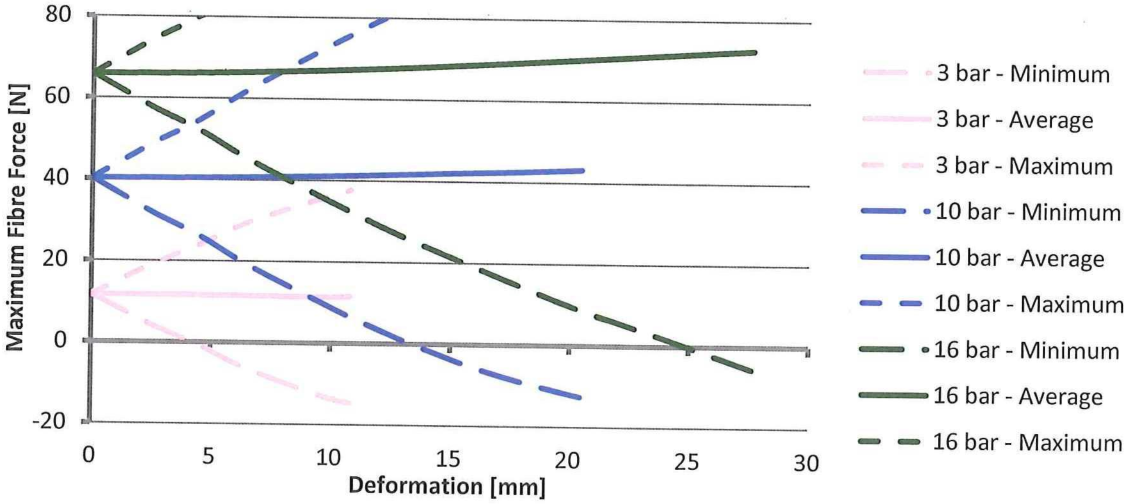

FIGURE 6.8: CENTRAL BELLOW FIBRE FORCES DURING LATERAL DEFORMATION, REINFORCED NYLON

The regions with compressive forces during lateral deformation in one direction are shown in Figure 6.9. Next to the compressive forces, the fibres in the cylindrical region experience compression as well. These compressive forces are less critical for the product performance as their maximum tensile forces during a lateral cycle remain rather low. The fibres on the middle of the bellow are critical as they experience the largest stress amplitude during a full lateral cycle. A lateral cycle goes up and down in both directions, causing the sides of the bellow to experience the minimum fibre force at one end and the maximum at the other. This has been confirmed during testing, as the location of failure during lateral fatigue testing has been consistently on the side of the bellow.

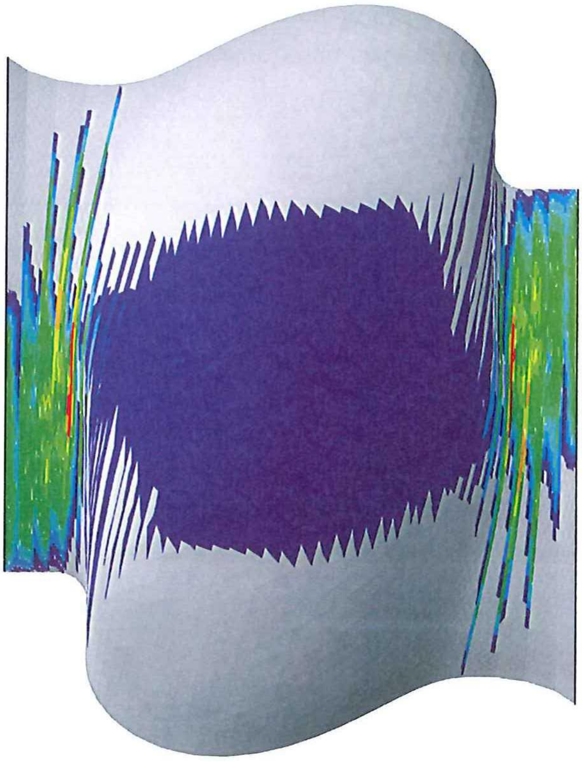

FIGURE 6.9: COMPRESSIVE REGIONS DURING LATERAL DEFORMATION AT 16 [BAR]

One of the difficulties when simulating lateral deformation is buckling of the bellow. The compressive fibre forces cause this structural instability that cannot be simulated using conventional solution methods. The linear decrease of the minimum fibre stresses during lateral deformation can however be used to predict the lateral deformation at which the forces become negative without actually modelling such a large unstable lateral deformation. To verify this assumption linear trend lines are determined for the minimum fibre forces as a function of the lateral deformation for the two different simulations at all pressures.

The slope and coefficient of determination of these trend lines are shown in Table 6.1. The linear approximation of the minimum fibre force response is valid, as the coefficients of determination are close to unity. The slopes at different pressures vary and are thus not interchangeable. Therefore if a prediction has to be made of the lateral deformation until compression at a given pressure level, the average force at that pressure level has to be determined and the slope of minimum fibre force at that pressure level up till a moderate lateral deformation. This slope can then be extrapolated to determine the lateral deformation where fibre compression initiates.

TABLE 6.1: LATERAL FIBRE FORCE EFFECT AND COEFFICIENT OF DETERMINATION

Design	Pressure [bar]	dFF/dz [N/mm]	R^2 [-]
Unreinforced Aramid	3	3,08	0,9991
	10	4,49	0,9977
	16	5,38	0,9981
Reinforced Nylon	3	2,76	0,9981
	10	3,02	0,9987
	16	2,66	0,9949

It should be noted that among the types of fibres used for expansion joints, only Aramid fibres experience deterioration due to compressive fibre forces. Therefore this failure mode is only critical for this fibre type.

6.4 FIBRE FRETTING

Another dynamic effect that influences the fatigue performance is fibre fretting. This is caused by abrasion of fibres running along each other. The dry winding used by Taniq causes the fibres to be in direct contact with each other without any protective resin layer in between. Furthermore the fibre shearing during the large deformations causes significant movement between the fibres in contact.

Both Nylon and Aramid fibres experience significant fibre fretting. Due to the brittle nature of Aramid it is more sensitive to abrasion. Figure 6.10 shows abrasion of an aramid fibre that has been in contact with a rotating metallic pin. The cyclic shearing of fibres repeatedly scrapes of some of the fibre material, gradually reducing the cross sectional area and its strength.

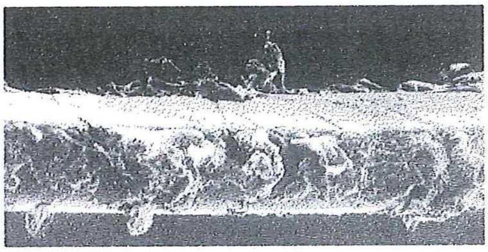

FIGURE 6.10: ABRASION OF AN ARAMID FIBRE [31]

As the through-thickness compressive stresses in cord-reinforced rubbers are low, this failure mode in itself is unlikely to cause failure of an entire expansion joint. However, it does add up to the other failure modes, contributing to a dynamic decrease in strength. Therefore the shear angle during deformation is an interesting parameter to keep track when comparing different designs.

7 PARAMETRIC STUDY

The purpose of the structural analysis methods investigated in the previous Chapters is to facilitate a more efficient design process of cord-reinforced rubber products. To validate the usability of the structural analysis method, a parametric study will be performed on an expansion joint. This parametric study will show the effect of different design parameters on the stress distribution and structural performance of the expansion joint. Furthermore these results can be used to determine an optimal expansion joint design.

For an efficient parametric study, Design of Experiments (DOE) is applied. Design of Experiments comprises of a set of statistical tools that enables statistically valid conclusion for a large design population with as little experiments as possible. In this Chapter this method is used to investigate the effects and interaction effects of multiple parameters with a limited number of numerical experiments.

To facilitate a parametric study it is important to determine all significant and modifiable design parameters. These are listed in Section 7.1, as well as their corresponding range of values. Section 7.2 discusses the actual design of the experiments and gives an overview of the experiments to be performed. The performance measures used to analyse the numerical experiments are related to the failure modes discussed in Chapter 6 and are given in Section 7.3. The results of the numerical experiments are shown in Section 7.4. These results are used to determine the significant design parameters for the different performance measures. Furthermore the effects of the different parameters on the stress and strain distribution will be discussed. In Section 7.5, DOE is used to determine an optimal expansion joint design that satisfies all manufacturing constraints. As DOE is unable to include the continuous non-linear effect of the length of the reinforcement layer, the optimal reinforcement length is determined separately in Section 7.6. This optimal design is validated by static and dynamic testing in Section 7.7. At last Section 7.8 gives some recommendations and design rules for future expansion joint developments.

7.1 PARAMETERS

An important part of a parametric study and a design of experiments is to determine which parameters are of importance and which of those can be influenced. In this parametric study an ID100 expansion joint is investigated (inner Ø = 100 [mm]). Such a small size is generally made using just a single main fibre layer, as this results in the shortest production times. Therefore the number of main fibre layers is not a design parameter as it would be for larger sizes. In consultation with Taniq the remaining significant design parameters have been determined. These are shown in Table 7.1.

TABLE 7.1: EXPANSION JOINT DESIGN PARAMETERS

Parameters	
Fibre Material	**Upper Reinforcement**
Bellow Shape	**Upper Reinforcement Length**
Bridging	**Lower Reinforcement**
Rubber Type	**Lower Reinforcement Length**
Reinforcement Angle	

The most important design parameter is the fibre material. Taniq has used a variety of fibre materials with different stiffness's and breaking strengths. Another important design parameter is the bellow shape. Optimal (isotensoid geodesic) winding is ensured when using a Corpo bellow as described in Section 3.3. However, some customers prefer other bellow shapes to increase the flexibility of the expansion joint. Where the bellow shape defines the winding angle on the bellow, the winding angle on the cylindrical region is controlled using fibre steering to satisfy the winding criteria for the flanges. As described in Section 3.2 the fibre angle in this cylindrical section can be adjusted using the bridging manufacturing method. Therefore the winding angles in the cylindrical regions are an important design parameter as well.

Next to the main fibre layer, local reinforcements are often applied to limit the elongation of the cylindrical regions and the corresponding high rubber strains. Either no reinforcement, reinforcement at the top or the bottom, or both reinforcement at the top and the bottom are used. Furthermore the length and fibre angle of both of these reinforcements can be varied. As proven in Section 6.3, these reinforcements have a significant influence and are therefore important design parameters.

The last design parameter that can be influenced is the type of rubber applied. This is usually stipulated by the customer for the desired level of chemical resistance on both the in- and outside of the product. However, the flexibility and dynamic performance of the rubbers can be significantly adjusted by using different compounds. This can be beneficial to increase the rubber tearing performance of an expansion joint.

Most of the design parameters are discrete. The only continuous variable parameters are the length of the upper and lower reinforcement layers. Therefore it is chosen to perform a conventional 2-level Design of Experiments. This requires a low and a high level for each parameter. These are listed in Table 7.2.

TABLE 7.2: DESIGN PARAMETER LEVELS

Parameter		Low Level	High Level
Fibre Material		Nylon	Aramid
Below Shape		Hyperbolic	Corpo
Bridging		No	Yes
Rubber Type		SBR	CR
Upper Reinforcement		No	Yes
Upper Reinforcement Length	**[mm]**	20	40
Lower Reinforcement		No	Yes
Lower Reinforcement Length	**[mm]**	25	50
Reinforcement Angle	**[°]**	0	45

The fibre materials that are investigated during this parametric study are Nylon and Aramid. These are the main fibre types used by Taniq. Aramid is a much stronger and stiffer fibre than Nylon requiring approximately half the amount of fibres to achieve the same burst pressure. The compressive performance of Aramid is however very poor, making it less suitable for lateral load cases. Both of the fibres used are treated with a rubber coating to improve rubber fibre bonding. The fibre supplier provides detailed test data for each batch of fibres, which are shown in Table 7.3. The numbers of fibres shown are the number of fibres required for a design burst pressure of 48 [bar] of an ID100 expansion joint.

TABLE 7.3: FIBRE PROPERTIES [33, 34]

Material	Young's Modulus [GPa]	Breaking Strength [N]	Poisson's Ratio [-]	Area [mm^2]	Number of Fibres
Nylon	4,34	314	0,39	0,401	488
Aramid	51,7	617	0,36	0,279	248

Figure 7.1 shows the profile of representative designs for both a Corpo and Hyperbolic bellow. The required height and length are typically given by the customer, limiting the design freedom of the bellow shapes. In general hyperbolic bellows are more flexible, but they do not allow isotensoid fibre paths.

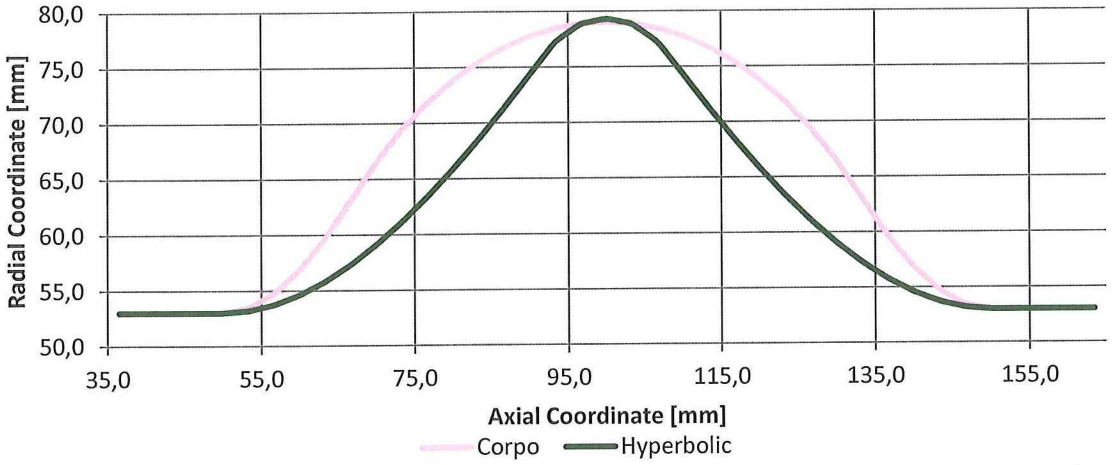

FIGURE 7.1: BELLOW SHAPES

The bridging and conventional winding paths corresponding with the given bellow shapes are given in Figure 7.2. For a conventional winding path the winding angle next to the flange has to be 86°, whereas the bridging manufacturing method allows for an angle of 78°. In the case that the fibre angle at the end of the bellow does not reach these angles, the minimum amount of friction is applied to reach the required winding angle next to the flange.

The local reinforcement material that is used is provided by the customer and can therefore not be adjusted. The local reinforcements are applied in the form of Nylon-Rubber prepregs, either unidirectional or angle-ply woven prepregs. These angle-ply prepregs are applied as ±45° reinforcements, whereas the unidirectional layers are applied as a single 0° layer. The properties of the prepregs are given in Table 7.4.

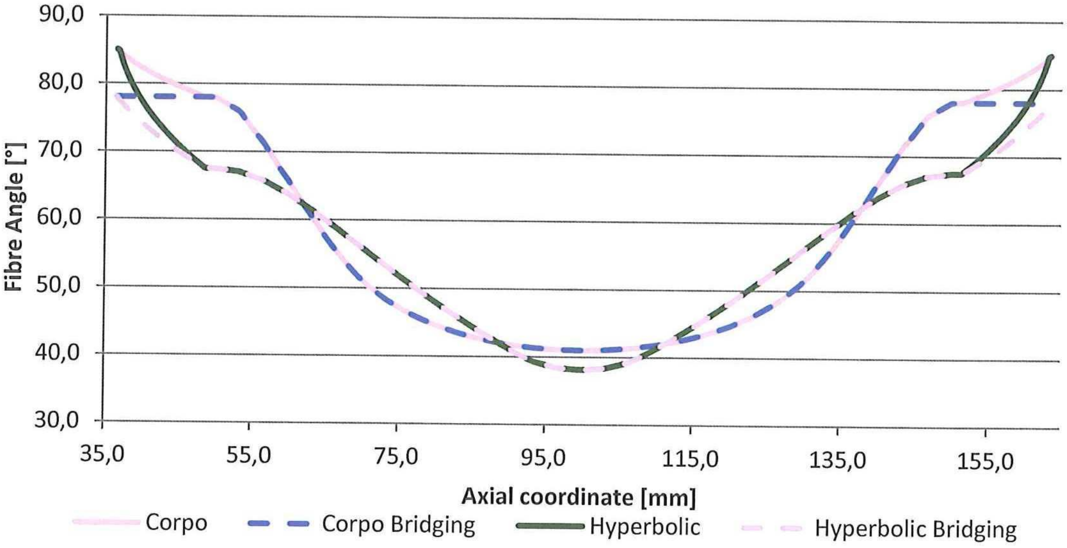

FIGURE 7.2: FIBRE ANGLES

Typically a full layer of upper and lower reinforcement is respectively 40 and 50 [mm] long along the profile path. To improve the lateral flexibility of the expansion joint, these layers can be shortened. For this parametric study it is chosen to take half of the full length as the low level. This allows expansion joints with both no, half and full upper and/or lower reinforcement to be included in the Design of Experiments.

TABLE 7.4: LOCAL REINFORCEMENT PROPERTIES [35]

Youngs Modulus [GPa]	Poisson's Ratio [-]	Area [mm^2]	Spacing [mm]
2,0	0,39	0,832	1,388

The last design parameter is the type of rubber. For chemical resistance CR and/or SBR are used for high performance expansion joints. For this parametric study it is chosen to investigate either fully CR or fully SBR expansion joints. Their calibrated properties and the respective material model used are given in Table 5.7. It should be noted that the stress-strain response of both rubbers in uniaxial tension is very similar, but they do show a different response in biaxial tension. This parametric study will show whether this difference has a significant effect on product performance.

7.2 DESIGN OF EXPERIMENTS

Now all the parameters and their corresponding levels are known, a Design of Experiments can be made. To determine all main and interaction effects, a full factorial design with a total of 272 experiments would be required. To limit this number of experiments, a fractional factorial design is used. This assumes that some interaction effects are not important, allowing the main effects and important 2nd order interaction effects to be studied with as little experiments as possible.[36]

For this parametric study it has been chosen to perform a 1/16th fractional factorial design. This limits the number of experiments to 32. This gives a resolution IV Design which indicates that no main effects are confounded with any other effects, but some two-factor interactions are confounded with each other. Confounding is the combining of the influence of certain effects on the measurement by which their effects cannot be estimated independently.

Commercial statistics software called Minitab is used to construct the Design of Experiments. When designing a fractional factorial design, this software allows the user to indicate the important two-factor interaction effects that should not be confounded. From there on the software constructs the design of experiments, indicating which designs have to be tested. An overview of the designs to be analysed for this parametric study is given in Table 7.5. The confounded interaction effects of this design of experiments are listed in Appendix C.1.

TABLE 7.5: EXPERIMENTAL OVERVIEW

#	Fibres	Bellow	Bridging	Rubber	Upper Reinforcement Length [mm]	Lower Reinforcement Length [mm]	Reinforcement Angle [°]
1	Nylon	Hyperbolic	Yes	SBR		40	±45
2	Aramid	Hyperbolic	Yes	SBR		20	0
3	Nylon	Corpo	Yes	SBR			
4	Aramid	Corpo	Yes	SBR			
5	Nylon	Hyperbolic	No	SBR			
6	Aramid	Hyperbolic	No	SBR			
7	Nylon	Corpo	No	SBR		20	±45
8	Aramid	Corpo	No	SBR		40	0
9	Nylon	Hyperbolic	Yes	CR			
10	Aramid	Hyperbolic	Yes	CR			
11	Nylon	Corpo	Yes	CR		40	0
12	Aramid	Corpo	Yes	CR		20	±45
13	Nylon	Hyperbolic	No	CR		20	0
14	Aramid	Hyperbolic	No	CR		40	±45
15	Nylon	Corpo	No	CR			
16	Aramid	Corpo	No	CR			
17	Nylon	Hyperbolic	Yes	SBR	25		0
18	Aramid	Hyperbolic	Yes	SBR	50		±45
19	Nylon	Corpo	Yes	SBR	25	40	±45
20	Aramid	Corpo	Yes	SBR	50	20	0
21	Nylon	Hyperbolic	No	SBR	50	20	±45
22	Aramid	Hyperbolic	No	SBR	25	40	0
23	Nylon	Corpo	No	SBR	50		0
24	Aramid	Corpo	No	SBR	25		±45
25	Nylon	Hyperbolic	Yes	CR	50	40	0
26	Aramid	Hyperbolic	Yes	CR	25	20	±45
27	Nylon	Corpo	Yes	CR	50		±45
28	Aramid	Corpo	Yes	CR	25		0
29	Nylon	Hyperbolic	No	CR	25		±45
30	Aramid	Hyperbolic	No	CR	50		0
31	Nylon	Corpo	No	CR	25	20	0
32	Aramid	Corpo	No	CR	50	40	±45

7.3 PERFORMANCE

To determine the effects of the parameters on product performance, performance measures have to be determined. The performance measures are related to the failure modes given in Chapter 6 and are listed in Table 7.6. It should be noted that al load cases are simulated at the working pressure of 16 [bar].

TABLE 7.6: EXPANSION JOINT PERFORMANCE MEASURES

Result	Model	Deformation
Maximum Rubber Strain	Embedded Model	30 [mm] elongation
Maximum Fibre Force	Embedded Model	restricted
		30 [mm] elongation
	Tetrahedral Model	5 [mm] lateral
Lateral Deformation Until Compressive Fibres	Tetrahedral Model	5 [mm] lateral
Maximum Fibre Shear Angle	Embedded Model	30 [mm] elongation

For the rubber performance the maximum principal rubber strain is evaluated in the elongated pressurized load case. This deformation mode is known to give one of the highest rubber strains throughout the specified deformation range of the expansion joint. The maximum fibre forces are measured for both the restricted, elongated and lateral deformation modes to give an indication of the static performance of the expansion joint throughout its deformation range. For a fair comparison between different fibre types, the fibre force relative to its breaking strength is measured.

As was indicated in Section 6.3, fibre compression is detrimental for lateral dynamic performance of Aramid expansion joints. Therefore a prediction is made of the lateral deformation at which the fibres on the bellow become compressive. This is done by linear extrapolation of the decrease in fibre forces on the middle of the bellow up to 5 [mm] of lateral deformation. As this relationship is nearly linear (as indicated in Table 6.1), this is a valid estimation.

To investigate the effect of fibre fretting, the maximum shear angle of the main fibre layer is measured. As fibre shearing is most extreme during axial elongation, it is only measured for this deformation mode.

It should be noted that wherever possible, a model with linear hexahedral elements for the rubber and embedded linear triangle fibre elements is used. For the lateral load case, the linear tetrahedral rubber elements aligned with the linear triangle fibre elements is more robust. This model has proven to deliver accurate and converged fibre stresses, and is therefore used to determine fibre forces during lateral deformation. To enable a fair comparison between all designs, a lateral deformation of just 5 [mm] is simulated, as this provides a converged solution for each design.

Table 7.7 shows the simulated results for all the designs. In this table the actual maximum fibre force is shown instead of the fibre force relative to the breaking strength, as this gives a better overview of the differences between the various load cases.

TABLE 7.7: EXPERIMENTAL RESULTS

Design	Max Rubber Strain [-]	Max Fibre Force [N]			Compressive Lateral	Fibre Shear [°]
	Elongated	Restricted	Elongated	Lateral	Deformation [mm]	Elongated
1	0,49	71	99	75	15,0	-14,3
2	0,56	147	244	167	7,1	-16,2
3	0,60	63	75	70	37,4	-9,5
4	0,68	139	214	142	27,4	-11,4
5	0,98	71	78	63	20,7	-12,2
6	0,85	148	179	136	11,9	-13,2
7	0,83	69	91	74	27,2	-9,6
8	0,34	152	323	170	10,7	-16,0
9	0,65	71	98	70	26,7	-11,4
10	0,59	149	187	141	12,1	-12,0
11	0,78	69	129	78	21,2	-14,3
12	0,70	148	280	157	15,3	-10,7
13	0,82	71	94	70	16,7	-12,8
14	0,44	159	198	171	6,3	-15,5
15	0,76	68	75	71	40,3	-9,7
16	0,88	139	183	138	34,1	-11,5
17	0,60	70	100	74	14,2	-13,7
18	0,44	167	210	192	5,2	-15,8
19	0,49	68	96	80	16,9	-12,3
20	0,43	153	314	208	6,0	-17,6
21	0,52	66	97	77	10,1	-15,8
22	0,65	225	353	200	13,7	-20,8
23	0,59	68	130	82	16,0	-15,9
24	0,37	140	223	177	9,8	-11,7
25	0,93	87	139	73	13,0	-19,9
26	0,44	146	209	184	6,0	-16,1
27	0,29	64	99	83	16,1	-11,8
28	0,45	150	282	182	9,0	-13,8
29	0,64	71	93	70	13,9	-12,5
30	0,53	209	345	184	5,1	-20,1
31	0,77	103	138	79	18,4	-11,0
32	0,81	138	298	197	6,8	-14,0

During the analysis of the results some interesting phenomena have been observed apart from the parametric effects that will be discussed in the following Section. First of all the location of the maximum rubber strain is dependent on the bellow shape. For the hyperbolic bellow this location is on the inside of the middle of the bellow as the hyperbolic shape flexes outwards, as can be seen in Figure 7.3. For the Corpo bellow the location of maximum strain is either at the end of the reinforcement or, if no reinforcement is present, at the flange boundary. These locations show stress concentrations that translate to high rubber strains.

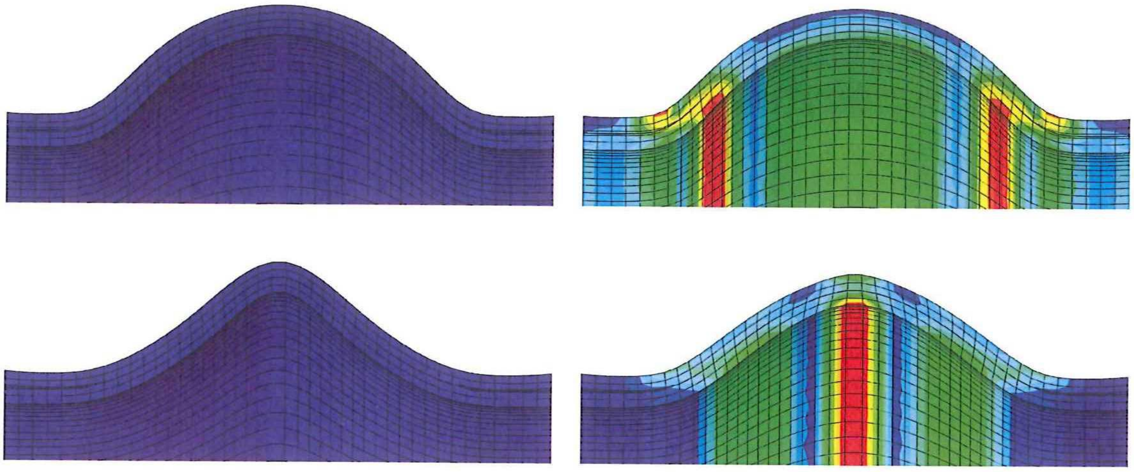

FIGURE 7.3: NOMINAL STRAIN CONTOUR PLOT ON ORIGINAL AND PRESSURIZED GEOMETRY
TOP: CORPO BELLOW, BOTTOM: HYPERBOLIC BELLOW

When looking at the fibre forces, the maximum fibre force for the hyperbolic bellow is approximately on a quarter of the bellow. This is due to the curvature caused by the outward flexing of the bellow when pressurized, resulting in non-optimal fibre directions at the given location on the bellow and thus higher fibre forces. In an unreinforced Corpo bellow the forces throughout the majority of the bellow are evenly distributed. However, when reinforcement layers are present these induce stress concentrations causing the maximum fibre force to be located at the end of the reinforcement.

Considering the deformation until fibre compression, Nylon performs significantly better than Aramid. This is due to the fact that the higher stiffness of the Aramid causes a higher bending stiffness of the cylindrical region, requiring the lateral deformation to be absorbed by shearing of the bellow. Therefore the poor performance of Aramid fibres in compression in combination with the low levels of deformation before compression occurs accumulates to a poor dynamic lateral performance of these expansion joints. Nylon performs much better, as it is better able to handle compression and only shows compression at high levels of lateral deformation.

With respect to fibre shearing, hyperbolic bellows show somewhat higher shear angles than Corpo bellows. This is again caused by the flexing of the bellow and the less optimal fibre angles. The position of maximum fibre shear is at the top of the bellow for both bellow types.

7.4 PARAMETER EFFECTS

To investigate the main and interaction effects, Pareto charts are made for each performance measure. A Pareto chart shows the sorted absolute values of the effects. Furthermore it indicates a reference line indicating the level above which an effect becomes significant. The Pareto charts are calculated using the same Minitab software that was used to create the Design of Experiments with a reference line indicating a 5% significance.

Figure 7.4 shows the Pareto chart for the rubber strain. As can be seen the most important main effects are the presence of upper reinforcement, bridging and fibre material. The most important sensible interaction effects are those of upper and lower reinforcement, and material and reinforcement angle.

Upper reinforcement, or any combination of upper and lower reinforcement, causes stress concentrations, explaining the significance of its effects on the rubber strain. The same holds for material type and reinforcement angle, as the stiffness of Aramid fibres matches well with the 0° Nylon reinforcement, whereas the lower stiffness of the Nylon fibres matches better with a ±45° Nylon reinforcement layer. Bridging on the other hand influences the axial elongation of the cylindrical section, limiting the rubber strains in this region. Furthermore the fibre material has a significant effect, as the stiffer Aramid fibres will result in smaller deformations throughout the whole expansion joint, limiting the average rubber strains.

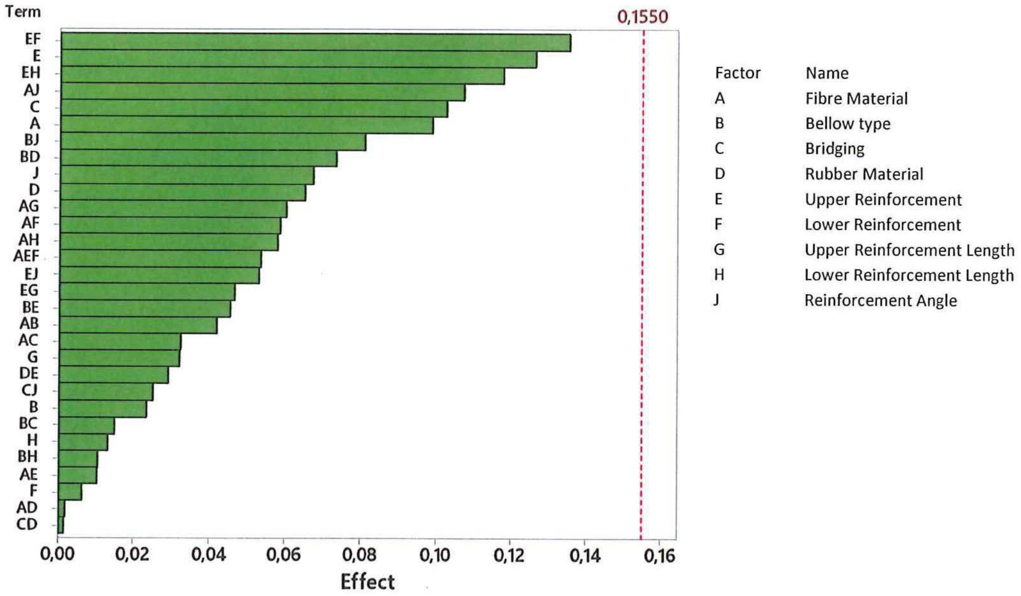

FIGURE 7.4: MAXIMUM RUBBER STRAIN PARETO CHART

The Pareto chart for the maximum fibre force during restricted pressurization is shown in Figure 7.5. The most important main effects are the fibre material, reinforcement angle, upper reinforcement and bellow shape. The most important interaction effects are the upper reinforcement and reinforcement angle, and bridging and reinforcement angle.

The effect of fibre material is caused by the fibre stiffness, as the Nylon fibres are more flexible such expansion joints expand more during restricted pressurization. Therefore the deformed internal surface on which the pressure is exerted becomes larger than is the case with Aramid fibres, causing a slight increase in relative fibre forces. The effect of the reinforcement angle, upper reinforcement and interaction of upper reinforcement and reinforcement angle on the maximum fibre forces is due to the stress concentrations that they cause. The effect of the bellow shape on the fibre forces was already indicated in the previous Section and is due to the non-optimal fibre angles (non-isotensoid) on the hyperbolic bellow.

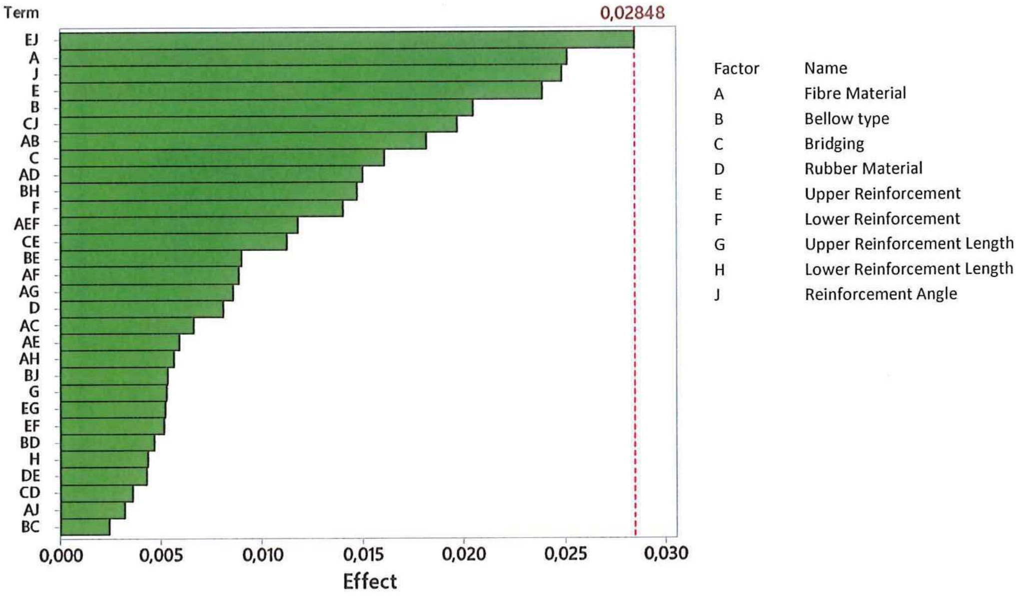

FIGURE 7.5: RESTRICTED MAXIMUM FIBRE FORCE PARETO CHART

Figure 7.6 shows the Pareto chart for the maximum fibre force during axial elongation. This performance measure is mainly influenced by the fibre material, upper and lower reinforcement and reinforcement angle. Furthermore the interaction of upper reinforcement and reinforcement angle has a significant effect.

Axial elongation has a bigger effect on Aramid fibres than it has on Nylon fibres. This is due to the high stiffness of the Aramid fibres, that causes a larger increase in relative fibre force at a given deformation than is the case for Nylon fibres. The main effects as well as the interaction effect of the reinforcements and their angle are clearly visible as well. These reinforcements show the biggest stress concentrations in the axial direction, causing a more significant effect than in the restricted load case.

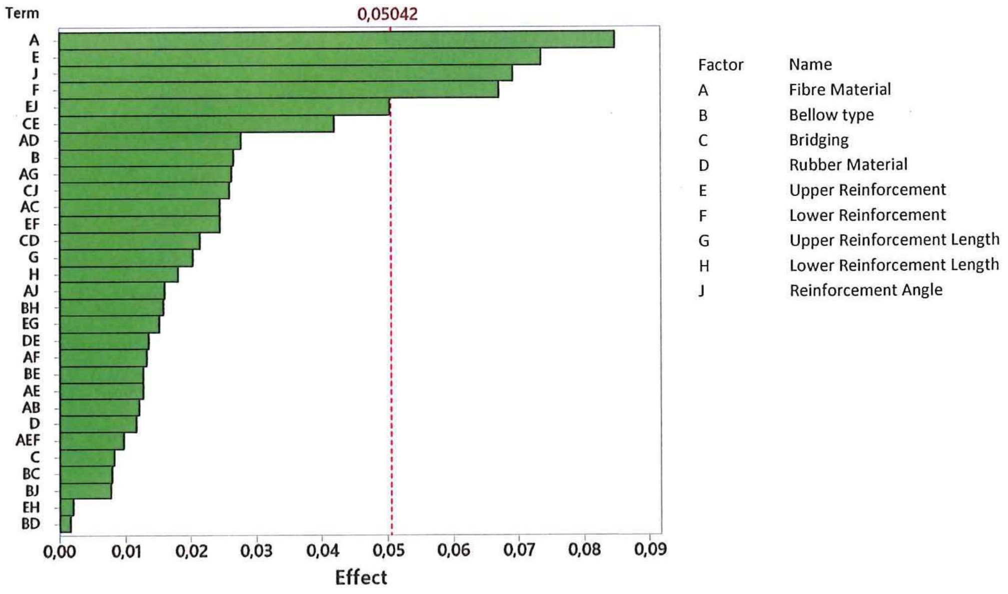

FIGURE 7.6: ELONGATED MAXIMUM FIBRE FORCE PARETO CHART

The effects on the maximum fibre force during lateral deformation are shown in the Pareto chart given in Figure 7.7. The most important main effects are the fibre material, upper and lower reinforcement. Furthermore the interaction of the fibre material with both upper and lower reinforcement has a significant effect.

This corresponds with the findings from Section 6.3. The fibre material determines the bending stiffness of the cylindrical region and thus the amount of shear deformation on the bellow. This shear deformation in turn linearly increases the fibre force on one side and linearly decreases it on the other for a single fibre direction. The same holds for the addition of reinforcement layers, these add bending stiffness to the cylindrical region, increasing the level of shear stresses. It is interesting to note that the upper reinforcement has a significantly higher effect than the lower reinforcement. This is due to the fact that the lower reinforcement is closer to the neutral axis of the expansion joint, thus adding less bending stiffness to the total expansion joint than the outer reinforcement layer. Furthermore the length of the upper reinforcement layers is longer than the lower reinforcement.

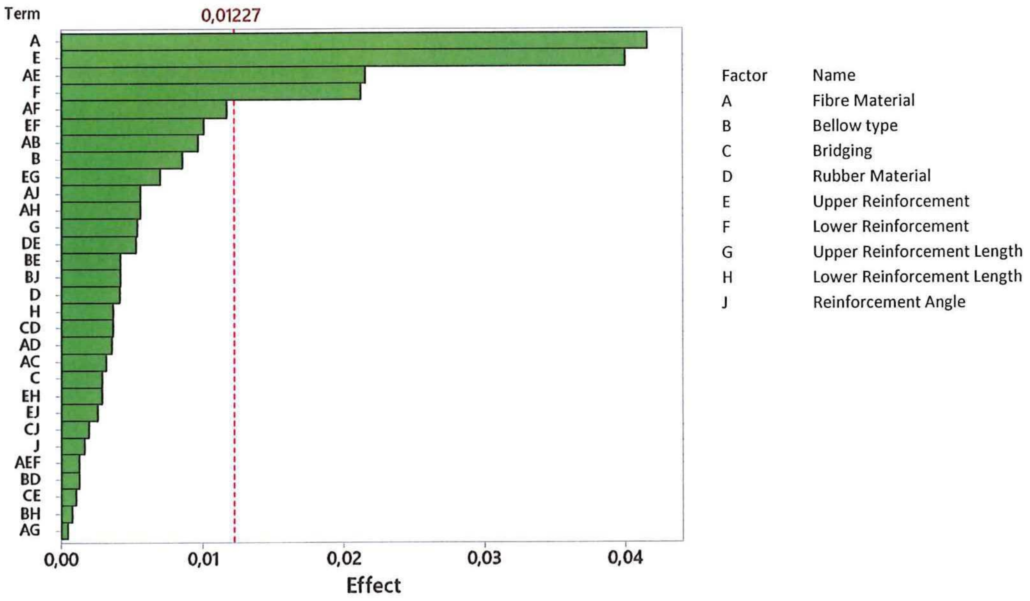

FIGURE 7.7: LATERAL MAXIMUM FIBRE FORCE PARETO CHART

The Pareto chart for the predicted lateral deformation at which compressive fibre forces occur is shown in Figure 7.8. In addition to the main effects that were of importance for the maximum fibre force during lateral deformation, the bellow shape and the interaction of upper reinforcement with the bellow shape are of importance as well. The difference between these Pareto charts is due to the fact that the maximum lateral deformation at which compressive fibres occur is determined by the fibre forces on the middle of the bellow whereas the maximum fibre force is the actual maximum fibre force throughout the model.

The effect of the bellow on the lateral deformation until compression can be explained by the size of the actual bellow. The hyperbolic bellow is somewhat smaller than the Corpo bellow. Therefore the same shear deformation has to be absorbed in a smaller region than is the case for a Corpo bellow.

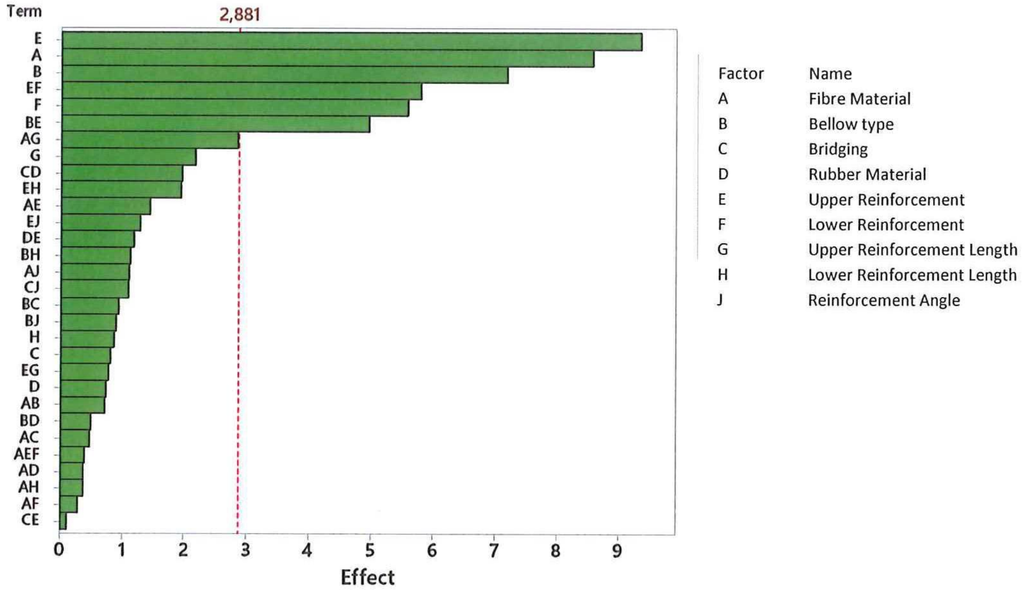

FIGURE 7.8: LATERAL DEFORMATION BEFORE COMPRESSIVE FIBRES PARETO CHART

The last Pareto chart shows the effects on the maximum fibre shear angle and is shown in Figure 7.9. This performance measure is mainly determined by the bellow shape, upper and lower reinforcement, reinforcement angle and the fibre material.

The influence of the reinforcement layers and reinforcement angle is due to their added stiffness to the cylindrical region. As this cylindrical region becomes stiffer the axial elongation has to be absorbed by the bellow, causing larger shear angles in this region. Furthermore the non-isotensoid fibre angles on the hyperbolic bellow causes larger shear angles than is the case with a Corpo bellow. The effect of the fibre material is again due to the difference in stiffness. As the Aramid fibres are stiffer, they tend to absorb the elongation by fibre shearing, whereas the Nylon fibres are more flexible and can absorb part of the axial elongation by stretching.

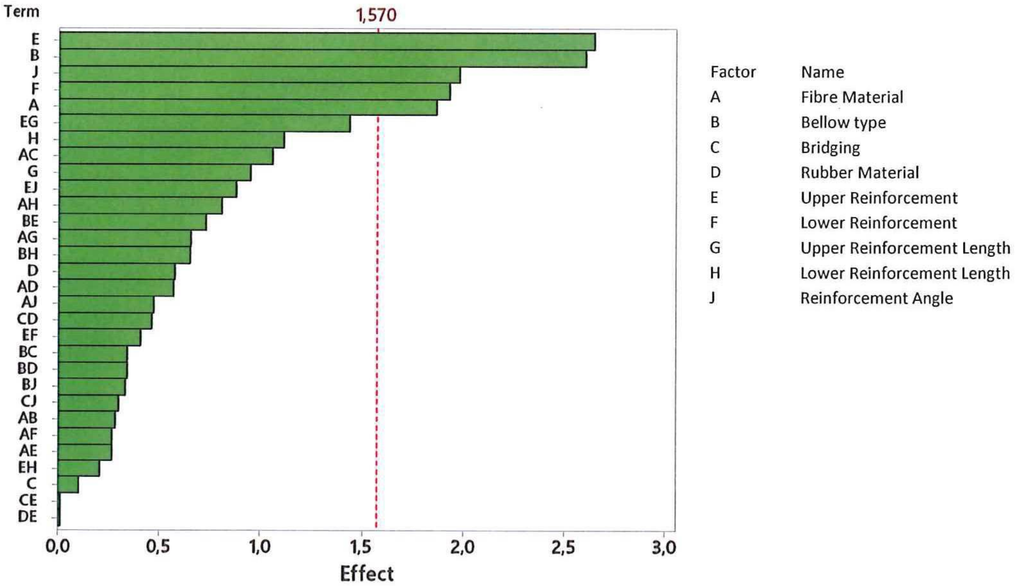

FIGURE 7.9: MAXIMUM FIBRE SHEAR PARETO CHART

The Pareto charts show the absolute effects on each performance measure. This gives a good indication on the most important effects, but does not show the actual effect itself. A complete overview of the relative main effects on the different performance measures is shown in Appendix C.2.

7.5 OPTIMAL DESIGN

The main and interaction effects can be used to determine an optimal design for the expansion joint. The final design has to perform well in each load case, therefore all the performance measures have to be accounted for when optimizing the design. As some performance measures are more important than others, a weight factor is assigned to each performance measure. The weight factors for both Aramid and Nylon designs are shown in Table 7.8.

For both material types, maximum rubber strain is an important performance measure as this is a common failure mode during dynamic testing. The maximum fibre forces in the different load cases all have an equal importance, as the expansion joints are burst tested in each deformation mode. Compressive fibre forces are detrimental for Aramid fibres but not for Nylon fibres, therefore this performance measure has a higher weight for Aramid designs. Next to the prediction of compressive fibres, this performance measure gives a good indication of the stress amplitudes during a lateral cycle. The maximum fibre shear angle has a fairly low weight as there has not been any expansion joint that has failed due to this failure mode. As Aramid fibres are more sensitive to fibre fretting, a slightly higher weight has been assigned.

TABLE 7.8: WEIGHT FACTORS PERFORMANCE MEASURES

Result	Deformation			Weight Factor Nylon	Weight Factor Aramid
Maximum Rubber Strain	30	[mm]	elongation	2	2
Maximum Fibre Force			restricted	1	1
	30	[mm]	elongation	1	1
	5	[mm]	lateral	1	1
Lateral Deformation Until Compressive Fibre Forces	5	[mm]	lateral	1	2
Maximum Fibre Shear Angle	30	[mm]	elongation	0,5	0,75

Again the Minitab software is used to determine an optimal design. This software creates a normalized general performance measure from the weighted performance measures. The effects of the different parameters on this general performance measure are determined, by which an optimal design can be determined. It is chosen to make separate optimal design for Nylon and Aramid fibres. These are shown in Table 7.9.

TABLE 7.9: PARAMETRIC OPTIMAL DESIGNS

Fibres	Bellow	Bridging	Rubber	Upper Reinforcement Length [mm]	Lower Reinforcement Length [mm]	Reinforcement Angle [°]
Nylon	Corpo	Yes	SBR	-	-	-
Aramid	Corpo	Yes	SBR	-	-	-

Both optimal designs have a Corpo bellow, bridging and SBR rubber without any reinforcement. Both static and dynamic tests have shown that expansion joints without any reinforcement show rubber cracking next to the flange. The 2-level Design of Experiments is thus not able to accurately describe this failure mode. Therefore it is required to enforce axial reinforcement during the optimization. New optimal designs are made taking this constraint into account. These optimal designs are shown in Table 7.10.

TABLE 7.10: REINFORCED OPTIMAL DESIGNS

Fibres	Bellow	Bridging	Rubber	Upper Reinforcement Length [mm]	Lower Reinforcement Length [mm]	Reinforcement Angle [°]
Nylon	Corpo	Yes	SBR	50	-	±45
Aramid	Corpo	Yes	SBR	-	20	0

The optimal reinforced designs still have a Corpo bellow, bridging and SBR rubber. For the Nylon design an upper reinforcement layer with full length and fibre angle of ±45° is given. The angle-ply reinforcement has less axial stiffness, limiting the stiffness discontinuity in the axial direction and thus the stress concentration. The optimal reinforced Aramid design on the other hand only has a short lower reinforcement layer with a 0° fibre angle. This unidirectional reinforcement layer has a higher axial stiffness that matches better with the stiff Aramid fibres. It should be noted that the 2-level parametric study assumes a linear effect with respect to the reinforcement length, therefore limiting the optimization to either the maximum or minimum allowed reinforcement length.

Next to the structural constraints there are some manufacturing constraints that have to be accounted for. One of these constraints is that the customer requires an inner layer of SBR and an outer layer of CR for the desired chemical resistance. Another manufacturing constraint is that a lower reinforcement layer cannot be combined with the bridging procedure. Therefore the optimal Aramid design has to be revised. This gives the optimal designs as shown in Table 7.11. It should be noted that the overall optimal design is the Nylon design as it performs better with respect to the normalized general performance measure.

TABLE 7.11: MANUFACTURABLE OPTIMAL DESIGNS

Fibres	Bellow	Bridging	Rubber	Upper Reinforcement Length [mm]	Reinforcement Angle [°]
Nylon	Corpo	Yes	SBR/CR	50	±45
Aramid	Corpo	Yes	SBR/CR	25	0

7.6 EFFECT OF REINFORCEMENT LENGTH

One of the major limitations of the 2-level parametric study that has been performed is that it assumes a linear relation between both levels of continuous parameters. The only continuous parameters that have been investigated are the reinforcement lengths. The relation between most of the performance measures and these parameters is not linear. Therefore its effects will be studied separately to determine the optimal length of the reinforcement layer. Both for the Nylon and Aramid optimal designs 5 different lengths of reinforcement are modelled to investigate its effects on the performance measures.

Figure 7.10 shows the maximum principal rubber strain with respect to the reinforcement length at each deformation mode. It is clearly visible that the lateral and axial elongated deformation modes cause the highest rubber strains. Short reinforcement lengths show severe rubber strains which are due to stress concentrations and subsequent necking of the rubber in the cylindrical region. The maximum rubber strain during lateral deformation shows a minimum at a reinforcement length of approximately 35 [mm], whereas the maximum rubber strain during axial elongation tends to decrease with increasing reinforcement length.

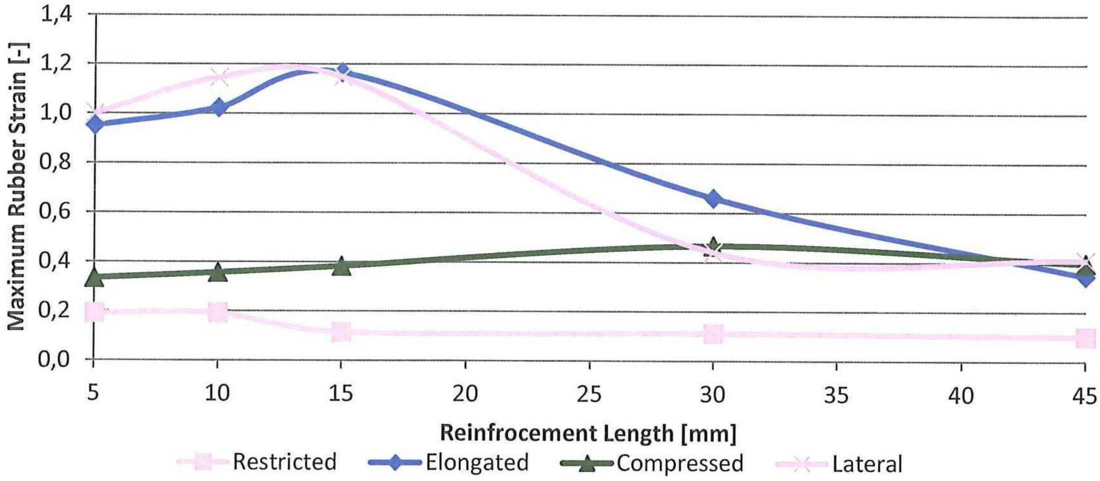

FIGURE 7.10: RUBBER STRAIN VS. REINFORCEMENT LENGTH

The maximum fibre force during the restricted and axial deformation modes with respect to the reinforcement length are shown in Figure 7.11. Again the most critical deformation mode is axial deformation. This shows an increase in maximum fibre force with increasing fibre length. This is due to the fact that the maximum fibre force during pressurization is evenly distributed over the bellow. At short reinforcement lengths the stress concentration caused by the reinforcement layer does not yet affect the forces in the bellow. With increasing reinforcement length this stress concentration approaches the bellow, causing the rise in fibre forces. Once the reinforcement layer overlaps the fibre bellow (>25 [mm]) the rise in fibre forces evens out as the stress concentration remains approximately the same, just as the originally evenly distributed fibre forces in the bellow.

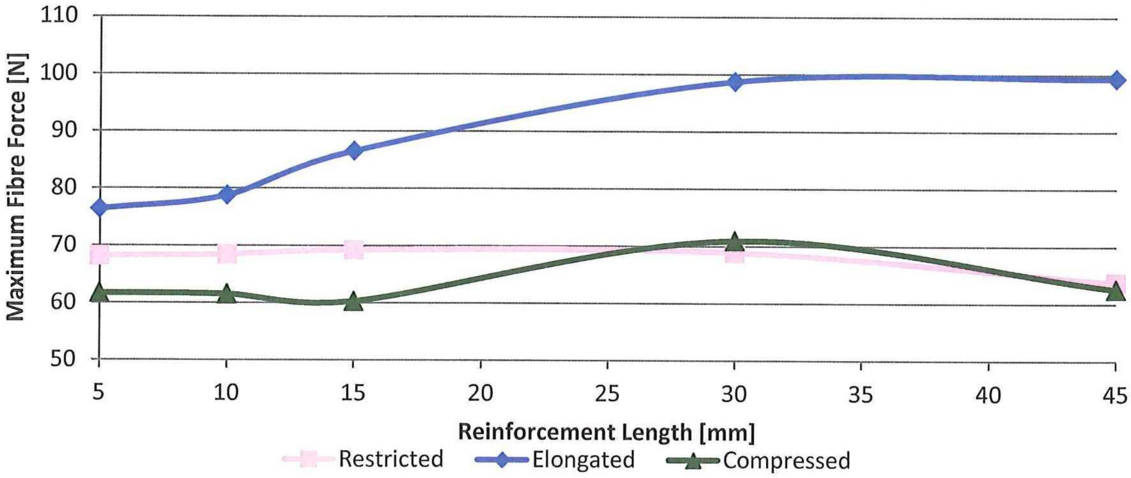

FIGURE 7.11: MAXIMUM FIBRE FORCE VS. REINFORCEMENT LENGTH

The predicted lateral deformation at which compressive fibres occur with respect to the reinforcement length is given in Figure 7.12. As can be seen the deformation at which fibre compression occurs decreases with increasing reinforcement length. This is due to the increase in bending stiffness of the prototype, increasing the shear deformation in the bellow. It should be noted that during cyclic testing a maximum lateral deformation of 20 [mm] is applied, which does not result in compressive fibre forces for the majority of the range of reinforcement lengths. Furthermore the Nylon fibres are better able handle compressive stresses.

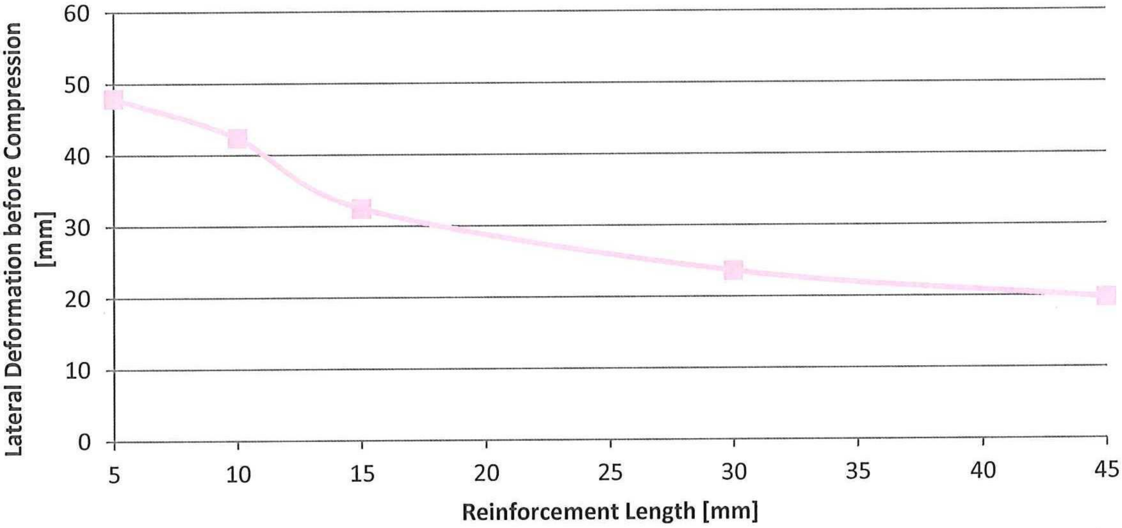

FIGURE 7.12: LATERAL DEFORMATION BEFORE COMPRESSION VS. REINFORCEMENT LENGTH

The last performance measure that is investigated is the maximum fibre shear angle. These are shown for different lengths of reinforcements during all deformation modes in Figure 7.13. As can be seen the influence of the reinforcement length on fibre shear angle is rather small. The only significant difference is visible during lateral deformation where a minimum is visible at a length of approximately 30 [mm].

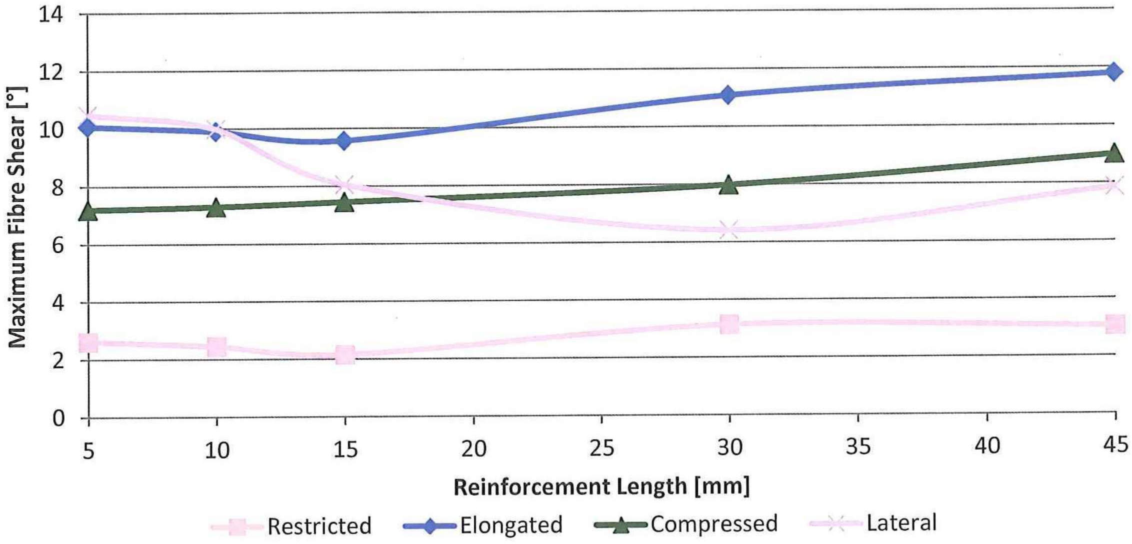

FIGURE 7.13: FIBRE SHEAR VS. REINFORCEMENT LENGTH

Considering all these performance measures an optimal reinforcement length has to be chosen. The maximum fibre shear angle is least important and therefore not taken into account. As the most common failure mode for Nylon prototypes is rubber cracking, the optimal reinforcement length has been based on Figure 7.10 resulting in an optimal reinforcement length of 35 [mm]. A shorter reinforcement length will show lower fibre forces during axial elongation but is likely to show rubber cracking. The final optimized expansion joint parameters are shown in Table 7.12. The internal geometry and fibre angles of this optimal design are shown in Appendix C.3.

TABLE 7.12: FINAL OPTIMAL DESIGN

Fibres	Bellow	Bridging	Rubber	Upper Reinforcement Length [mm]	Reinforcement Angle [°]
Nylon	Corpo	Yes	SBR/CR	35	±45

The same graphs have been determined for Aramid expansion joints as well and are shown in Appendix C.4. Even with an optimal reinforcement length, the Aramid expansion joints will show compressive fibre forces at relatively low lateral deformations. This indicates that an Aramid expansion joint is unable to deliver the same dynamic lateral performance as Nylon Expansion Joints.

7.7 VALIDATION

To validate the parametric study and optimization, prototypes have been made and tested. A great number of Aramid expansion joints for a wide range of burst pressures have been made. Extensive static and dynamic tests have been performed on these Aramid prototypes. Due to the limited availability of Nylon fibres with the correct coating, only four Nylon prototypes have been made. Therefore only two static and two dynamic tests have been performed on these prototypes.

Table 7.13 shows the average burst pressure of the most recent Aramid and Nylon expansion joints. In total 8 similar Aramid and 2 similar Nylon expansion joints have been statically tested. The Aramid expansion joints were designed for a burst pressure of 64 [bar] whereas the Nylon prototypes were designed for a burst pressure of 48 [bar]. Automated placement of the inner rubber, fibre and wrapping tape has been used on all prototypes. The outer rubber layers have been applied manually. The average test pressure and standard deviation of these prototypes can be seen in Table 7.13. The average burst pressures are nearly identical to the design pressure and the standard deviation is acceptable. This indicates that both Aramid and Nylon expansion joints can be designed with an accurate restricted burst pressure.

TABLE 7.13: DESIGN, AVERAGE AND STANDARD DEVIATION OF STATIC BURST TESTS

		Aramid	Nylon
Design Pressure	[bar]	64	48
Average Test Pressure	[bar]	64,3	48,0
Standard Deviation	[%]	7,0	8,1

One of the statically tested Nylon prototypes is nearly identical to the optimized design given in Table 7.12. Furthermore an Aramid prototype has been made with the exact same reinforcement length, but with a design pressure of 64 [bar]. The static test results of both of these prototypes are given in Table 7.14. Both prototypes exceed their design burst pressure and satisfy their static requirement.

TABLE 7.14: DESIGN AND BURST PRESSURE OF NEAR OPTIMAL DESIGNS

		Aramid	Nylon
Design Pressure	[bar]	64	48
Test Pressure	[bar]	64,3	51,9

The static performance is satisfied for most expansion joints. Dynamic testing on the other hand is more troublesome. So far there has not been an Aramid expansion joint that has satisfied the dynamic requirements. This is due to fibre compression as discussed in Section 6.3. The poor dynamic performance of these expansion joints has resulted in the change to Nylon fibres. The two Nylon prototypes that have been dynamically tested were identical to the optimal design as proposed in the previous Section. These Nylon prototypes are compared with two similar Aramid designs that have been dynamically tested. All of the prototypes are designed for a burst pressure of 48 [bar].

The dynamic testing consists of one million lateral cycles at 10 and/or 15 [mm] and a test pressure of 3 [bar] after which the prototypes are burst tested. Their results are shown in Table 7.15.

TABLE 7.15: DYNAMIC LATERAL TEST RESULTS

	Dynamic Cycles	Burst Pressure [bar]
Aramid	1.000.000 Lateral 10 [mm]	43
	150.000 Lateral 15 [mm]	Bursted during testing
Nylon	1.000.000 Lateral 15 [mm]	40
	1.000.000 Lateral 15 [mm] 1.000.000 Lateral 10 [mm]	49

As can be seen one of the Aramid prototypes performs quite well at a lateral cyclic deformation of 10 [mm]. When the same design was tested at a lateral deformation of 15 [mm], it failed prematurely at the test pressure of only 3 [bar]. This indicates the sensitivity of Aramid expansion joints to large lateral deformations. On the contrary, both Nylon prototypes survived the cyclic lateral deformation of 15 [mm] after which one of the prototypes has been burst tested at 40 [bar]. The other Nylon prototype did an additional dynamic test at a lateral deformation of 10 [mm]. This prototype showed a final burst pressure of 49 [bar]. This confirms that the cyclic lateral deformation has little effect on the performance of Nylon expansion joints. Furthermore both prototypes have been the first expansion joints that satisfy all static and dynamic requirements for the highest performance expansion joints.

7.8 EXPANSION JOINT DESIGN GUIDELINES

In this research the simulations, parametric study and performance tests have been applied to one of the smallest sizes of expansion joints (Ø = 100 [mm]). During the certification program of an entire range of expansion joints, larger sizes have to be developed as well. Some basic simulations have been performed on larger expansion joints (Ø = 250 [mm] and Ø = 600 [mm]) to investigate their stress distribution during the characteristic deformations (axial elongation/compression and lateral deformation). These simulations have confirmed that these larger sizes show a similar structural response as the smallest expansion joints. Therefore some general design guidelines can be given for the future development of expansion joints, these are listed below;

- Use Nylon fibres

When an expansion joint will be exerted to cyclic lateral deformation, Aramid fibres have to be avoided as this deformation mode is detrimental to its performance.

- Use a Corpo bellow

A Corpo bellow ensures an optimal stress distribution over the bellow, the advantage of more flexibility of a Hyperbolic bellow is neutralized, as an Hyperbolic bellow deforms to a similar shape as a Corpo bellow at working pressure.

- Use the bridging procedure

Bridging increases the axial strength of the cylindrical region, limiting excessive stretching of the rubber near the flanges that causes cracks.

- Apply local reinforcement

Testing has shown that any unreinforced expansion joint will exhibit rubber cracking near the flanges during cyclic testing. Therefore a layer of local reinforcement needs to be applied to limit the rubber strains near the flanges.

- Optimal reinforcement length

To reduce stress concentrations in both the rubber and the fibres, the stiffness discontinuity at the end of the local reinforcement has to be minimized. This is achieved by matching the fibre angle at the end of the reinforcement layer with the main fibre (as illustrated in Figure 7.14). This limits both the stiffness discontinuity as well as the interlaminar shear.

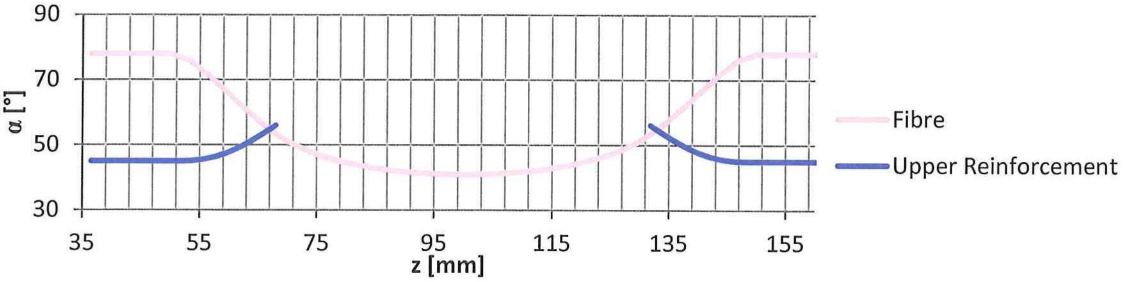

FIGURE 7.14: FIBRE ANGLES OF OPTIMAL NYLON DESIGN

8 CONCLUSION AND RECOMMENDATIONS

8.1 CONCLUSION

For the structural analysis of the unique combination of multi-layered filament wound cord-reinforced rubber, numerical FEA methods have to be used. The finite deformation of the flexible products requires aligned fibre meshes to prevent intra-ply shear locking. This limits the available mesh constructions to aligned triangle or truss elements for the fibres and aligned tetrahedral or unaligned hexahedral elements for the rubber.

Various combinations of elements for the fibres and rubber have been evaluated and compared. Satisfactory agreement with test results of a pneumatic muscle, single-layered and multi-layered expansion joints has been shown. The models are not accurate enough to give an exact prediction of the strength of the product, but can be used for a comparison between different designs.

During the simulations numerical instabilities have been encountered. These are caused by the combination of incompressible rubber with stiff fibres. Therefore the most important requirements for the meshes are their convergence and robustness. All combinations of linear elements showed satisfactory convergence for the fibre forces and reaction forces. The rubber strains on the other hand only showed a converged solution when using linear triangle elements embedded in unaligned linear hexahedral elements in Abaqus. Therefore it has been chosen to continue with this mesh type in further simulations.

During the simulations, only basic parameters for the rubber were known. To investigate the importance of the accuracy of the rubber properties and material models, material tests have been performed. The experimental results have been used to calibrate various material models. The basic Neo-Hookean material model that was given by the material supplier was not able to accurately model the response of the rubber in biaxial and planar shear tensile deformation modes. A comparison between an advanced calibrated 3th order Ogden material model and the given Neo-Hookean material model showed a noticeable difference in the reaction forces and rubber strains of a complete expansion joint. However, the basic model is a conservative approximation and it can therefore be argued whether the improvements achieved by using a fully calibrated model are worth the additional testing efforts.

To relate the simulations to actual product performance, the characteristic failure modes of expansion joints have been investigated. Rubber cracking is the most important failure mode of the rubber. Dynamic rubber crack growth is dependent on many parameters and can therefore not be predicted with the current model. However, the global analysis model that has been developed can be used to indicate critical regions with large rubber strains that cause rubber crack growth.

Fibre breaking is the most important static and dynamic failure mode. Static fibre fracture is easily determined by the simulated fibre forces. Dynamic fibre failure on the other hand is dependent on the fibre material and load amplitude. It has been shown that lateral deformation of expansion joints cause fibre compression, which is detrimental for Aramid fibres. Nylon fibres on the other hand are less sensitive to compression and are thus a suitable alternative to improve the dynamic performance of expansion joints.

The last failure mode is fibre fretting. Although this failure mechanism cannot be solely attributed to failure of an entire expansion joint it has an effect on the dynamic degradation of the fibres. This failure mode is caused by the shear angle of the fibres during cyclic deformation.

Design of Experiments has been used for a parametric study to investigate the influence of all design parameters on the performance of the product. The performance measures are based on the characteristic failure mechanisms. The effect of the reinforcement length on the performance of the product has been investigated separately. The parametric study and reinforcement length investigation have been used to determine an optimal expansion joint design that satisfies all manufacturing constraints. The optimal design parameters are repeated in Table 8.1.

TABLE 8.1: OPTIMAL EXPANSION JOINT DESIGN

Fibres	Bellow	Bridging	Rubber	Upper Reinforcement Length [mm]	Reinforcement Angle [°]
Nylon	Corpo	Yes	SBR/CR	35	±45

To validate the parametric study, optimal expansion joints were built and tested. Both the old and optimized design achieved their static pressure requirement. During lateral dynamic testing the optimized design showed a major improvement as it was the first expansion joint to satisfy all dynamic requirements. This improvement has proven that the numerical structural analysis method can be a valuable tool during the development of cord-reinforced rubber products.

Some design guidelines for expansion joints have been determined based on the results of the parametric study and the tests. These are listed below;

- Use Nylon Fibres
- Use a Corpo bellow
- Use the bridging procedure
- Apply local reinforcements

The optimal length of the reinforcement layer is the length where the angle of the angle-ply local reinforcement matches the fibre angle of the main fibre layer. This limits the stiffness discontinuity that causes stress concentrations.

8.2 RECOMMENDATIONS

The current model has proven to be a valuable tool during the design process. There are however numerical issues that limit the ease of use of the model during some extreme load cases. These are caused by numerical and/or structural instabilities (buckling). The structural instabilities can however be resolved by using the Riks solution method for the non-linear analysis. This will eliminate convergence problems caused by structural instabilities.

Further improvements can be made by using aligned truss elements for the fibres. During the simulations, truss elements have proven to be computationally efficient. Therefore the computational costs of the models could be reduced by developing an algorithm that constructs meshes with this type of element. This algorithm can be used for fully automated mesh generation that can be integrated in Taniq's design software.

An interesting extension of the current model is to incorporate viscoelastic effects. During the research it was shown that the burst pressure is highly dependent on the load rate. Viscoelasticity can be included in the numerical model if the correct material parameters are determined. It is expected that this can lead to a significant improvement of the accuracy of the simulation.

A limitation of the current global model is that its mesh is too coarse for an accurate analysis of the stress concentrations caused by local reinforcements. This could be investigated by using local-global models that use the stresses and strains given by the global model as boundary conditions for a fine mesh of a local region of the product. This will enable the investigation of delamination and crack growth.

Another effect that is worth investigating is the effect of advanced calibrated material models on the simulation of multi-layered expansion joints. During this research various material models were applied to a single-layered expansion joint that experienced little biaxial tension and planar shear. However, planar shear deformation could play an important role in the interlaminar behaviour of the rubber. Therefore the use of advanced calibrated material models might show a more significant difference when applied to these products.

Next to the structural analysis method itself, the Design of Experiments could be improved as well. The current 2-level design was unable to describe the rubber cracking failure mode. This is due to the non-linear relation between this failure mode and the length of the reinforcement layer. Experiments have shown that axial reinforcement is required to prevent this failure mode. Therefore the presence of a reinforcement layer is not a design variable anymore. This can be accounted for by writing an algorithm that determines the optimal reinforcement length for a given set of design parameters based on minimizing the stiffness discontinuity. This would eliminate the reinforcement parameters and enable the Design of Experiments to capture the rubber cracking failure mode.

REFERENCES

1. Taber, L.A., *Comparison of elasticity and shell theory results for large deformation of rubberlike shells.* International Journal of Non-Linear Mechanics, 1989. **24**(3): p. 237-249.
2. Koussios, S., *Filament winding: a unified approach.* 2004, DUP Science: Delft. p. 368 blz.
3. Vasiliev, V.V. and R.M. Jones, *Composite Pressure Vessels: Analysis, Design, and Manufacturing.* 2009: Bull Ridge Publishing.
4. Zu, L., *Design and optimization of filament wound composite pressure vessels.* 2012, BOXPress: Oisterwijk. p. 270 blz.
5. Sayem Uddin, M., E.V. Morozov, and K. Shankar, *The effect of filament winding mosaic pattern on the stress state of filament wound composite flywheel disk.* Composite Structures, 2014. **107**(0): p. 260-275.
6. Park, J.S., et al., *Analysis of filament wound composite structures considering the change of winding angles through the thickness direction.* Composite Structures, 2002. **55**(1): p. 63-71.
7. Barendse, R., *Fatigue Modeling of Corpo Reinforced Turbohoses*, in *Aerospace Engineering.* 2011, TU Delft: Delft. p. 115.
8. Mollers, R.J.W., *Development of a geodesic reinforced tire for a road racing bicycle*, in *Aerospace Engineering.* 2012, TU Delft: Delft. p. 133.
9. Krueger, R., et al., *Comparison of 2D finite element modeling assumptions with results from 3D analysis for composite skin-stiffener debonding.* Composite Structures, 2002. **57**(1-4): p. 161-168.
10. Luo, S.-Y. and T.-W. Chou, *Finite deformation of flexible composites.* Proceedings of the Royal Society of London. A. Mathematical and Physical Sciences, 1990. **429**(1877): p. 569-586.
11. Entwistle, K.M. and G.J. White, *A method for achieving effective load transfer between the inner and outer layers of a two-layer braided high-pressure hydraulic hose.* International Journal of Mechanical Sciences, 1977. **19**(4): p. 193-201.
12. FLIPSindia, *Rubber Expansion Joints*, aaaaaa15.jpg, Editor. 2007.
13. Spaanderdam, K., *Robotic Automation of Reinforced Expansion Joints, Market opportunities and product development.* 2014. p. 99.
14. Barendse, R., *Fatigue Modeling of Corpo Reinforced Turbohoses, Literature Research.* 2011, TU Delft: Delft. p. 78.
15. Baker, E.H., L. Kovalevsky, and F.L. Rish, *Structural Analysis of Shells.* 1972: McGraw-Hill.
16. Ten Thije, R.H.W., B. Davids, Editor. 2013.
17. ten Thije, R.H.W. and R. Akkerman, *Solutions to intra-ply shear locking in finite element analyses of fibre reinforced materials.* Composites Part a-Applied Science and Manufacturing, 2008. **39**(7): p. 1167-1176.
18. ten Thije, R.H.W., R. Akkerman, and J. Huetink, *Large deformation simulation of anisotropic material using an updated Lagrangian finite element method.* Computer Methods in Applied Mechanics and Engineering, 2007. **196**(33-34): p. 3141-3150.

19. Klute, G.K. and B. Hannaford, *Accounting for Elastic Energy Storage in McKibben Artificial Muscle Actuators.* Journal of Dynamic Systems, Measurement, and Control, 1998. **122**(2): p. 386-388.

20. SIMULIA, *Abaqus 6.13: Abaqus Analysis User's Guide*, in *Volume IV: Constraints & Interactions*. 2013, DSS. p. 699.

21. SIMULIA, *Rubber Course, Lesson 4: Defining Rubber*. 2008, Simuleon.

22. SIMULIA, *Rubber Course, Lesson 5: Modeling Issues and Tips*. 2008, Simuleon.

23. SIMULIA, *Abaqus 6.13: Abaqus Analysis User's Guide*, in *Volume II: Analysis*. 2013, DSS. p. 1471.

24. SIMULIA, *Abaqus 6.13: Abaqus Analysis User's Guide*, in *Volume III: Materials*. 2013, DSS. p. 699.

25. Treloar, L.R.G., *Mechanics of Rubber Elasticity.* Journal of Polymer Science Part C-Polymer Symposium, 1974(48): p. 107-123.

26. Cousineau, d.A., *Broken Outside*, broken_outside.jpg, Editor. 2012, Anvis.

27. Pidaparti, R.M.V. and A.W. May, *Micromechanical analysis of fatigue cracks in cord–rubber composites.* Composite Structures, 2001. **54**(4): p. 459-465.

28. Mars, W.V. and A. Fatemi, *A literature survey on fatigue analysis approaches for rubber.* International Journal of Fatigue, 2002. **24**(9): p. 949-961.

29. Lee, B.L. and D.S. Liu, *Cumulative Damage of Fiber-Reinforced Elastomer Composites under Fatigue Loading.* Journal of Composite Materials, 1994. **28**(13): p. 1261-1286.

30. Harbour, R.J., A. Fatemi, and W.V. Mars, *Fatigue life analysis and predictions for NR and SBR under variable amplitude and multiaxial loading conditions.* International Journal of Fatigue, 2008. **30**(7): p. 1231-1247.

31. Elices, M. and J. Llorca, *Fiber Fracture*. 2002: Elsevier Science. 406.

32. Knijnenberg, A., *Compressive Failure Behaviour of Novel Aramid Fibres*, in *Aerospace Engineering*. 2009, TU Delft: Delft. p. 168.

33. Milliken, *Pa 66 1880 2*. 2014. p. 1.

34. Milliken, *Milliken - Teijin Twaron Fiber Properties*. 2013. p. 2.

35. Cousineau, d.A., *tissu C2509*, R. Barendse, Editor. 2014.

36. Antony, J., *Design of Experiments for Engineers and Scientists*. 2003: Elsevier Science.

37. SIMULIA, *Rubber Course, Lesson 2: Material Models*. 2008, Simuleon.

38. Treloar, L., *The elasticity of a network of long-chain molecules—II.* Trans. Faraday Soc., 1943. **39**: p. 241-246.

39. Arruda, E.M. and M.C. Boyce, *A three-dimensional constitutive model for the large stretch behavior of rubber elastic materials.* Journal of the Mechanics and Physics of Solids, 1993. **41**(2): p. 389-412.

40. Rivlin, R., *Large elastic deformations of isotropic materials. IV. Further developments of the general theory.* Philosophical Transactions of the Royal Society of London. Series A, Mathematical and Physical Sciences, 1948. **241**(835): p. 379-397.

41. Enderle, H. and H.-G. Kilian, *General deformation modes of a van der Waals network*, in *Permanent and Transient Networks*. 1987, Springer. p. 55-61.

42. Yeoh, O., *Some forms of the strain energy function for rubber.* Rubber Chemistry and technology, 1993. **66**(5): p. 754-771.

43. Marlow, R., *A general first-invariant hyperelastic constitutive model.* Constitutive Models for Rubber, 2003: p. 157-160.

44. Ogden, R. *On isotropic tensors and elastic moduli.* in *Mathematical Proceedings of the Cambridge Philosophical Society*. 1974. Cambridge Univ Press.

Appendix A FINITE ELEMENT ANALYSIS

In this Appendix the designs of the products that have been used during the development of the FEA models are shown. The design of the pneumatic McKibben actuator is given in Section A.1, whereas the design of a single layered expansion joint is given in Section A.2. The method of calculating the reinforcement fibre angle is explained in Section A.3. At last the design of a reinforced expansion joint is illustrated in Section A.4.

A.1 MCKIBBEN ACTUATOR GEOMETRY AND FIBRE ANGLE

The McKibben actuator is a cylindrical rubber bladder with a braided fibre layer on top. Its profile is shown in Figure A.1.

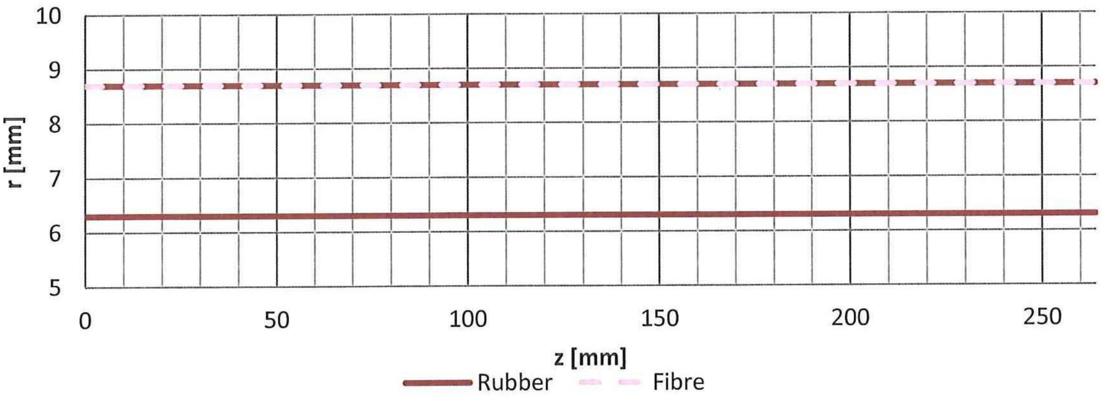

FIGURE A.1: MCKIBBEN PROFILE

The braid in the McKibben actuator has a constant angle, which is shown in Figure A.2.

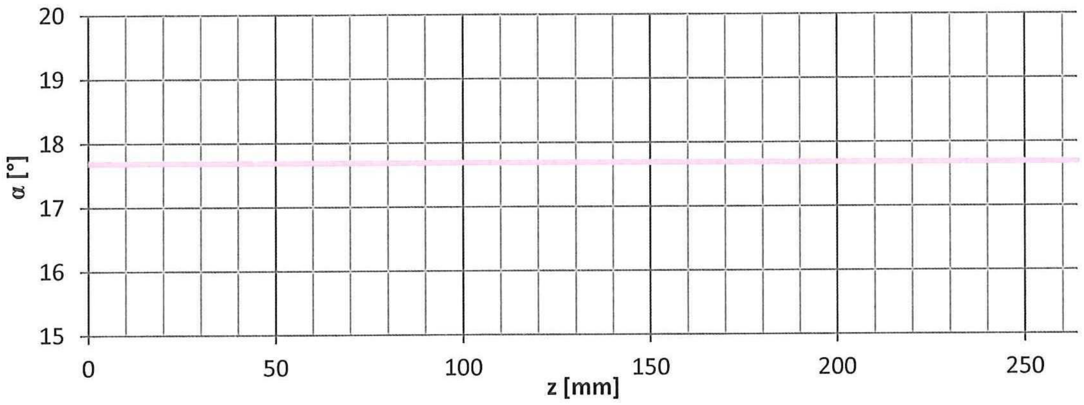

FIGURE A.2: MCKIBBEN FIBRE ANGLE

The properties of the materials used in the McKibben actuator are given in Table A.1.

TABLE A.1: MCKIBBEN MATERIAL PROPERTIES

Rubber	$C_{10} = 118{,}4\ kPa$		$C_{01} = 105{,}7\ kPa$	
Fibre	$E = 3{,}5\ GPa$	$\nu = 0{,}37$	$A = 1{,}791\ mm^2$	$s = 2{,}8\ mm$

A.2 SINGLE LAYERED EXPANSION JOINT GEOMETRY AND FIBRE ANGLE

The single layered expansion joint that has been modelled is a so called bridging prototype (see Section 3.2). Its bellow has been designed using the Taniqwind software and is a so called Corpo bellow (Section 3.3). The inner and outer rubber layers are both 3,3 [mm] thick. The profile of both the rubber and the fibre layers are shown in Figure A.3.

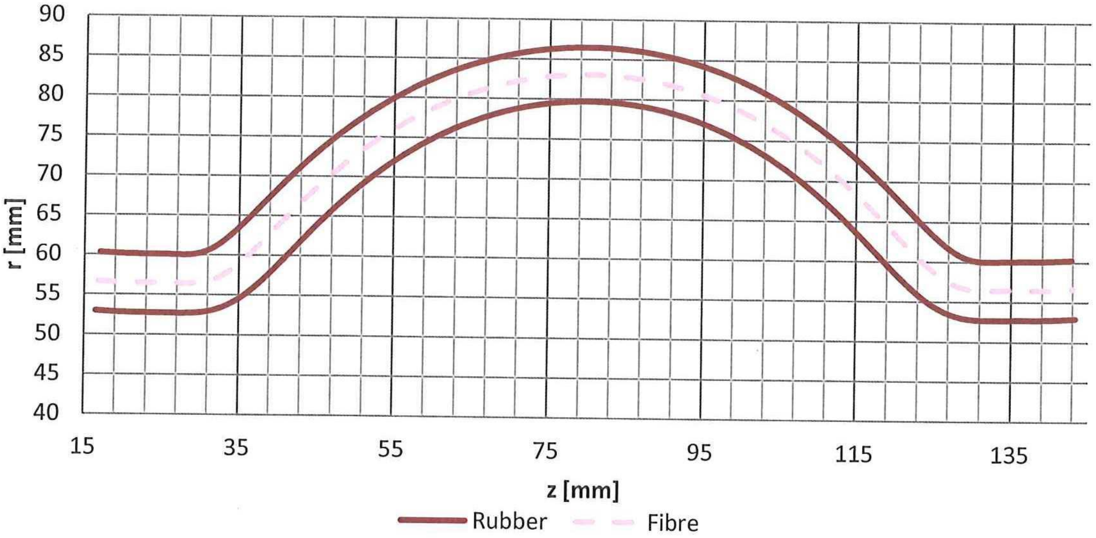

FIGURE A.3: SINGLE LAYERED EXPANSION JOINT PROFILE

As the expansion joint is a bridging type, its fibre angle towards the flanges remains rather low. It should be noted that the effect on the bridging procedure on the actual fibre angles is unknown, as this procedure has been developed recently. The assumed fibre angle of this bridging expansion joint is shown in Figure A.4.

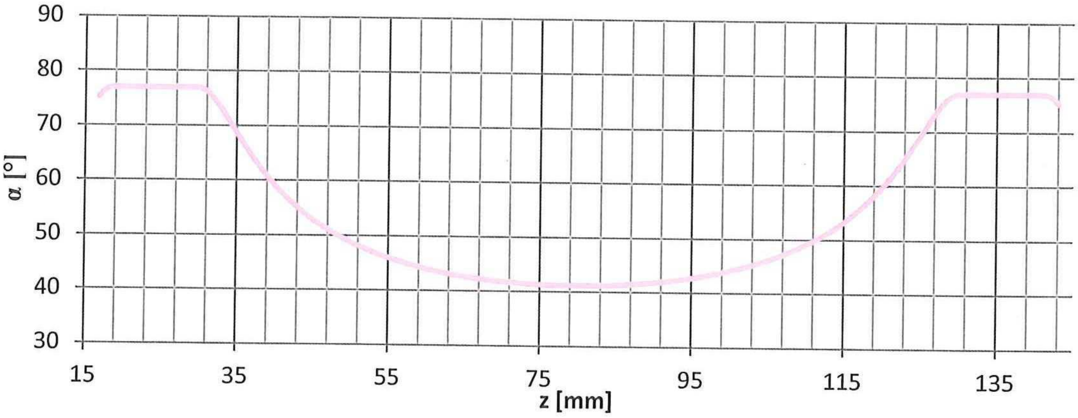

FIGURE A.4: SINGLE LAYERED EXPANSION JOINT FIBRE ANGLE

The properties of the fibre and rubber of the single layered expansion joint are given in Table A.2.

TABLE A.2: EXPANSION JOINT MATERIAL PROPERTIES

Rubber	$C_{10} = 118{,}4\ kPa$			
Fibre	$E = 36{,}09\ GPa$	$\nu = 0{,}36$	$A = 0{,}28\ mm^2$	$n = 248$

A.3 REINFORCEMENT ANGLE DETERMINATION

In cord-reinforced rubber products, local reinforcements are applied manually. In the case of axial unidirectional (0°) reinforcement the fibre angle will not shift due to the profile of the product. However, this is not the case for a woven angle-ply layer (±45°). In this Section the Equations used to determine the shifting fibre angles of such reinforcements are presented.

When applying a local reinforcement layers, the undeformed circumferential length is determined by the circumference at the minimum radius of the reinforced region. At this location the angle-ply prepreg will not be stretched and retain its fibre angle of ±45°. However as the radius changes, the stiff fibres will tend to shift to compensate for the stretch in circumferential direction. To determine the shifted fibre angles it is assumed that the fibre length of an infinitesimally small section remains constant while the circumference changes, as illustrated in Figure A.5.

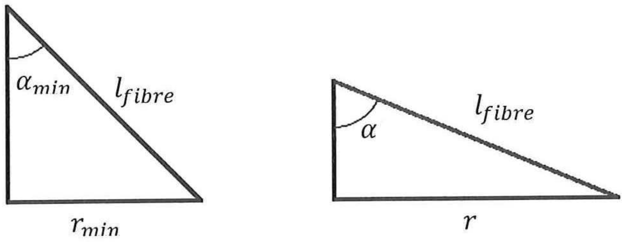

FIGURE A.5: FIBRE ANGLE SHIFT

This results in an inverse Clairaut relation, as given in Equation A.1.

$$l_{fibre} = constant = \frac{r}{\sin \alpha} \qquad \text{A.1}$$

The constant fibre length can be determined using the unshifted fibre angle at the minimum radius. Therefore the shifted fibre angle can be determined at any position along the radial profile using Equation A.2.

$$\alpha = \sin^{-1}\left(\frac{r \sin \alpha_{min}}{r_{min}}\right) \qquad \text{A.2}$$

A.4 REINFORCED EXPANSION JOINT GEOMETRY AND FIBRE ANGLES

The reinforced expansion joint that has been modelled is an original design by Taniq and has been extensively tested by one of its customers. It has both an outer and inner layer of angle-ply reinforcement. The rubber thicknesses of the inner and outer layer are both 3,3 [mm]. The increased thickness towards the ends is caused by the fibre build-up as the fibres approach a winding angle of 90° due to the manufacturing constraints of the flanges. The profiles of the fibre and rubber layers are shown in Figure A.5.

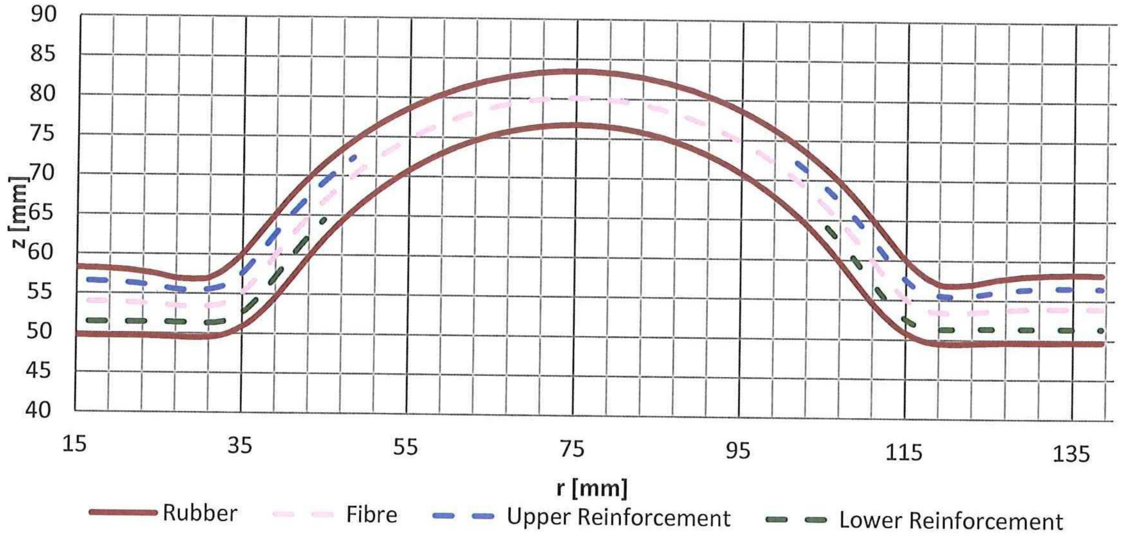

FIGURE A.6: REINFORCED EXPANSION JOINT PROFILE

The fibre angles of the main and reinforcement layers are shown in Figure A.6. The peak after the bellow is made to reduce the tendency of the expansion joint to stretch in the axial direction during pressurization.

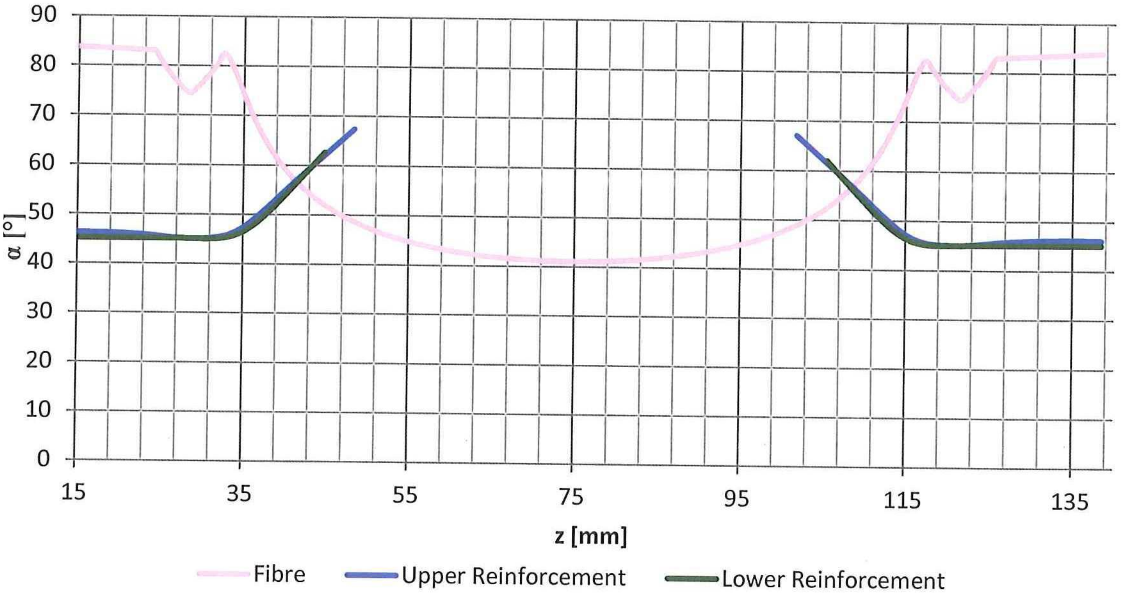

FIGURE A.7: REINFORCED EXPANSION JOINT FIBRE ANGLES

The fibre and rubber material properties for the reinforced expansion joint are the same as for the single layered expansion join, as given in Table A.2. In addition, the material properties of the reinforcement layer are given in Table A.3.

TABLE A.3: REINFORCEMENT MATERIAL PROPERTIES

Fibre Reinforcement	$E = 2{,}0\ GPa$	$\nu = 0{,}39$	$A = 0{,}83\ mm^2$	$s = 1{,}39\ mm$

Appendix B RUBBER

In this appendix the strain energy potentials that have been investigated are discussed in Section B.1. Next the calibrated material model parameters for CR and NR are given in Section B.2, whereas their stress-stretch responses for the three characteristic deformation modes are shown in Section B.3. At last the stability ranges of the unstable models for these rubber types are given in Section B.4.

B.1 STRAIN ENERGY POTENTIALS

Strain energy potentials describe the strain energy stored per unit of reference volume as a function of the strain. There are several strain energy potentials to model incompressible hyperelastic materials. Most strain energy potentials are phenomenological models based on continuum mechanics that use series expansion to imitate the characteristic stress-strain response. More recent models are physically motivated models that are based on the micromechanical phenomena in the elastomer. Each of the strain energy potentials has its own benefits and drawbacks but one of the most important differences is the ease of calibration of the models. [37]

B.1.1 NEO HOOKEAN

The most basic hyperelastic material model is the Neo-Hookean model. This is a phenomenological first-order reduced polynomial proposed by Treloar in 1943. [38] Its strain energy potential is given by Equation B.1 where C_{10} is a calibration constant based on the initial shear modulus.

$$U = C_{10}(\bar{I}_1 - 3) \qquad \text{B.1}$$

B.1.2 ARRUDA-BOYCE

The Arruda-Boyce material model is one of the few physically motivated models. It is based on a representative hexahedron volume in which 8 polymer chains emitting from the centre to the corners are modelled. [39] It has been developed in 1993 and its strain energy potential is given by Equation B.2. The material parameters are the initial shear modulus μ and the polymer chain locking stretch λ_m which defines the start of the characteristic upturn.

$$\begin{aligned} U = \mu\Bigg(\frac{1}{2}(\bar{I}_1 - 3) + \frac{1}{20{\lambda_m}^2}\left({\bar{I}_1}^2 - 3\right) + \frac{11}{1050{\lambda_m}^4}\left({\bar{I}_1}^3 - 27\right) + \frac{19}{7000{\lambda_m}^6}\left({\bar{I}_1}^4 - 81\right) \\ + \frac{519}{673750{\lambda_m}^8}\left({\bar{I}_1}^5 - 243\right)\Bigg) \end{aligned} \qquad \text{B.2}$$

B.1.3 MOONEY-RIVLIN

The Mooney-Rivlin model is one of the most commonly used models. It is a phenomenological second-order full polynomial model that allows a slight change of shape in comparison with the Neo-Hookean model, making it a reasonable fit up to moderate strains. The final model has been proposed in 1948 and its strain energy potential is given in Equation B.3. [40] One of the drawbacks of this model is that it can become unstable at low strains for certain combinations of parameters.

$$U = C_{10}(\bar{I}_1 - 3) + C_{01}(\bar{I}_2 - 3) \qquad \text{B.3}$$

B.1.4 VAN DER WAALS

The van der Waals model is a physically motivated model based on a network of polymer chains that are bonded by van der Waals forces. It has been developed in 1987 and its strain energy potential is given by Equation B.4. [41] Here μ is the initial shear modulus again and λ_m the polymer chain locking stretch. In addition, α accounts for the van der Waals interaction between the polymer chains. The β parameter is the strain invariant mixture parameter and has an empirical nature.

$$U = \mu\left(-({\lambda_m}^2 - 3)\left(ln\left(1 - \sqrt{\frac{\tilde{I} - 3}{{\lambda_m}^2 - 3}}\right) + \sqrt{\frac{\tilde{I} - 3}{{\lambda_m}^2 - 3}}\right) - \frac{2}{3}\alpha\left(\frac{\tilde{I} - 3}{2}\right)^{\frac{2}{3}}\right) \qquad \text{B.4}$$

$$\tilde{I} = (1 - \beta)\bar{I}_1 + \beta\bar{I}_2$$

B.1.5 YEOH

The Yeoh model is a phenomenological third-order reduced polynomial model that is able to capture the characteristic upturn at large strains of hyperelastic materials. It was proposed in 1993 and its strain energy potential is given by Equation B.5. [42]

$$U = C_{10}(\bar{I}_1 - 3) + C_{20}(\bar{I}_1 - 3)^2 + C_{30}(\bar{I}_1 - 3)^3 \qquad \text{B.5}$$

B.1.6 MARLOW

The Marlow model is a general first invariant model that exactly reproduces test data and has been developed in 2003. [43] Its strain energy potential is described by a deviatoric function of the first strain invariant as given in Equation B.6. This model works best when calibrated to detailed test data from a single deformation mode.

$$U = U_{dev}(\bar{I}_1) \qquad \text{B.6}$$

B.1.7 OGDEN

The Ogden model is a phenomenological full polynomial model. This model differs from other models in that it uses principal stretches instead of strain invariants. Furthermore the powers used are real values rather than integers, providing more accuracy. The model was proposed in 1974 and its strain energy potential for a common third-order model is given in Equation B.7. [44] Although this model is able to describe the behaviour of the rubber accurately over large strain ranges, it has to be calibrated with detailed test data of all characteristic deformation modes.

$$U = \sum_{i=1}^{N} \frac{2\mu_i}{{\alpha_i}^2} \left(\overline{\lambda_1}^{\alpha_i} + \overline{\lambda_2}^{\alpha_i} + \overline{\lambda_3}^{\alpha_i} - 3 \right) \qquad \text{B.7}$$

B.2 MATERIAL MODEL RARAMETERS FOR CR AND NR

The calibrated material model parameters for CR are given in Table B.1.

TABLE B.1: MATERIAL MODEL PARAMETERS FOR CR

Material Model	Parameters					
Neo-Hookean Given	$C_{10} = 6,10\ 10^5$					
Neo-Hookean Measured	$C_{10} = 6,23\ 10^5$					
Arruda-Boyce	$\mu = 1,25\ 10^6$		$\mu_0 = 1,25\ 10^6$		$\lambda_m = 2,63\ 10^3$	
Mooney-Rivlin	$C_{10} = 4,78\ 10^5$			$C_{01} = 2,33\ 10^5$		
van der Waals	$\mu = 1,18\ 10^6$		$\lambda_m = 10,0$		$\alpha = 0,17$	
Yeoh	$C_{10} = 7,58\ 10^5$		$C_{20} = -1,14\ 10^5$		$C_{30} = 1,63\ 10^4$	
Marlow	*test data*					
Ogden, N=3 approximation	$\mu_1 = 1,26\ 10^6$	$\alpha_1 = 1,16$	$\mu_2 = 1,61\ 10^4$	$\alpha_2 = 6,81$	$\mu_3 = 6,81\ 10^3$	$\alpha_3 = -3,32$
Ogden, N=3 full tests	$\mu_1 = 1,61\ 10^6$	$\alpha_1 = -0,25$	$\mu_2 = 5,28\ 10^3$	$\alpha_2 = 8,16$	$\mu_3 = 9,32\ 10^4$	$\alpha_3 = -5,84$

The calibrated material model parameters for NR are given in Table B.2.

TABLE B.2: MATERIAL MODEL PARAMETERS FOR NR

Material Model	Parameters					
Neo-Hookean Measured	$C_{10} = 4,71\ 10^5$					
Arruda-Boyce	$\mu = 9,26\ 10^5$		$\mu_0 = 9,47\ 10^5$		$\lambda_m = 5,23$	
Mooney-Rivlin	$C_{10} = 6,12\ 10^5$			$C_{01} = -2,38\ 10^5$		
van der Waals	$\mu = 8,95\ 10^5$		$\lambda_m = 4,73$		$\alpha = 0,44$	
Yeoh	$C_{10} = 4,79\ 10^5$		$C_{20} = -2,97\ 10^4$		$C_{30} = 6,45\ 10^3$	
Marlow	*test data*					
Ogden, N=3 approximation	$\mu_1 = 9,19\ 10^5$	$\alpha_1 = 1,46$	$\mu_2 = 1,72\ 10^4$	$\alpha_2 = 6,77$	$\mu_3 = 1,71\ 10^4$	$\alpha_3 = -2,67$
Ogden, N=3 full tests	$\mu_1 = 1,54\ 10^6$	$\alpha_1 = -0,88$	$\mu_2 = 1,07\ 10^3$	$\alpha_2 = 9,98$	$\mu_3 = 5,35\ 10^4$	$\alpha_3 = -6,57$

B.3 FITTED MATERIAL MODELS FOR CR AND NR

The uniaxial stress-stretch responses for CR material models are shown in Figure B.1.

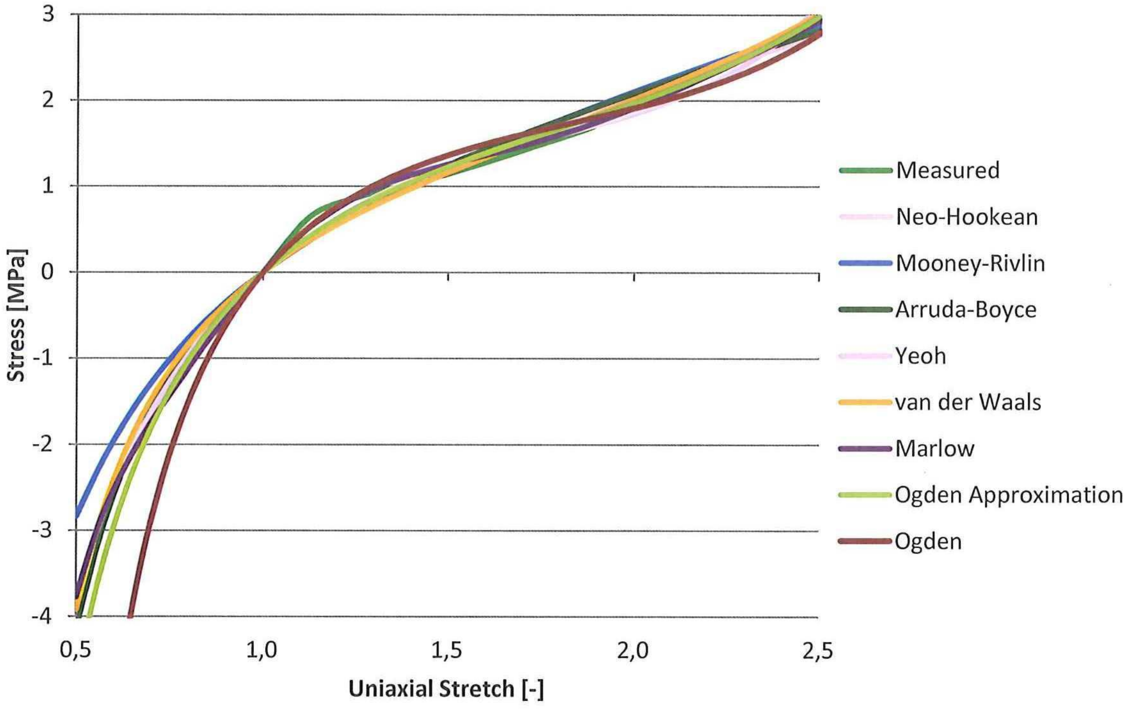

FIGURE B.1: UNIAXIAL STRESS STRETCH RESPONSE CR

The biaxial stress-stretch responses for the CR material models are shown in Figure B.2.

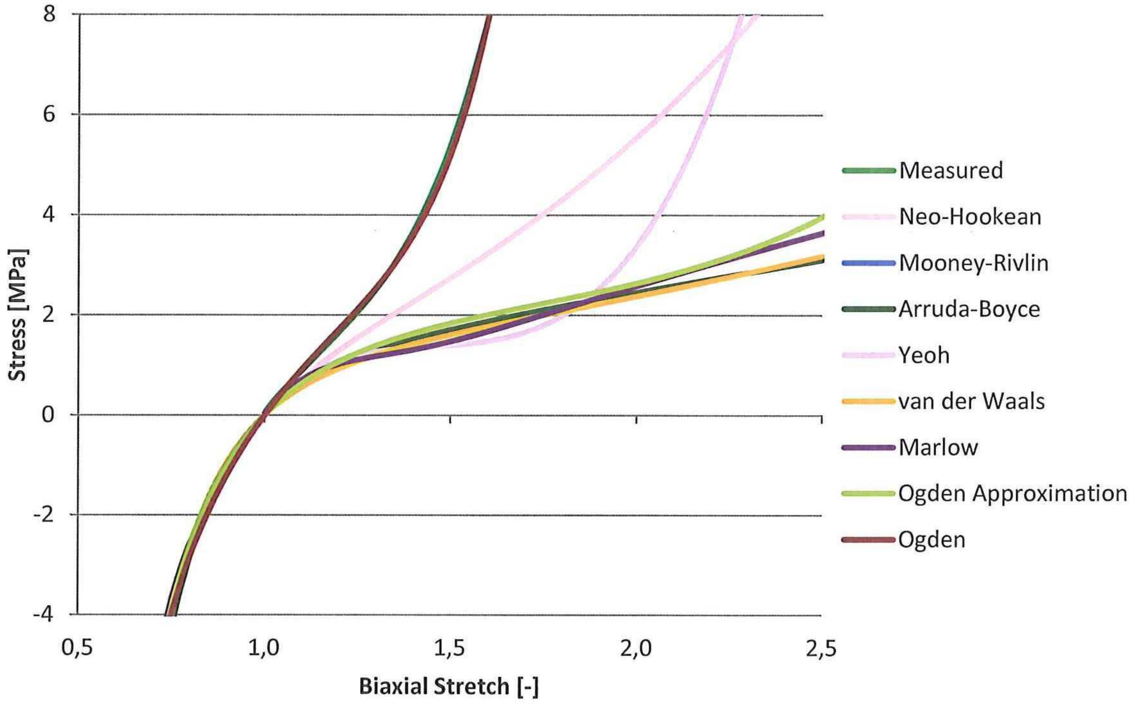

FIGURE B.2: BIAXIAL STRESS STRETCH RESPONSE CR

The planar shear stress-stretch responses for the CR material models are shown in Figure B.3.

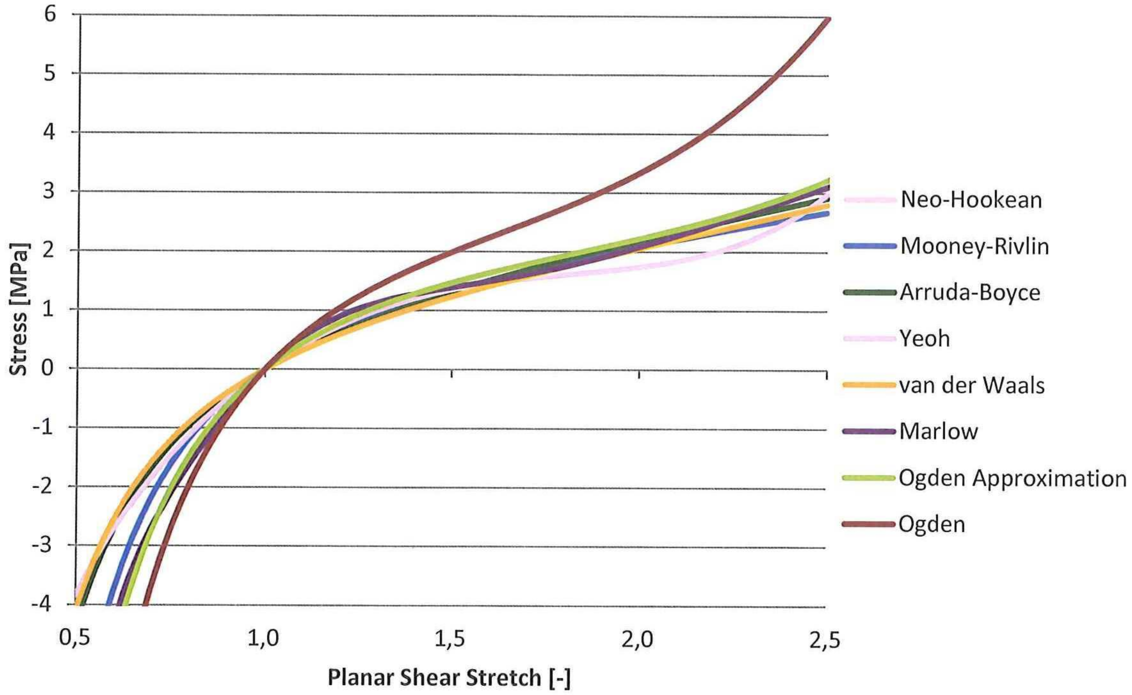

FIGURE B.3: PLANAR SHEAR STRESS STRETCH RESPONSE CR

The uniaxial stress-stretch responses of the NR material models are shown in Figure B.4.

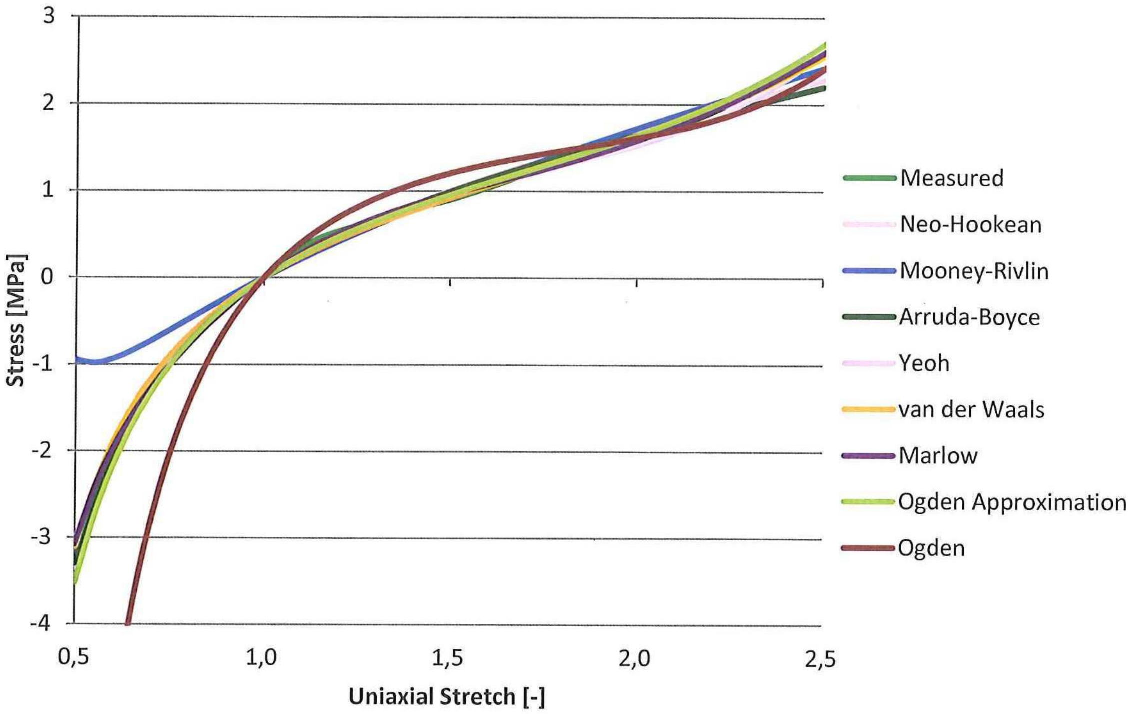

FIGURE B.4: UNIAXIAL STRESS STRETCH RESPONSE NR

The biaxial stress-stretch responses for the NR material models are shown in Figure B.5.

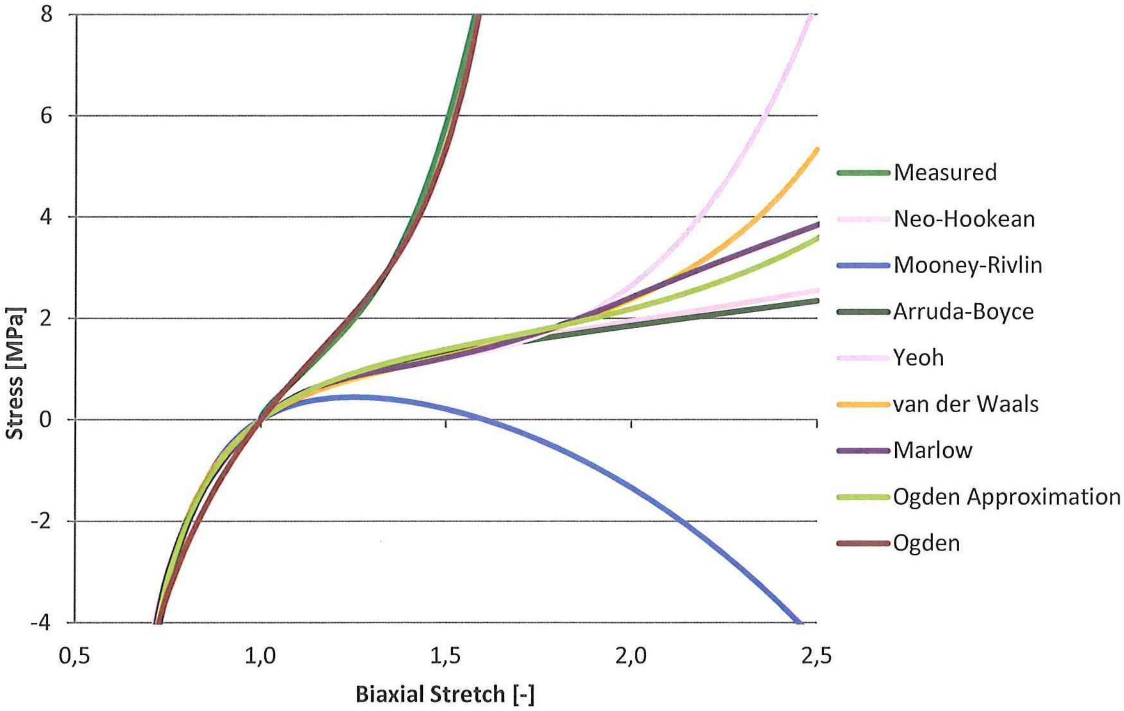

FIGURE B.5: BIAXIAL STRESS STRETCH RESPONSE NR

The planar shear stress-stretch responses of the NR material models are shown in Figure B.6.

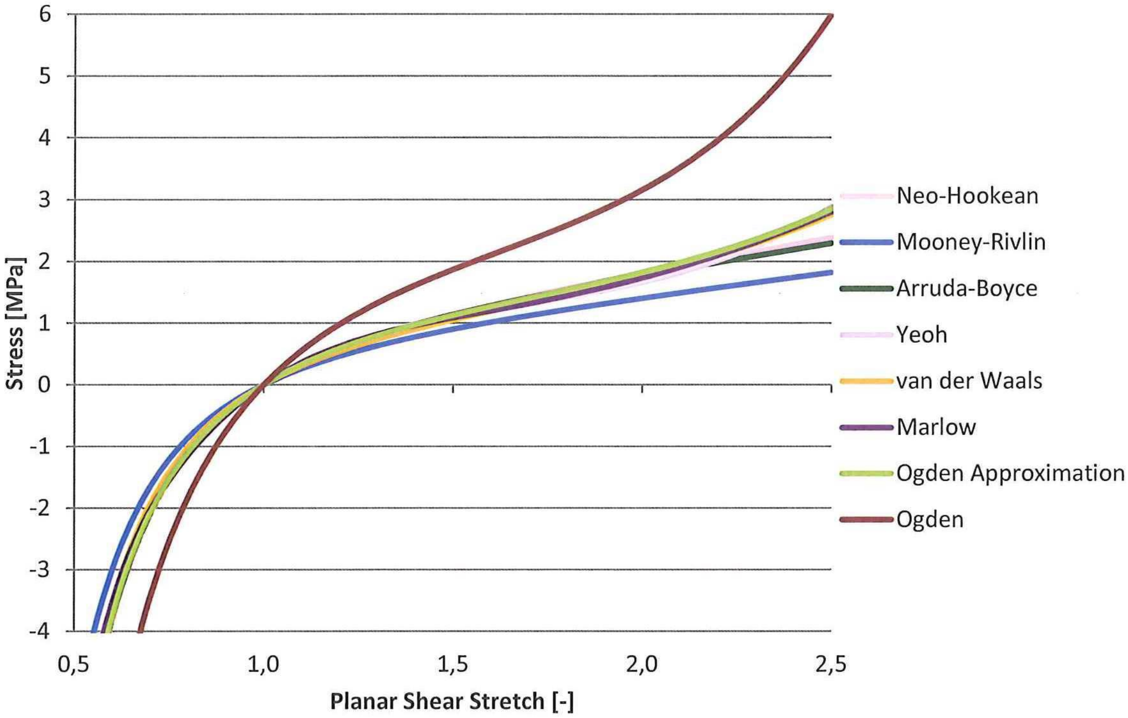

FIGURE B.6: PLANAR SHEAR STRESS STRETCH RESPONSE NR

B.4 UNSTABLE MATERIAL MODELS FOR CR AND NR

The only unstable CR material model is the van der Waals model, its stability range is given in Table B.3.

TABLE B.3: UNSTABLE CR MATERIAL MODELS

Material Model	Stability Range Uniaxial	Stability Range Planar Shear	Stability Range Biaxial
van der Waals	$0{,}02 \leq \lambda \leq 10{,}00$ [-]	$0{,}1 \leq \lambda \leq 9{,}96$ [-]	$0{,}32 \leq \lambda \leq 7{,}08$ [-]

For NR the Mooney-Rivlin and the van der Waals model are unstable, their stability ranges are listed in Table B.4.

TABLE B.4: UNSTABLE NR MATERIAL MODELS

Material Model	Stability Range Uniaxial	Stability Range Planar Shear	Stability Range Biaxial
Mooney-Rivlin	$0{,}6 \leq \lambda \leq 1{,}61$ [-]	$0{,}66 \leq \lambda \leq 1{,}53$ [-]	$0{,}79 \leq \lambda \leq 1{,}29$ [-]
van der Waals	$0{,}09 \leq \lambda \leq 4{,}69$ [-]	$0{,}22 \leq \lambda \leq 4{,}62$ [-]	$0{,}46 \leq \lambda \leq 3{,}35$ [-]

Appendix C DESIGN OF EXPERIMENTS

In this Appendix the confounded interaction effects of the Design of Experiments are listed in Section C.1. Section C.2 shows all main effects on the different performance measures. The final optimized design geometry and winding angles are shown in Section C.3. At last the effects of reinforcement length on the performance measures for Aramid expansion joints are illustrated in Section C.4.

C.1 CONFOUNDED INTERACTION EFFECTS

The confounded interaction effects for the fractional factorial Design of Experiments are listed in Table C.1. It should be noted that confounding is only undesirable if both interaction effects that are confounded are expected to have a significant influence on the performance measures. This is not the case for the confounded interaction effects for this Design of Experiments and therefore it is able to indicate all important parametric effects.

TABLE C.1: CONFOUNDED INTERACTION EFFECTS

<table>
<tr><th colspan="4">Confounded Interaction Effects</th></tr>
<tr><td colspan="2">Fibre - Bellow</td><td colspan="2">Lower Reinforcement – Upper Reinforcement Length</td></tr>
<tr><td colspan="2">Fibre - Fibre Angle</td><td colspan="2">Lower Reinforcement – Lower Reinforcement Length</td></tr>
<tr><td colspan="2">Fibre - Rubber</td><td colspan="2">Lower Reinforcement - Reinforcement Angle</td></tr>
<tr><td>Fibre - Lower Reinforcement</td><td>Bellow - Upper Reinforcement Length</td><td>Fibre Angle - Lower Reinforcement Length</td><td>Rubber - Reinforcement Angle</td></tr>
<tr><td colspan="2">Fibre - Upper Reinforcement Length</td><td colspan="2">Bellow - Lower Reinforcement</td></tr>
<tr><td colspan="2">Fibre - Lower Reinforcement Length</td><td colspan="2">Fibre Angle - Lower Reinforcement</td></tr>
<tr><td colspan="2">Fibre - Reinforcement Angle</td><td colspan="2">Rubber - Lower Reinforcement</td></tr>
<tr><td colspan="2">Bellow - Fibre Angle</td><td colspan="2">Upper - Lower Reinforcement Length</td></tr>
<tr><td colspan="2">Bellow - Rubber</td><td colspan="2">Upper - Reinforcement Angle</td></tr>
<tr><td colspan="2">Bellow - Lower Reinforcement Length</td><td colspan="2">Fibre Angle - Upper Reinforcement Length</td></tr>
<tr><td colspan="2">Bellow Shape - Reinforcement Angle</td><td colspan="2">Rubber Material - Upper Reinforcement Length</td></tr>
<tr><td colspan="2">Fibre Angle - Rubber Material</td><td colspan="2">Lower Reinforcement Length – Reinforcement Angle</td></tr>
<tr><td colspan="2">Fibre Angle - Reinforcement Angle</td><td colspan="2">Rubber - Lower Reinforcement Length</td></tr>
</table>

C.2 EFFECTS OF MAIN PARAMETERS ON PERFORMANCE

The main effects on the maximum principal rubber strain are shown in Figure C.1.

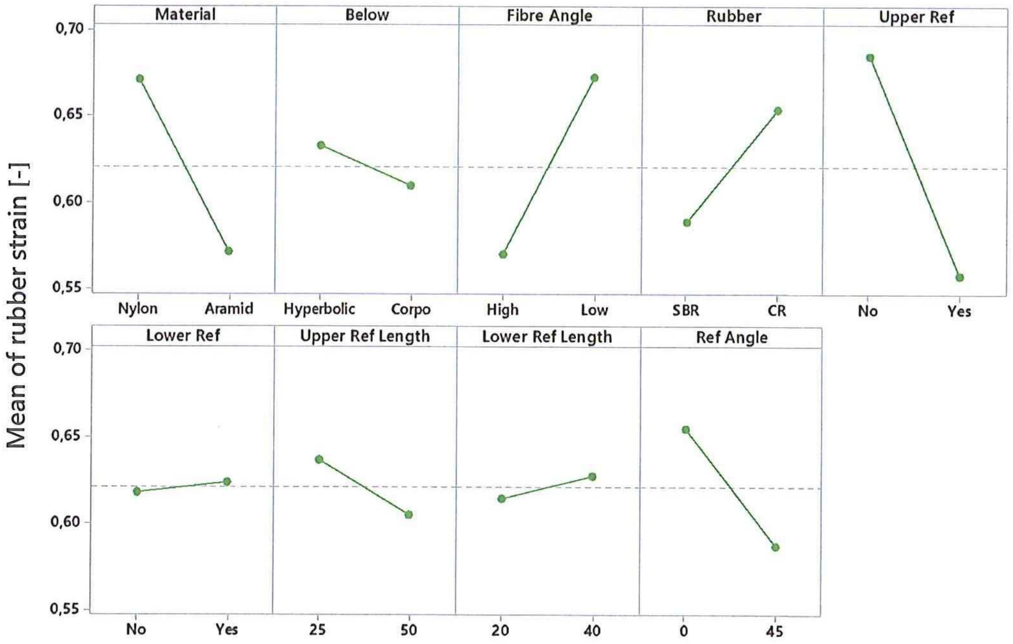

FIGURE C.1: MEAN EFFECTS OF MAIN PARAMETERS ON RUBBER STRAIN

The main effect on the maximum restricted fibre forces are shown in Figure C.2.

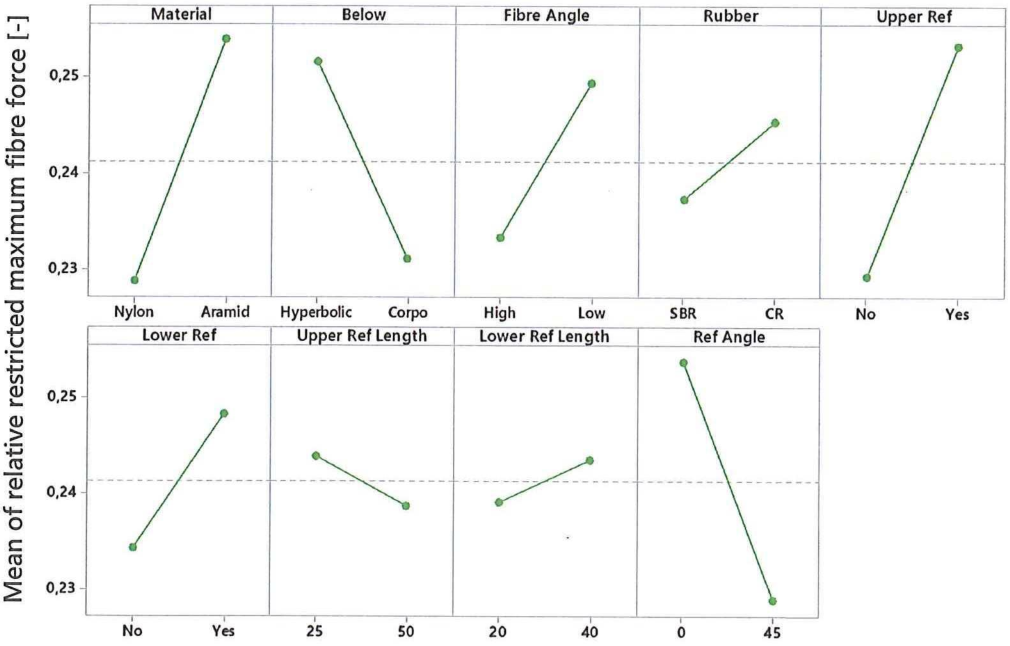

FIGURE C.2: MEAN EFFECTS OF MAIN PARAMETERS ON RESTRICTED MAXIMUM FIBRE FORCE

The main effects on the maximum fibre force during axial elongation are shown in Figure C.3.

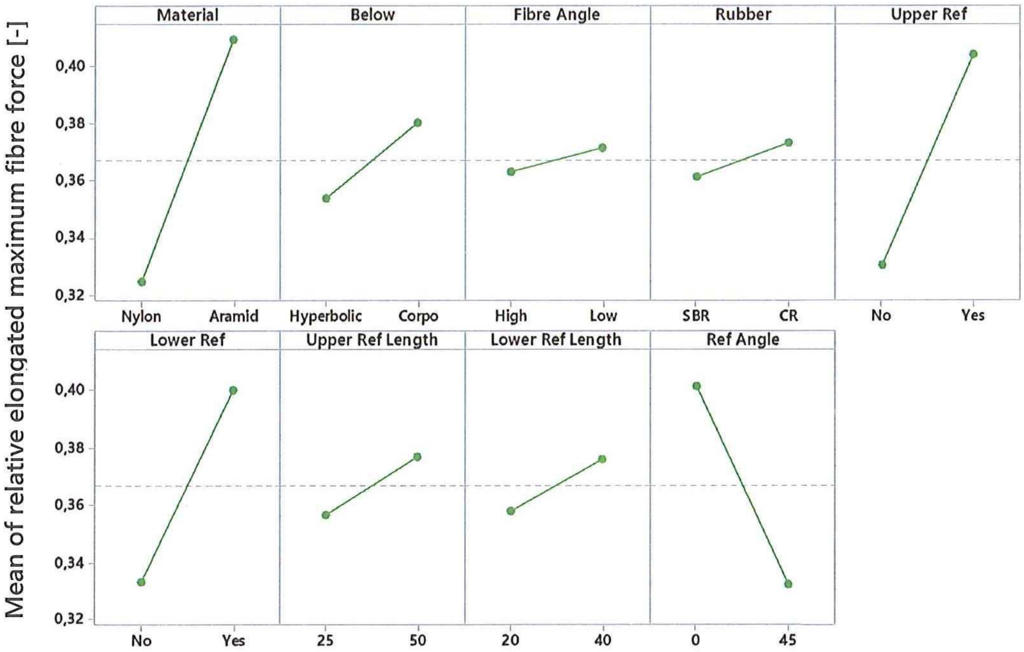

FIGURE C.3: MEAN EFFECTS OF MAIN PARAMETERS ON ELONGATED MAXIMUM FIBRE FORCE

The main effects on the maximum fibre force during lateral deformation are shown in Figure C.4.

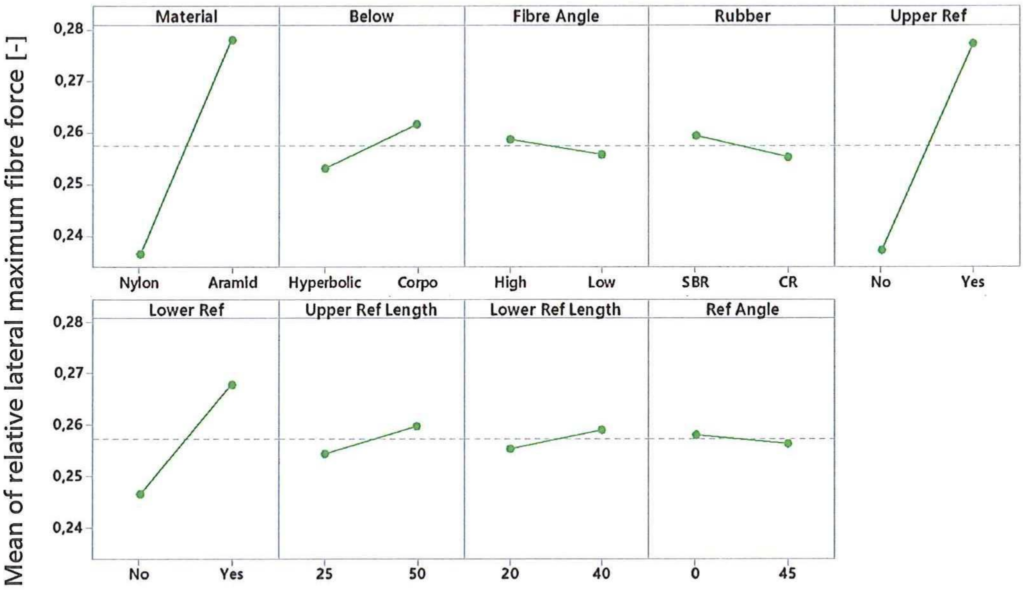

FIGURE C.4: MEAN EFFECTS OF MAIN PARAMETERS ON LATERAL MAXIMUM FIBRE FORCE

The main effects on the lateral deformation at which fibre compression occurs are shown in Figure C.5.

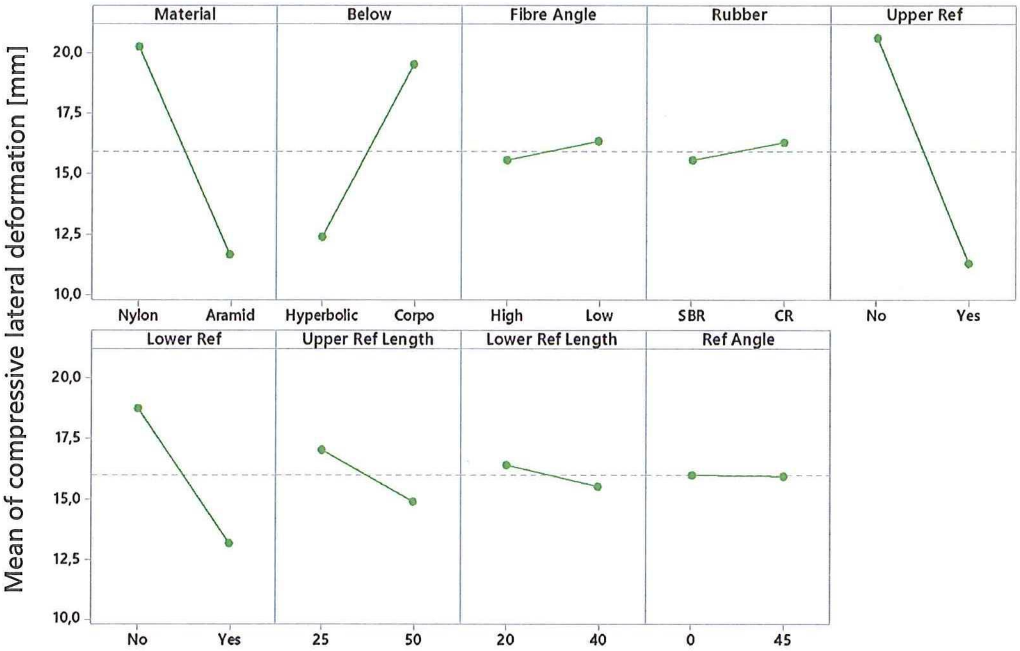

FIGURE C.5: MEAN EFFECTS OF MAIN PARAMETERS ON LATERAL DEFORMATION BEFORE COMPRESSIVE FIBRES

The main effects on the maximum fibre shear angle during axial elongation are shown in Figure C.6.

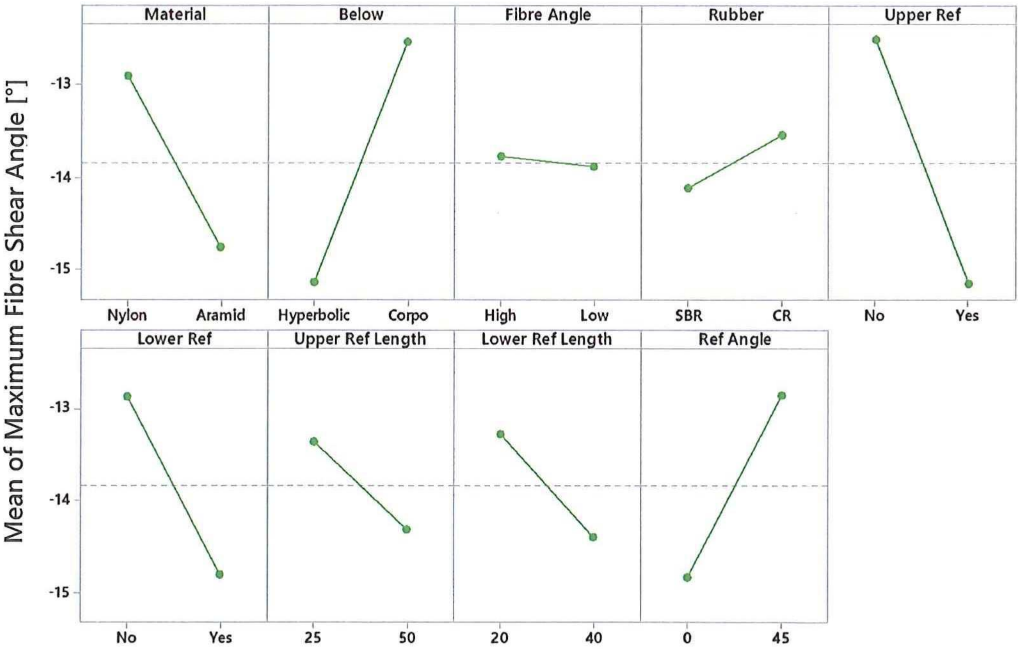

FIGURE C.6: MEAN EFFECTS OF MAIN PARAMETERS ON MAXIMUM FIBRE SHEAR ANGLE

C.3 OPTIMAL EXPANSION JOINT DESIGN GEOMETRY AND FIBRE ANGLES

The optimal expansion joint has Nylon Fibres and only an upper reinforcement layer. The inner and outer rubber thickness are 3,3 [mm]. The profiles of the fibre and rubber layers are shown in Figure C.7.

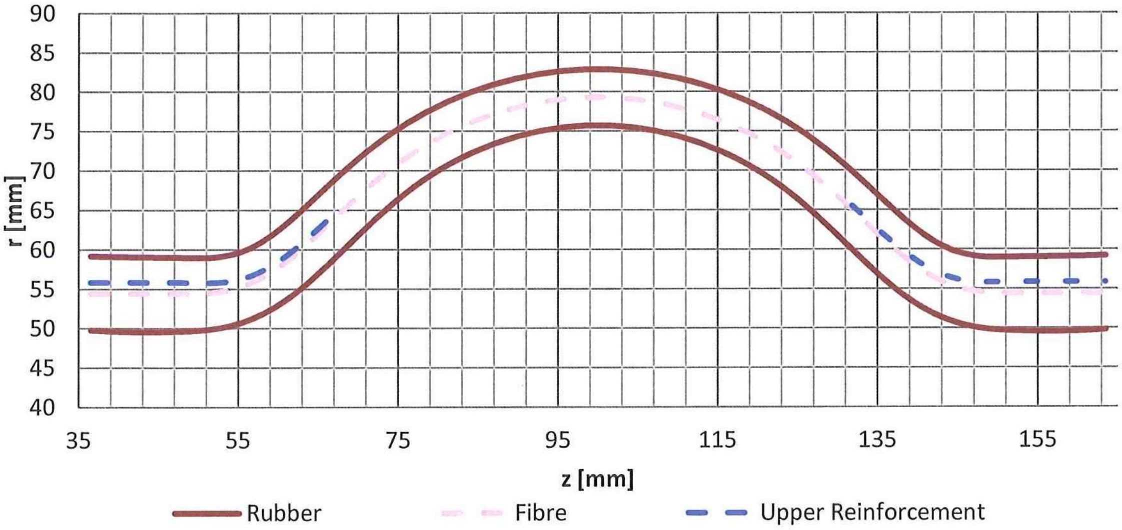

FIGURE C.7: OPTIMAL EXPANSION JOINT PROFILE

The fibre angle of the main fibre layer and the local reinforcements are given in Figure C.8. It should be noted that at the end of the local reinforcement the fibre angle is approximately the same as that of the main fibre layer, minimizing the stress concentrations.

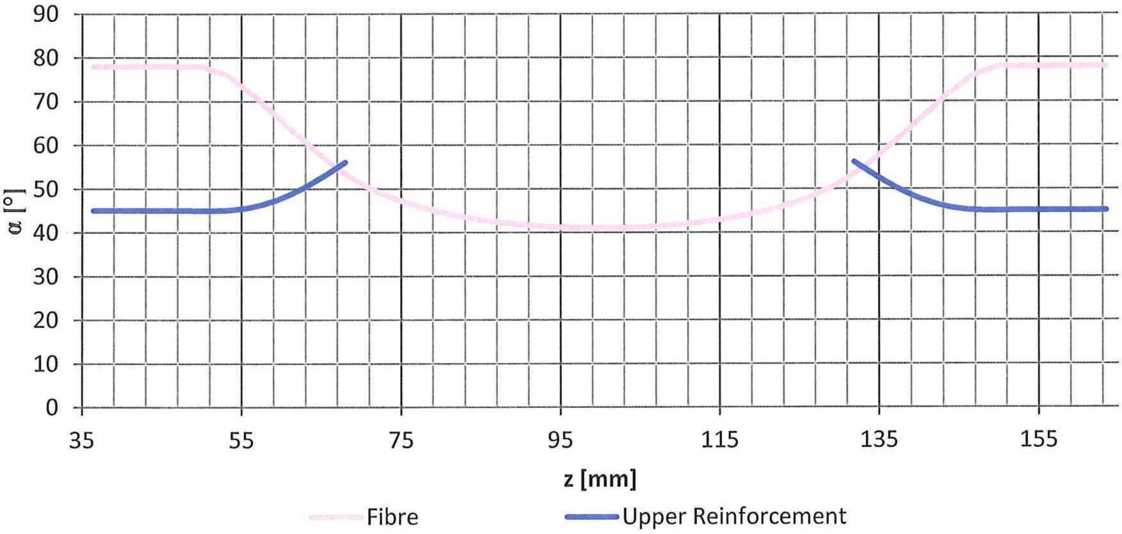

FIGURE C.8: OPTIMAL EXPANSION JOINT FIBRE ANGLES

C.4 REINFORCEMENT LENGTH EFFECTS FOR ARAMID EXPANSION JOINTS

The effect of the reinforcement length on the maximum rubber strain during all deformation modes for Aramid expansion joints are shown in Figure C.9.

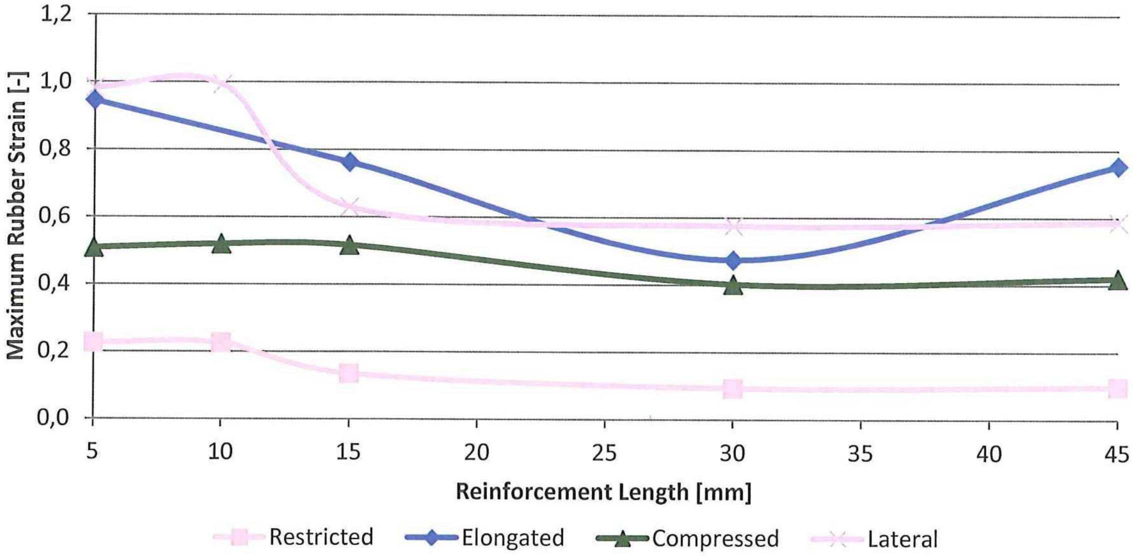

FIGURE C.9: RUBBER STRAIN VS. REINFORCEMENT LENGTH

The effect of the reinforcement length on the maximum fibre force during all axial deformation modes for Aramid expansion joints are shown in Figure C.10.

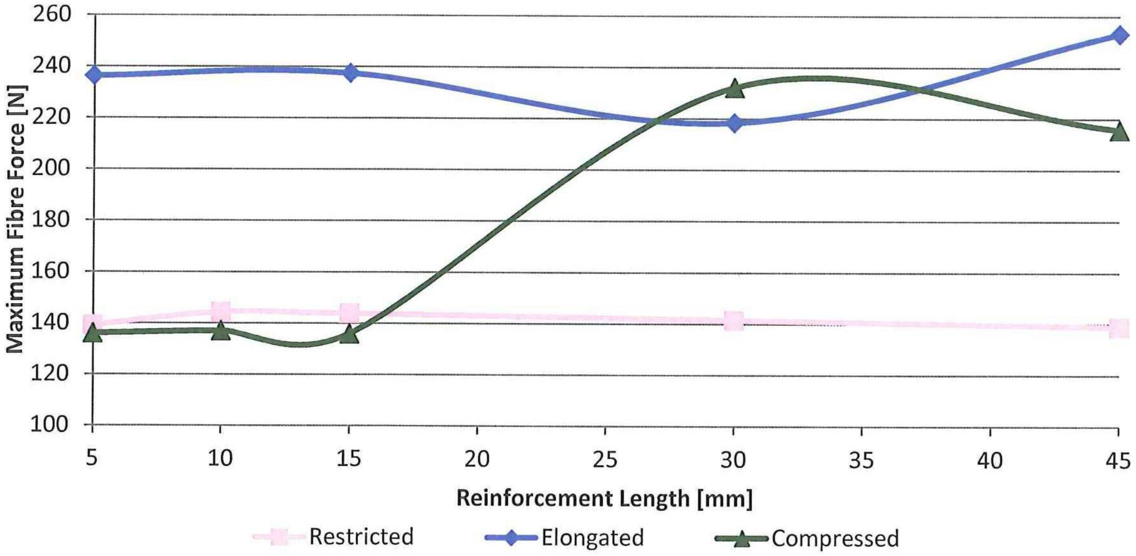

FIGURE C.10: FIBRE FORCE VS. REINFORCEMENT LENGTH

The effect of the reinforcement length on the predicted lateral deformation at which fibre compression occurs is shown in Figure C.11. It should be noted that the lateral deformation range is up to 20 [mm], and therefore even the design with the shortest reinforcement length will experience fibre compression.

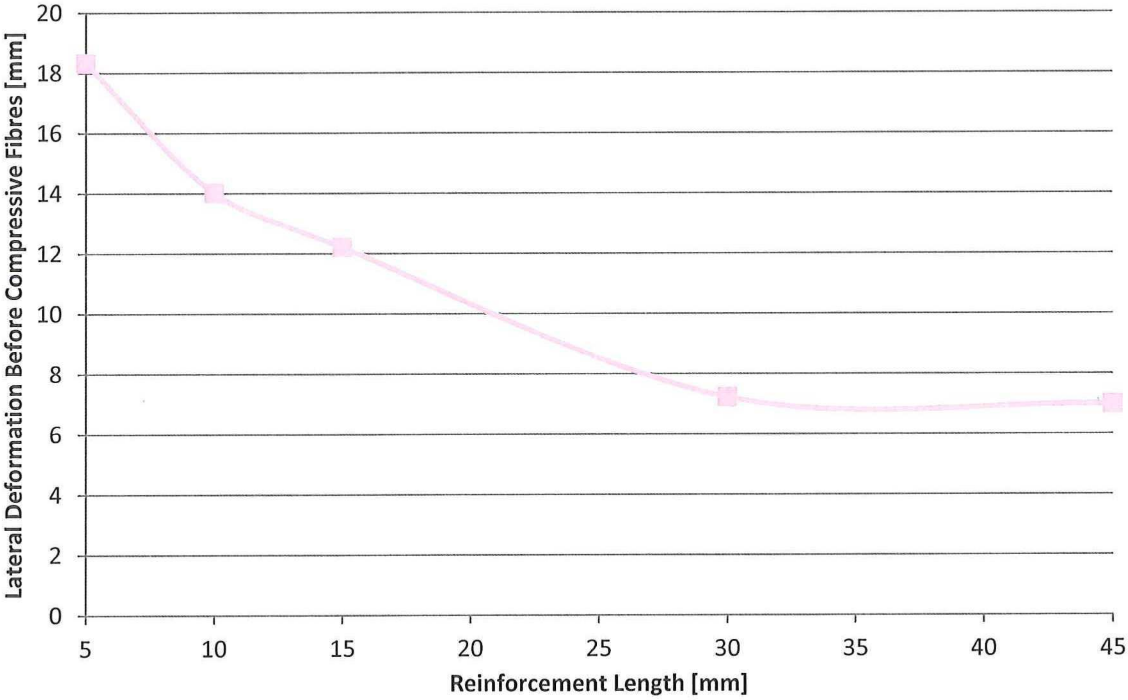

FIGURE C.11: LATERAL DEFORMATION BEFORE COMPRESSIVE FIBRES VS. REINFORCEMENT LENGTH

The effect of the reinforcement length on the maximum fibre shear angle during all deformation modes for Aramid expansion joints are shown in Figure C.12.

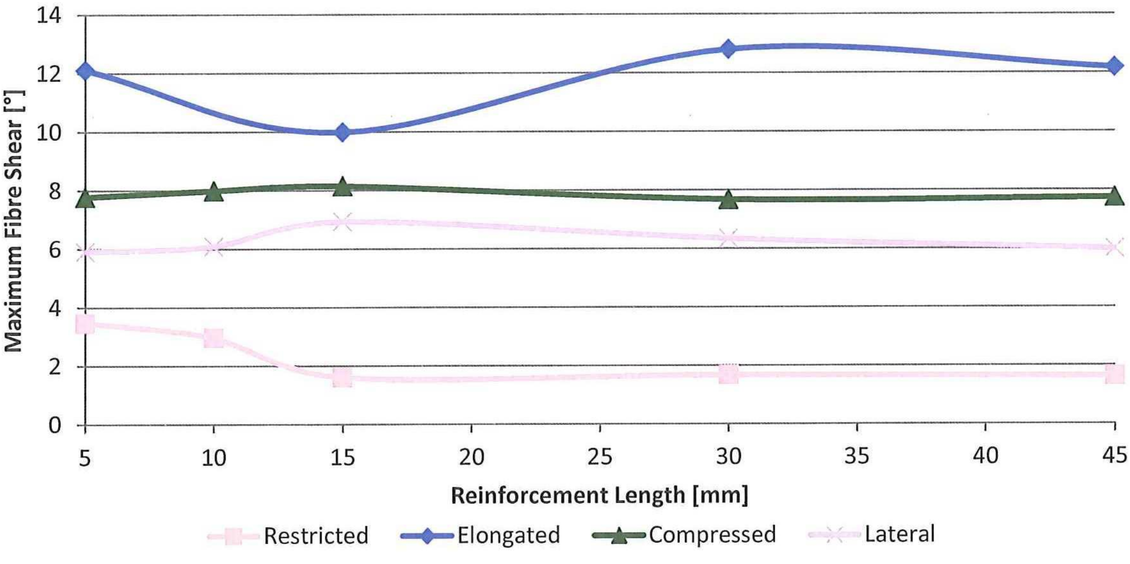

FIGURE C.12: FIBRE SHEAR VS. REINFORCEMENT LENGTH